

Integrated approach for auto-adaptive synchronous motor winding

THÈSE N° 8903 (2018)

PRÉSENTÉE LE 4 OCTOBRE 2018

À LA FACULTÉ DES SCIENCES ET TECHNIQUES DE L'INGÉNIEUR
LABORATOIRE D'ACTIONNEURS INTÉGRÉS
PROGRAMME DOCTORAL EN ROBOTIQUE, CONTRÔLE ET SYSTÈMES INTELLIGENTS

ÉCOLE POLYTECHNIQUE FÉDÉRALE DE LAUSANNE

POUR L'OBTENTION DU GRADE DE DOCTEUR ÈS SCIENCES

PAR

Florian Louis COPT

acceptée sur proposition du jury:

Dr R. Boulic, président du jury
Prof. Y. Perriard, Dr C. Köchli, directeurs de thèse
Prof. B. Dehez, rapporteur
Dr L. Burdet, rapporteur
Prof. P.-A. Farine, rapporteur



ÉCOLE POLYTECHNIQUE
FÉDÉRALE DE LAUSANNE

Suisse
2018

“Don’t ask what the world needs. Ask what makes you come alive, and go do it. Because what the world needs is people who have come alive.”

— **Howard Thurman**

Remerciements

L'accomplissement de ce travail de recherche n'aurait pas été possible sans l'aide et le soutien de diverses personnes que j'ai eu la chance de côtoyer. J'aimerais leur exprimer ma reconnaissance à travers ces quelques lignes.

Avant tout, je tiens à remercier le Professeur Yves Perriard de m'avoir offert l'opportunité d'effectuer cette thèse au sein de son laboratoire. Son soutien, ses encouragements et l'autonomie qu'il m'a accordée m'ont permis d'évoluer sur le plan professionnel. Un grand remerciement également au Dr. Christian Koechli tant pour son aide, sa disponibilité que les nombreux échanges enrichissants. Son expérience m'a été d'un grand secours pour affronter les différents défis qui ont traversés ma route. Je suis également très reconnaissant au Dr. Yoan Civet pour tout le temps qu'il m'a consacré et pour son encadrement sans faille des différentes étapes effectuées en salle blanche. J'aimerais également remercier le partenaire industriel Faulhaber minimotor sans qui cette thèse n'aurait pas été possible.

Ma reconnaissance va ensuite à tous ceux et celles qui de près ou de loin m'ont encouragé, conseillé, écouté et accompagné au cours de mes recherches. Ma gratitude va ainsi tout particulièrement à Mr. Paolo Germano pour le temps qu'il m'a consacré et ses explications, à Louis Masson pour le temps qu'il a investi à m'aider à améliorer l'écriture de mon manuscrit, à Jasha Poliakine pour nos bons moments en salle blanche ainsi qu'à François Baudart, Douglas Martins Araujo et Liu Xinchang, mes compagnons de travail nocturnes, dont les échanges m'ont beaucoup apporté. Je remercie également tous mes collègues présents et passés du laboratoire pour tous les bons moments partagés et les franches rigolades : Dan, Daniel, Romain, Chris, Tophe, Sean, Raphaël, Patricio, Guillaume, Cécile, Jonathan, Valentin, David, Alexis, Camilo et Magda.

Finalement, je tiens à remercier ma famille d'avoir toujours cru en moi quel que soit les défis que je rencontrais. C'est grâce à leurs encouragements et leur soutien que ce projet a pu être mené à bien.

Neuchâtel, August, 2018
Florian Copt

Abstract

The intrinsic characteristic of a permanent magnet synchronous motor is defined by its internal dimensions, its material properties, as well as the power supply used in conjunction with the motor. When an extended operating range is desired but the electronics are limited, motor manufacturers face a problem. Furthermore, when different operating points are needed –e.g. a low torque with a high speed as well as a large torque at a lower speed- the used drive system is oversized so that all operating points are included in the motor's characteristic. Therefore, this thesis aims to find a solution to obtain an extended operating range while considering the use of limited electronics. In addition, the proposed solution must be embeddable into the motor.

A survey of possible solutions allowing the increase of the motor's intrinsic characteristic is presented. Among them, the dynamic winding reconfiguration is chosen because it allows an increase in torque and in speed while having restrictions on the electronics. This reconfiguration is performed by using switches.

As the connections between the coils of the winding will be reshaped, coils can be placed in parallel. Depending on the geometrical distribution of these coils, circulating currents may appear, which in turn will be generating unwanted losses. Therefore, a study of the spatial distribution of the turns is undertaken demonstrating that these currents can be significantly reduced without adding complexity to the winding manufacturing.

Considering the integration of the switching system and the alternating current that will run through it, the MEMS (Micro Electro-Mechanical System) relays are favored because of their ease of use, their galvanic separation when they are open, but especially thanks to their separation between the control command and the signal, which removes all the floating voltage issues. In order to reduce the contact resistance, the design of the relay is based on an innovative system of double springs combined with variation of the flexural rigidity of the contact structure. In addition, the influence of microfabrications tolerances is considered in the design. A novel manufacturing process flow has been specifically developed to manufac-

ture the relay in a cleanroom environment. The prototypes obtained and the mechanical and electrical characterizations performed on them confirmed the feasibility of the design and the manufacturing methodology.

From then on, the control allowing the winding reconfiguration is studied. The latter focuses on slotless permanent magnet motors. Their low inductance implies rapid current variations and by extension rapid torque variations as well. The proposed methodology explores the transient regime from one configuration to another and is based on a fine control of current amplitude and the commutation angle. Numerical simulations and experimental results confirm the accuracy of the proposed approach.

Keywords: *Permanent magnet synchronous motor, Winding reconfiguration, Electromechanical modelling, MEMS relay, Circulating currents, Torque control*

Résumé

La caractéristique intrinsèque d'un moteur synchrone à aimants permanents est définie par ses dimensions internes, les propriétés des matériaux qui le constituent ainsi que de son alimentation. Lorsqu'une plage de fonctionnement étendue est désirée mais que l'électronique à disposition est limitée, les fabricants de moteurs sont confrontés à un problème. De plus, lorsque des points de fonctionnement très différents sont nécessaires - un faible couple avec une grande vitesse ou un grand couple à faible vitesse - l'électronique de commande utilisée doit être surdimensionnée de sorte que tous les points de fonctionnement soient compris dans la caractéristique du moteur. Sur la base de ce constat, cette thèse a pour vocation de trouver une solution intégrable dans le moteur qui permette d'obtenir une plage de fonctionnement étendue tout en considérant une électronique limitée.

La solution retenue est celle de la reconfiguration dynamique du bobinage. Cette reconfiguration est effectuée à l'aide de commutateurs qui modifient les connections entre les bobines et remodelent le bobinage. Selon l'organisation géométrique de ces bobines, des courants de circulations peuvent apparaître, engendrant des pertes non désirées. C'est pourquoi, la distribution spatiale des spires du bobinage a été analysée. Cette dernière démontre que ces courants peuvent être significativement réduits sans complexifier la fabrication des bobines.

En considérant l'intégration du système de commutation et le courant alternatif qui le traverse, une solution avec des relais MEMS (Micro Electro-Mechanical System) a été sélectionnée. Ces derniers offrent l'avantage de leur simplicité d'utilisation, leur séparation galvanique lorsqu'ils sont ouverts et surtout l'isolation entre la commande et le signal qui élimine tous les problèmes de tensions flottantes.

Afin de réduire la résistance de contact, le design du relais se base sur un système de doubles ressorts combinés avec une variation de la rigidité en flexion de la structure de contact. De plus, en vue d'une fabrication fiable, l'influence des tolérances de microfabrication a été prise en compte dans cette étude. Un nouveau procédé de fabrication a été spécifiquement développé afin de fabriquer le relais sur wafer silicium. Les prototypes obtenus ainsi que

les caractéristiques mécaniques et électriques effectuées sur ces derniers ont confirmé la faisabilité de la méthodologie de conception et de fabrication.

Dès lors, le contrôle permettant la reconfiguration a été étudié. Ce dernier se concentre sur les moteurs à aimants permanents sans encoches complétant ainsi la littérature dans ce domaine. Leur faible inductance implique des variations rapides de courant et par conséquent de couples. La méthodologie proposée explore le régime transitoire d'une configuration à une autre et se base sur un contrôle fin de l'amplitude du courant ainsi que de l'angle de commutation. Les simulations numériques et les résultats expérimentaux confirment l'exactitude de la démarche proposée.

Mots clefs : *Moteur synchrone à aimant permanent, Reconfiguration du bobinage, modélisation électromécanique, Relais MEMS, Courant de circulation, Control en couple*

Contents

| | |
|---|------------|
| Abstract (English/Français) | iii |
| List of figures | xi |
| List of tables | xv |
| 1 Introduction | 1 |
| 1.1 Background and motivation | 1 |
| 1.1.1 Permanent magnet synchronous motor structure | 2 |
| 1.1.2 Evolution and trends | 3 |
| 1.1.3 Motivation | 4 |
| 1.2 Outline of the thesis | 7 |
| 2 State of the art | 9 |
| 2.1 Modification of the motor's intrinsic characteristic | 10 |
| 2.1.1 Motor supply | 10 |
| 2.1.2 Motor command | 11 |
| 2.1.3 Variable magnetic flux | 12 |
| 2.1.4 Winding reconfiguration | 14 |
| 2.1.5 Choice of the method to change the motor intrinsic characteristic | 16 |
| 2.2 Possibilities to modify the winding configuration | 17 |
| 2.2.1 Commutators | 17 |
| 2.2.2 Mosfet | 18 |
| 2.2.3 Relay | 20 |
| 2.2.4 Implementation | 21 |
| 2.2.5 Choice of the solution | 21 |
| 2.3 Conclusion | 21 |
| 3 Circulating current | 23 |
| 3.1 Types of circulating currents | 24 |
| 3.2 The motor | 25 |
| 3.3 Modelling | 27 |
| 3.3.1 The back-emf | 27 |
| 3.4 Winding layouts | 30 |

Contents

| | | |
|----------|--|------------|
| 3.4.1 | Radially grouped | 30 |
| 3.4.2 | Tangentially grouped | 34 |
| 3.4.3 | Generalization | 35 |
| 3.5 | Conclusion | 36 |
| 4 | Design of the MEMS relay | 37 |
| 4.1 | Introduction | 38 |
| 4.1.1 | MEMs relays technologies | 38 |
| 4.1.2 | Existing geometry in electrostatic MEMs | 45 |
| 4.2 | Design | 47 |
| 4.2.1 | Resistance of the relay | 48 |
| 4.2.2 | Modelling using the Lagrange formulation | 55 |
| 4.2.3 | Breakdown voltage | 62 |
| 4.2.4 | Dynamic response analysis | 63 |
| 4.2.5 | Modal analysis | 66 |
| 4.3 | Design example | 66 |
| 4.3.1 | Influence of the microfabrication tolerances | 67 |
| 4.4 | Summary and conclusion | 69 |
| 5 | Microfabrication of the MEMS relay | 71 |
| 5.1 | Choice of the relay manufacturing method | 72 |
| 5.2 | Manufacturing | 75 |
| 5.2.1 | Introduction | 75 |
| 5.2.2 | The borofloat wafer process | 78 |
| 5.2.3 | The SOI wafer process | 82 |
| 5.2.4 | Bonding and release of the relays | 88 |
| 5.3 | Measurements and discussion | 94 |
| 5.3.1 | Distance between the electrodes | 94 |
| 5.3.2 | Stiffness of the structure | 95 |
| 5.3.3 | Switching measurements | 98 |
| 5.3.4 | Contact resistance | 99 |
| 5.4 | Summary and conclusion | 101 |
| 6 | Dynamic winding reconfiguration | 103 |
| 6.1 | Introduction | 104 |
| 6.2 | Reconfiguration criterion | 105 |
| 6.3 | Importance of the control strategy | 106 |
| 6.4 | Electrical setup | 107 |
| 6.5 | Series to parallel reconfiguration | 108 |
| 6.6 | Star to delta reconfiguration | 109 |
| 6.6.1 | State I & II | 109 |
| 6.6.2 | State III | 112 |
| 6.6.3 | State IV & V | 113 |

| | |
|---|------------|
| 6.6.4 State VI & VII | 113 |
| 6.6.5 State VIII | 115 |
| 6.6.6 Overview | 115 |
| 6.7 Experimental result | 116 |
| 6.7.1 Series to parallel reconfiguration | 117 |
| 6.7.2 Star to delta reconfiguration | 118 |
| 6.8 Modification of the motor dynamic | 120 |
| 6.9 Experimental verification of the motor characteristic extension | 121 |
| 6.10 Conclusion | 123 |
| 7 Conclusion and perspectives | 125 |
| 7.1 Original contributions | 126 |
| 7.2 Outlook and perspectives | 127 |
| A Vector potential | 129 |
| B Evaluation of the vector potential in the motor | 133 |
| C Process Flow | 135 |
| D Wafer carrier process flow | 145 |
| Bibliography | 158 |
| Curriculum Vitae | 159 |

List of Figures

| | | |
|------|--|----|
| 1.1 | Example of applications for permanent magnet synchronous motor | 1 |
| 1.2 | Comparison between the different types of permanent magnet synchronous motor | 2 |
| 1.3 | Built-in motion controller in a brushless servo motor from FAULHABER | 3 |
| 1.4 | Torque-speed limitation with no electronic limitation | 4 |
| 1.5 | Torque-speed limitation with a limited electronic | 5 |
| 1.6 | Operating range with an oversized drive system | 5 |
| 1.7 | Two motors to reach the separate operating points | 6 |
| | | |
| 2.1 | Possibilities to modify the motor intrinsic characteristic | 10 |
| 2.2 | The three diagrams of voltage and current for imposed speed - inspired from [44] | 12 |
| 2.3 | Variable magnetic flux | 14 |
| 2.4 | 5 phases reconfiguration possibilities [82] | 15 |
| 2.5 | Matrix motor [40] | 16 |
| 2.6 | Different types of four-quadrant circuits with transistor | 18 |
| 2.7 | Bootstrap circuit | 19 |
| 2.8 | Transformer | 20 |
| | | |
| 3.1 | Circulating currents | 24 |
| 3.2 | Flux density in the motor | 25 |
| 3.3 | Exploded view of the brushless DC motor | 26 |
| 3.4 | Representation of the motor's winding | 26 |
| 3.5 | Internal radius parametrization | 29 |
| 3.6 | Parametrization of the winding | 30 |
| 3.7 | Choice of spatial distribution of the winding - Cross section | 31 |
| 3.8 | Results for scenario <i>a</i> - radially grouped | 31 |
| 3.9 | Comparison of the back-emf between the model and the measurements | 31 |
| 3.10 | Back-emf for each conductor at 15'000 rpm | 32 |
| 3.11 | Results for scenario <i>a</i> - radially grouped | 32 |
| 3.12 | Circulating current at 15'000 rpm | 33 |
| 3.13 | Circulating current for scenario <i>b</i> , <i>c</i> and <i>d</i> - radially grouped | 34 |
| 3.14 | Results for scenario <i>a</i> - tangentially grouped | 34 |
| 3.15 | Circulating current for scenario <i>b</i> , <i>c</i> and <i>d</i> - radially grouped | 35 |

List of Figures

| | | |
|------|--|----|
| 4.1 | Bi-material thermal switch [77] | 39 |
| 4.2 | Thermal latch principle [6] | 39 |
| 4.3 | SPST MEMs [53] | 41 |
| 4.4 | SPDT MEMs [76] | 41 |
| 4.5 | MEMS reed switch (the external magnet or coil is not represented) [19] | 42 |
| 4.6 | Reed relay | 42 |
| 4.7 | Electrostatic MEMs | 44 |
| 4.8 | Measurement of the induction under the magnet using FEM | 45 |
| 4.9 | Two terminal relay | 46 |
| 4.10 | Three terminal relay | 46 |
| 4.11 | Four terminal relay | 46 |
| 4.12 | Design routine | 48 |
| 4.13 | Resistance of the relay in on state | 49 |
| 4.14 | Contact surface | 49 |
| 4.15 | Contact resistance for different material | 51 |
| 4.16 | Bending of the contact while the contacts are closing | 52 |
| 4.17 | Schematic of the contact part | 52 |
| 4.18 | Parametrization of the bending moment | 53 |
| 4.19 | Model of the relay | 56 |
| 4.20 | Rotational stiffness | 58 |
| 4.21 | Deflection calculated under 15 V actuation using FEM performed with ANSY | 59 |
| 4.22 | Pull-in simulation | 60 |
| 4.23 | Body diagram of a relay arm | 61 |
| 4.24 | Modified Paschen curve using [32] | 63 |
| 4.25 | Current peak when the relay is turned on | 64 |
| 4.26 | Current increase with the variation of the capacitance | 65 |
| 4.27 | Variation of the switching time depending on the voltage applied | 65 |
| 4.28 | Measures of the motor vibration (motor presented in section 3.2) in the XYZ directions | 66 |
| 4.29 | Dimension of the designed relay - dimension in μm | 67 |
| 4.30 | Round under cut | 68 |
| 4.31 | Influence of different parameters variations on the relay stiffness (Normalized value) | 69 |
| 5.1 | SEM view of the manufactured relay | 75 |
| 5.2 | Terminology used for the borofloat wafer | 76 |
| 5.3 | Terminology used for the SOI wafer | 76 |
| 5.4 | Emplacement of cross section used | 77 |
| 5.5 | Under etch between the photoresist and the seed layer | 80 |
| 5.6 | Example of the presence of fences - picture taken after the resist strip | 80 |
| 5.7 | Before and after the gold dry etch of the borofloat | 81 |

| | | |
|------|--|-----|
| 5.8 | SEM images at the end of the borofloat wafer process flow. The deformation at the extremities of the structure of the left picture is due to the limit of the optics | 82 |
| 5.9 | The borofloat after all the steps have been performed | 82 |
| 5.10 | SEM images after <i>KOH</i> etching and oxide etching with a <i>HF</i> solution | 84 |
| 5.11 | Excrescence during a bad electroplating | 85 |
| 5.12 | Bad electroplating | 86 |
| 5.13 | Good electroplating | 86 |
| 5.14 | SEM images after the gold etching | 87 |
| 5.15 | Dry etch of the top silicon to manufacture the relay structure | 88 |
| 5.16 | Silicon oxide residue inside cavities | 88 |
| 5.17 | Test of tungsten deposition to alleviate the stress of the stack wafer | 91 |
| 5.18 | Evaluation of the required tungsten thickness deposition | 91 |
| 5.19 | Process flow of the wafer bond | 92 |
| 5.20 | Carrier wafer used for the wafer bond | 93 |
| 5.21 | SEM and microscope view of the manufactured relay after the release | 93 |
| 5.22 | Schematic representation of two parallel plates with a dielectric | 94 |
| 5.23 | Capacitance measured on the MEMs relays | 95 |
| 5.24 | Variation of the capacitance with 220 nm SiO ₂ thickness measured according to the analytical model | 95 |
| 5.25 | Schematic view of the force sensor system | 96 |
| 5.26 | Force-displacement measurement setup | 97 |
| 5.27 | Force-displacement measurements | 97 |
| 5.28 | Stiffness dispersion | 97 |
| 5.29 | Deflection of the relay due to an externally applied voltage | 99 |
| 5.30 | Contact resistance measurement | 99 |
| 5.31 | Electroplating result | 100 |
| 5.32 | Contact electroplating | 100 |
| 5.33 | Zoom on the targeted force | 101 |
| 6.1 | Reconfiguration criterion | 106 |
| 6.2 | Torque simulation when all the phase are interrupt at the same time | 106 |
| 6.3 | Torque simulation with a phase per phase reconfiguration but without any strategy | 107 |
| 6.4 | Electric circuit for the winding reconfiguration - inspired from [66] | 107 |
| 6.5 | Reconfiguration criterion for series to parallel | 108 |
| 6.6 | Simulated winding reconfiguration using current control strategy | 109 |
| 6.7 | Simulated current while reconfiguring the winding | 110 |
| 6.8 | Star to delta reconfiguration steps - the current flow is represented in red | 111 |
| 6.9 | Control signal for each phase | 113 |
| 6.10 | Current control loop | 114 |
| 6.11 | Simulated current signal during winding reconfiguration from star to delta | 115 |
| 6.12 | Evolution of the simulated torque while accelerating | 116 |
| 6.13 | Setup for the control command | 116 |

List of Figures

| | |
|--|-----|
| 6.14 Relay prototype board | 117 |
| 6.15 Evolution of the measured current during the winding reconfiguration | 118 |
| 6.16 Evolution of the measured phase 2 current during the winding reconfiguration | 118 |
| 6.17 Evolution of the measured phase 2 current during the winding reconfiguration | 119 |
| 6.18 Measured currents of phase 2 and 3 during the winding reconfiguration | 119 |
| 6.19 Speed comparison with or without reconfiguration | 121 |
| 6.20 Speed comparison with or without reconfiguration | 121 |
| 6.21 Torque-speed characteristics with and without winding reconfiguration | 122 |
| 6.22 Torque-speed characteristic with winding reconfiguration | 123 |
| | |
| B.1 Internal radius parametrization | 133 |

List of Tables

| | | |
|-----|---|-----|
| 2.1 | Comparison of the different methods to increase the motor intrinsic characteristic | 17 |
| 2.2 | Comparison between commutators | 18 |
| 2.3 | Number of available configurations and number of switches needed [66] | 21 |
| 3.1 | Joule losses at 3000 rpm | 32 |
| 4.1 | Summary of the MEMs real values found in the literature | 44 |
| 4.2 | Values used for the comparison between the two models | 55 |
| 4.3 | Contact deformation | 55 |
| 4.4 | Value used for the dynamic response analysis | 64 |
| 4.5 | Design relay properties | 67 |
| 5.1 | Wafer bonding | 74 |
| 5.2 | Process flow for the borofloat wafer | 78 |
| 5.3 | Process flow for the SOI wafer | 83 |
| 5.4 | Process flow for the bonding of the two wafers and the release of the structure | 89 |
| 6.1 | Resistance, speed and torque constant for different winding configurations | 105 |
| 6.2 | Commutation table during the winding reconfiguration | 115 |

1 Introduction

1.1 Background and motivation

Nowadays, electrical motors have become essential in the electronic appliances and transportation in the day to day life of society. A multitude of categories of electrical motors are used across these domains, such as synchronous, asynchronous, brushless DC, or DC motors. Among these, the permanent magnet synchronous motor shall be the focus of the present thesis. It can be found in different applications such as in domestic or commercial, which include computer peripherals, multimedia, ventilation or aero-modelling; in transportation for electrical vehicles; in industrial application when precise motion control is necessary; in aerospace, medical or research field applications when the reliability, wear, environment and the operating time are crucial. A non-exhaustive list of applications where this motor can be found is shown in fig. 1.1.

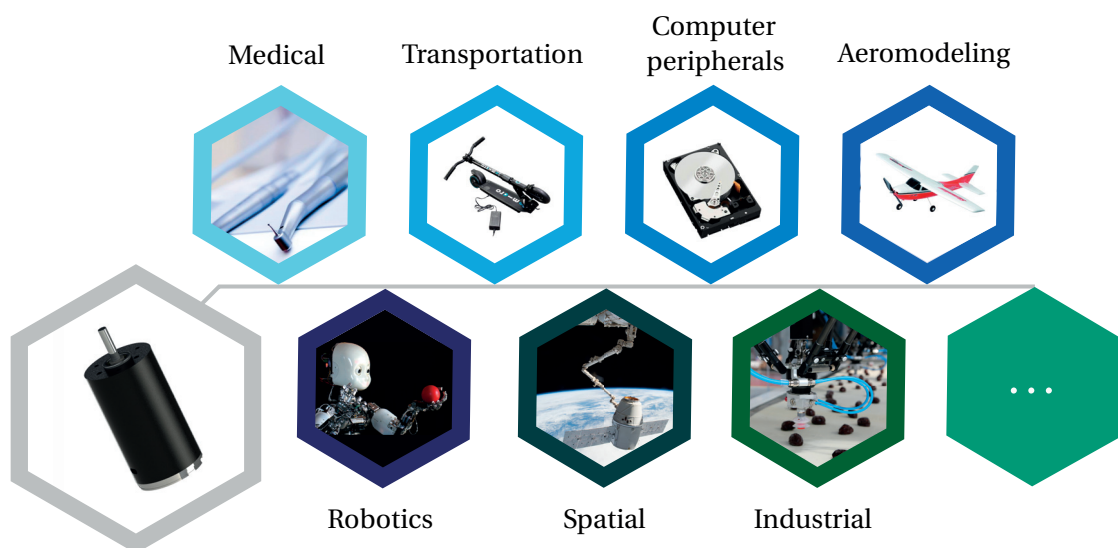


Figure 1.1 – Example of applications for permanent magnet synchronous motor

1.1.1 Permanent magnet synchronous motor structure

Permanent magnet synchronous motor or brushless motors can be separated into two types depending on their stator geometry: slotted and slotless motors, as illustrated in fig. 1.2

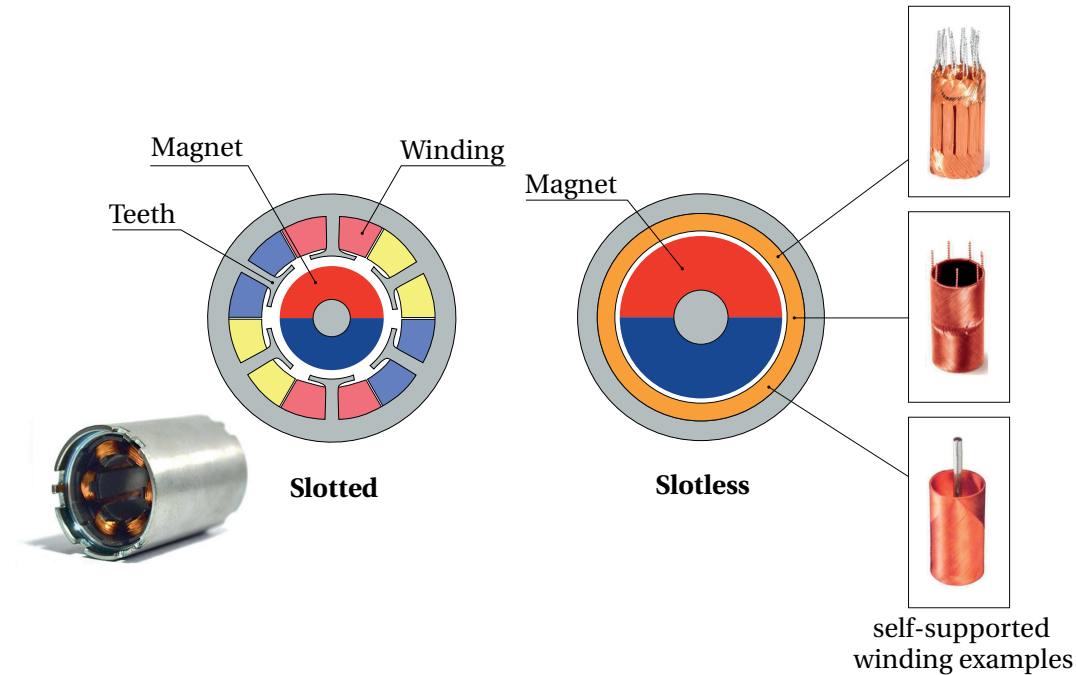


Figure 1.2 – Comparison between the different types of permanent magnet synchronous motor

Slotted motors have a preferred equilibrium position when the motor is not supplied because the air gap is increased at the tooth extremities. The interaction of the rotor magnet with the stator teeth generates a cogging torque. Furthermore the heat dissipation is improved as the stator yoke is bigger. Consequently, a higher power density is possible.

For slotless motors, the winding is self-supported and is placed in the air gap. They do not have a preferential equilibrium position due to the absence of teeth. Consequently, there is no cogging torque, which reduces the vibration and noises. However, as the air gap is bigger compared to the slotted configuration, the inductance is smaller resulting in higher current variations.

Different images of fig. 1.1 and fig. 1.2 have been taken from different websites accessed on July 9, 2018:

- Fig. 1.1 Medical: <https://ch.mathworks.com/> ; Robotic: <https://frontiersinblog.files.wordpress.com/2016/08/icub-robotics-robot-1024x684.png?w=940>; TransportationSpatial: <https://www.universetoday.com/>; Computer peripherals: <https://pisces.bbystatic.com/> ; Industrial: <http://www.camagroup.com/>; Aeromodeling: <https://www.dcm-modelisme.com/>;
- Fig. 1.2 The slotted motor: <https://www.hsdcmotor.com/>; The self-supported windings: <https://encrypted-tbn0.gstatic.com/>

1.1.2 Evolution and trends

Since the 1980s, when permanent magnets became more available and sufficiently strong [93], this type of motor has continued to see improvements in its design, allowing permanent magnet synchronous motor to reach their current performances. These enhancements can be separated into three categories: the hardware, the control and the motor itself.

Due to advancements in microcomputer and inverter capabilities, a finer control of the motor position, dynamic and speed range has become possible with the introduction of vector control strategies. This control has also provided sensorless vector control techniques introduced in 1989 that could be used as a replacement to the required Hall sensor for the phase commutations. However, this control was imprecise at low speeds. Solutions based on test signals have been proposed since 1999 [64]. In terms of the motor structure itself, researchers have recently been investigating the possibility of exchanging the wire winding for a flexPCB, providing new possible winding shape optimizations and a higher filling factor [21].

Nowadays, there is a miniaturization trend that pushes the motor manufacturers to propose compact motor solutions with a built-in electronics to save space or simplify the user experience. For example, the integration of the electronic drive simplifies the use and the control of the motor. Consequently, its installation and startup time is reduced, which lowers the user cost. Furthermore, the motor system can be preconfigured according to the manufacturer specifications, which limits misuse and protects the electronics. Other integrated systems found on the market are encoders or motion controllers as shown in fig. 1.3. The main limitation of a motor is its thermal operating range. Usually, a safety margin is used to protect the motor from overheating. However, build-in thermal sensor can be added as well in order to reduce this margin.

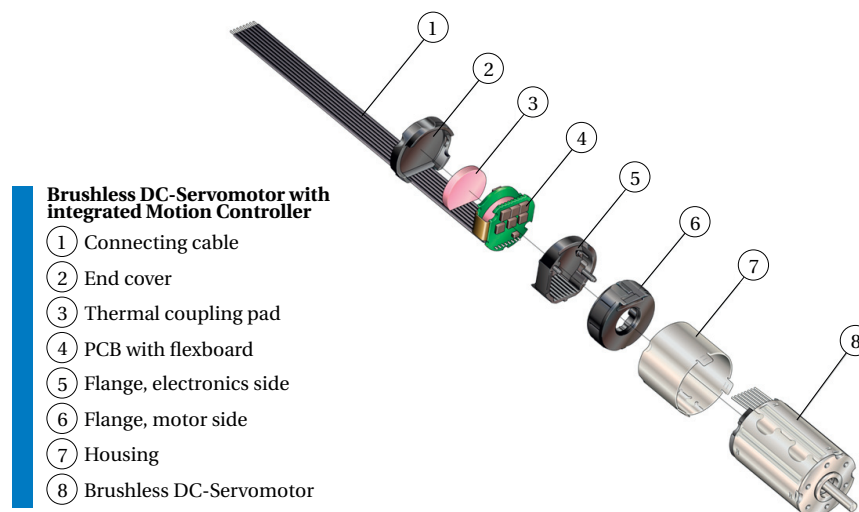


Figure 1.3 – Built-in motion controller in a brushless servo motor from FAULHABER

1.1.3 Motivation

The performance of permanent magnet synchronous motors is defined by their operating range, which is represented by a torque-speed curves. This intrinsic characteristic is defined and fixed by the motor’s internal and geometrical characteristics and by the power supply. For this reason, the same intrinsic characteristic can be obtained for different sources by changing the motor design.

However, motor manufacturers are challenged by clients who require motors with extensive operating ranges. Indeed, it can occur that reshaping the motor internal design is not sufficient in order to reach the desired working points.

Consequently two issues can be identified:

- How to achieve extensive operating range when the electronics are limited?
- How to reduce the winding cost for the motor manufacturer?

Consequence of limited electronics

One of the most suitable solutions to increase the operating range of a motor is by reconfiguring the winding. If there were no restriction on the electronics, the main motor limitation would have been the Joule losses produced by the winding. When the winding is rearranged, the phase-phase resistance is modified as well. Consequently, for equivalent Joule losses, the maximum currents are different. Fig. 1.4 shows an example of different operating ranges obtained for multiple winding combinations at equivalent Joule losses. The horizontal line represents the Joule losses safety margin limitation chosen by manufacturers to avoid the winding to overheat.

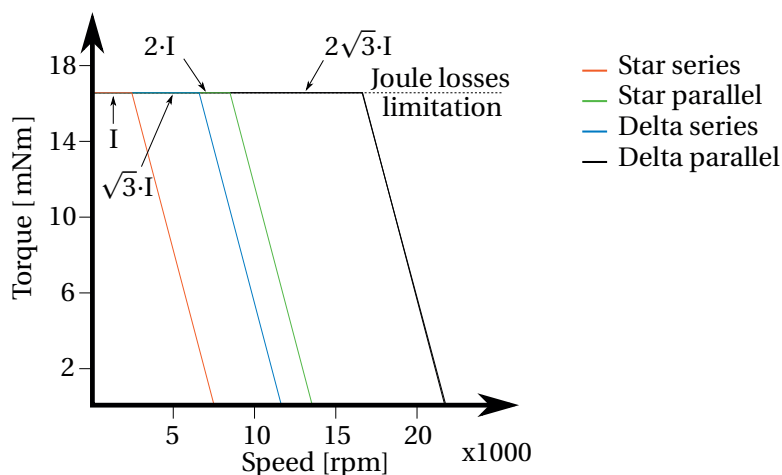


Figure 1.4 – Torque-speed limitation with no electronic limitation

As evidenced by this figure, all the operating ranges can be included in one range if only Joule

1.1. Background and motivation

losses are considered. However, if the electronics are limited, the torque-speed operating ranges are reduced because the current and the voltage are limited, narrowing down the maximum torque of each of the winding configurations as indicated in fig. 1.5. The maximum torque of each configuration is referenced to the star-series configuration maximum torque -i.e. M - if the motor was designed for this configuration.

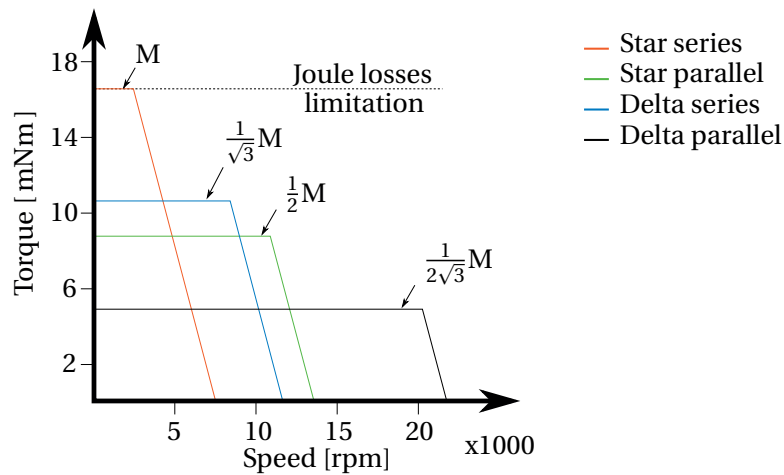


Figure 1.5 – Torque-speed limitation with a limited electronic

Different working points

Permanent magnet synchronous motors can be used at different operating points. If a high torque is required at low speed, and another working point is at a higher speed but with a lower torque, the operating range of the latter shall include both. Consequently, the drive system is oversized.

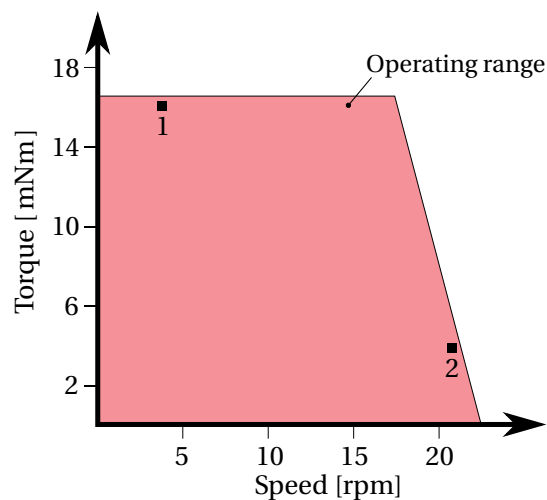


Figure 1.6 – Operating range with an oversized drive system

Chapter 1. Introduction

Fig. 1.6 shows an example of two different working points that need an oversized drive system. If two motors were to be used, they would have been specified for the targeted application and they would require a lower power input as shown in fig. 1.7

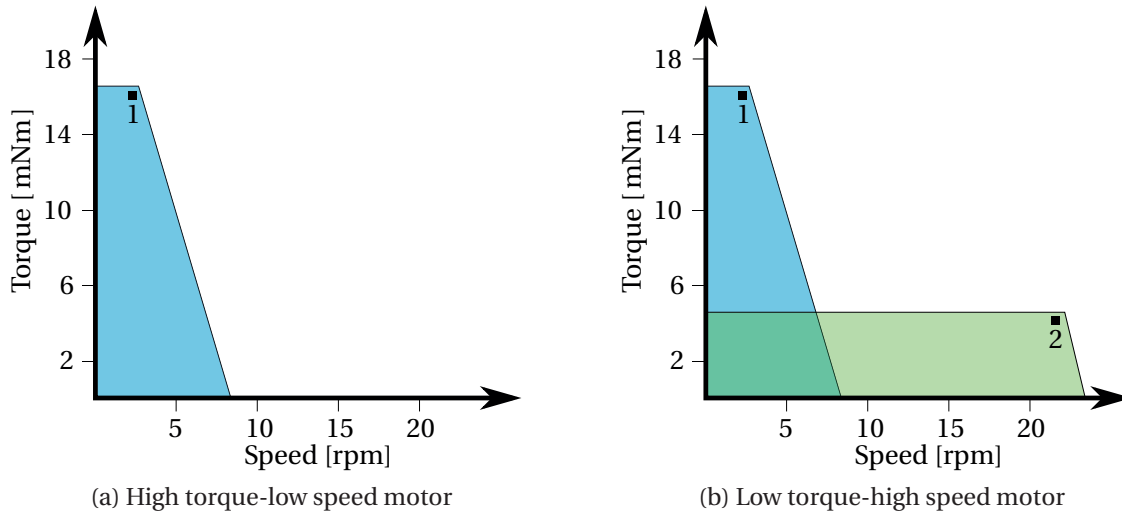


Figure 1.7 – Two motors to reach the separate operating points

If a motor could have a specific operating range for a given operating point, a smaller power supply would be required and the dynamic of the motor would be improved. These two operating ranges can be obtained within a single motor by adapting the winding configuration. For example, by reconfiguring the winding, the motor intrinsic characteristic is modified, which results in a different torque-speed limitation that can be driven with the same limited electronics.

Same motor's intrinsic characteristic with different supplies

The commercial permanent magnet synchronous motor performance is described by its operating range, which is represented by a torque-speed curve. This intrinsic characteristic is defined and fixed by the motor internal and geometrical characteristics. For this reason, motor manufacturers offer motors that have only one intrinsic characteristic, which is not interchangeable. The same characteristic can be achieved by modifying the motor internal design and by changing its supply as well. However, this results in an increased motor production cost as different motors (windings) are manufactured.

Research context

This thesis aims to achieve different aspects. Firstly, the main goal is to extend the motor intrinsic characteristic when the electronics are limited. Then, in order to follow the current trend which consists in having a built-in solution that simplifies the user experience, the developed system should be embedded in the motor and should be able to adapt to the

working situations. For this reason, miniaturization is a key factor in this research, more specifically in the design of the embedded system as well as in its realization.

1.2 Outline of the thesis

As previously explained, the idea is to extend a motor's intrinsic characteristic. For this reason, chapter 2 is dedicated to the summarization of existing research in the field and a comparison between the different instigated venue to find the best fit solution. From this solution, further investigations on the integration of such a system will be performed while considering the electrical and the mechanical aspects.

When it comes to winding reconfigurations, the winding distribution defines the intrinsic motor characteristic. Between the numerous possibilities, winding turns can be connected either in series or in parallel. Depending on the winding organization, circulating currents may appear. Therefore, chapter 3 will focus on the consequences of the winding distribution on circulating currents in order to provide an understanding of how to minimize this effect. This study will be supported by an analytical model which will be confronted to measurements performed on a prototype.

In order to reconfigure the winding, small switches are needed. As no solution was found on the market to satisfy the requirements of this research, dedicated switches needed to be manufactured. Consequently, chapter 4 will present their design, which will consider different aspects. As the final aim is to integrate them with the winding, their influence on the overall electrical circuit shall be minimal. The influence of the manufacturing steps will be considered together with their influence on the properties of the switches.

Chapter 5 will be devoted to the fabrication of the switches. A cleanroom process flow will be designed by considering the manufacturing challenges. Finally, in order to study the obtained switches, a measurement setup will be presented.

Chapter 6 will deal with the reconfiguration process using switches. Permanent magnet motors with small inductances suffer from fast current variations while switching, causing torque jerks. In this context, a control methodology to reduce them will be proposed in chapter 6.

Finally, chapter 7 will conclude this thesis by summarizing the main conclusions and contributions achieved. Some outlooks for future researches will be given as well.

2 State of the art

Contents

| | |
|---|-----------|
| 2.1 Modification of the motor's intrinsic characteristic | 10 |
| 2.1.1 Motor supply | 10 |
| 2.1.2 Motor command | 11 |
| 2.1.3 Variable magnetic flux | 12 |
| 2.1.4 Winding reconfiguration | 14 |
| 2.1.5 Choice of the method to change the motor intrinsic characteristic . . . | 16 |
| 2.2 Possibilities to modify the winding configuration | 17 |
| 2.2.1 Commutators | 17 |
| 2.2.2 Mosfet | 18 |
| 2.2.3 Relay | 20 |
| 2.2.4 Implementation | 21 |
| 2.2.5 Choice of the solution | 21 |
| 2.3 Conclusion | 21 |

Motor performances are defined by their operating range, which are represented by a torque-speed curve. This intrinsic characteristic is defined by the electronics, the physical dimension of the motor and the properties of the material used. Generally, motors have only one characteristic. When a large range of speed and torque is required, usually the drive system is oversized so that all the working points are included in the motor characteristic. However, the source used to supply the motor can be limited, which will refrain the motor to reach the required performances. Different methods thus provide a temporary or permanent increase of the motor operating range. In order to choose the most suitable solution, the methods will be presented, discussed and compared.

Once the method is chosen, toward having an integrated solution, a focus on the implementation is necessary. Different solutions can be considered. However, they can quickly become voluminous. As a consequence, they will be reviewed and confronted.

2.1 Modification of the motor's intrinsic characteristic

The motor's intrinsic characteristic is defined by three main parameters : the supply, the control of the inverters and the motor itself as shown in figure 2.1. Firstly, depending on the supply, the speed or the torque can respectively be increased by having a higher voltage or more current. Secondly, by adapting the command on the inverters, the magnetic flux perceived by the phases can be reduced. As a result, the motor's speed limitation is increased. Finally, the motor internal dimensions (iron , air gap or the rotor shaft), the physical properties of the material used (permeability of the iron or the type of magnet) or the winding composition or configuration play a major role. The back-electromotive force (back-emf) resulting in the variation of the magnetic flux in the air gap determines the limitation of the torque and the speed.

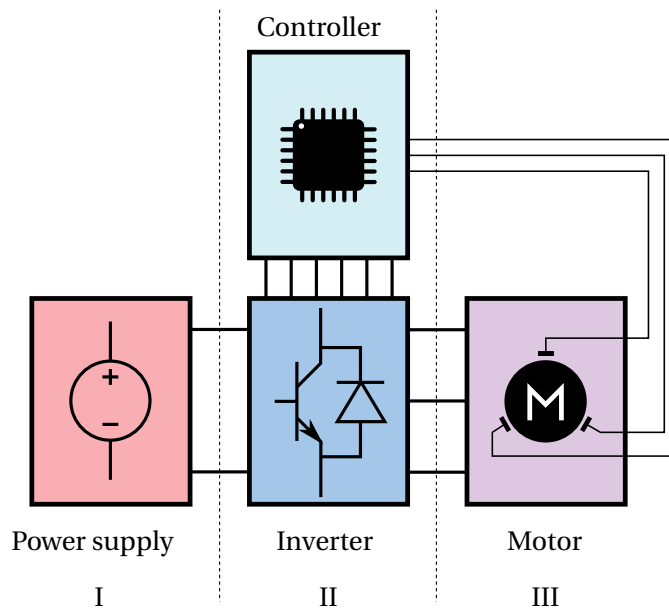


Figure 2.1 – Possibilities to modify the motor intrinsic characteristic

2.1.1 Motor supply

In order to operate, the motor needs to be supplied. The power source gives the necessary energy to set the motor in motion. According to the voltage or the current supplied, the motor can reach a given speed and a given torque. An increase of the voltage allows the motor to reach a higher speed. Conversely, an increase of the current allows the motor to reach a higher torque. Nevertheless, when the electronic are limited, the supply can be insufficient to attain a desire working point. As a consequence, the input voltage or current need to be increased. Two solutions exist in order to boost or buck-boost the input voltage or current. It is possible to use a step-up DC/DC power converter to boost the input voltage while buck-boosting the current (reciprocally) or to use the Z-source inverter [74].

2.1. Modification of the motor's intrinsic characteristic

There are two main circuits that can be used as step-up DC/DC converter: isolated converter and non-isolated converter. Isolated converters such as flyback and fullbridge offer a stepping up or down due to the ratio of the turn across a transformer. However, core losses, winding losses, transition losses and external losses reduce the efficiency of these converters [14, 45]. Furthermore, due to the presence of bulky components, the overall size is substantial compared to non-isolated converter. Therefore, non-isolated converters are favoured. Theoretically, they can attain an infinite gain. However, in practice, the gain is limited to Joule losses of the boost coil caused by its intrinsic resistance [12].

The Z-source converter offers a higher voltage gain than conventional boost converters without increasing the turn ratio for the same duty cycle [25]. As a consequence, this converter is more adapted for high boost applications. Furthermore, this converter can be used for current boost as well. As this added electric circuit can only boost the voltage for a voltage source or boost the current if the source is a current source, the modification of the intrinsic characteristic can only be on the torque or on the speed limit.

2.1.2 Motor command

In order to control the rotation of the motor, the timing during which a phase is supplied as a function of rotor position angle is crucial. This commutation angle is the difference angle between the back-emf and the source voltage. Depending on the advance angle on the command it is possible to obtain a higher speed or a higher torque as shown with eq. (2.1).

$$M = \frac{m \cdot p \cdot U}{\omega \cdot Z_s^2} [\hat{U} \cos(\delta - \epsilon) - R_s I] \quad (2.1)$$

where M is the torque, ϵ is the argument of the impedance, δ is the angle between the back-emf and the source voltage, I is the current, m is the number of phases, p is the number of pole pairs, ω is the angular speed, R_s is the stator resistance, Z_s is the stator impedance and U is the supply voltage.

In order to control this commutation angle, for three phase motors, each phase is represented by a vector placed in an abc frame (a stands for the first phase, b stands for the second one and c stands for the third phase). Each phase is spaced by 120° . It is possible to simplify this representation by transforming the three phase frame (abc) into a bi phase frame ($\alpha\beta$) followed by a rotational transformation (dq). The advantage of using the dq frame to represent the overall vector system is that the control is simplified (2 vectors instead of 3).

Fig. 2.2a shows a representation of the vectors in the dq when the torque is not maximum and fig. 2.2b shows the result for the command when the torque is maximized.

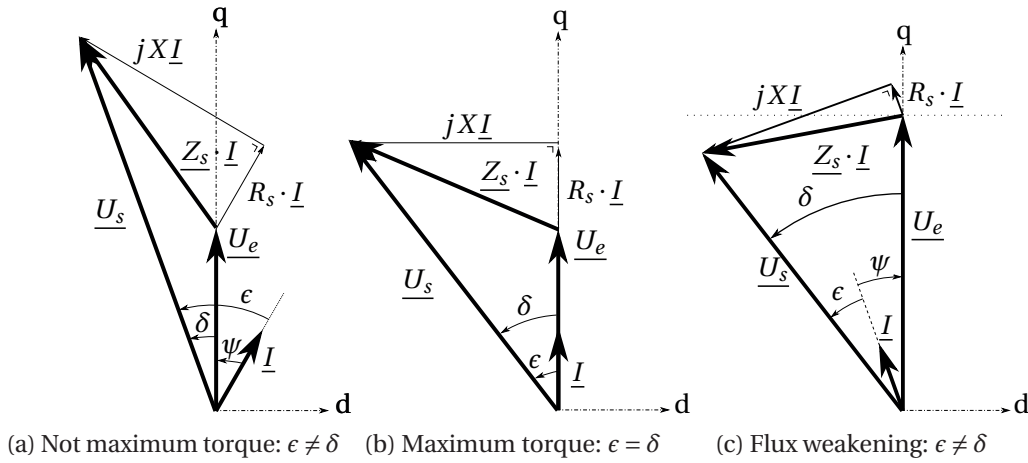


Figure 2.2 – The three diagrams of voltage and current for imposed speed - inspired from [44]

In these figures : ϵ is the argument of the impedance, δ is the angle between the back-emf and the source voltage, ψ is the angle between the back-emf and the current, \underline{I} is the current, \underline{U}_e is the back-emf and \underline{U}_s is the source voltage.

While the rotor is in motion, Lenz's law reveals that a back-emf is generated in the coil due to the variation of magnetic flux. As the back-emf is function of the speed, the speed is limited when the back-emf reaches the amplitude of the source voltage

$$\underline{U}_s = R_s \underline{I} + jX \underline{I} + \underline{U}_e \quad (2.2)$$

If the amplitude of the back-emf exceeds this limit, the current will reverse and the free-wheel diodes will start to conduct. In order to increase the speed limitation and bear the increase of the back-emf, the commutation angle is advanced. It can be done by setting $i_{d,ref}$ to a negative value. As a result, the maximum torque is reduced but the speed range is extended. The vectorial result is shown in figure 2.2c. The purpose of this technique is to reduce the magnetic flux of the magnet seen by the phase by creating a magnetic flux that is opposed to this flux. This technique is named flux-weakening [57].

By setting a negative reference on the d axis, a flux that is opposed to the natural magnetic flux is created. As a consequence, this solution is not very efficient because it burns up energy into the winding. Moreover, during the flux weakening, the current increases which leads to an increase of Joules losses in the coil.

2.1.3 Variable magnetic flux

The motor torque results from the magnetic force between the magnet and the rotating magnetic field. For instance, for constant dimensions and for the same power supply, if the air gap flux density produced by the rotor magnets decreases, the torque will decrease as well. Furthermore, as the flux density in the air gap decreases, the back-emf will decrease as well.

2.1. Modification of the motor's intrinsic characteristic

As a consequence, for the same voltage supply, the motor can reach higher speeds.

Electrical method

By using the principle of magnetization and demagnetization of a magnet by applying a current pulse, the flux density in the airgap can be modulated. This has been explored in [68, 69] where the rotor was composed of soft iron and AlNiCo magnets. This type of magnet has a high remanence and a low coercivity which means that they can easily be magnetized or demagnetized by applying a current pulse. However, as the remanence of AlNiCo is lower than NdFeB the flux density in the air gap is lower as well. As a consequence, the torque of the motors using only AlNiCo is lower as well.

As a workaround to increase the air gap flux density, a hybridization between AlNiCo magnet and NdFeB can be used. [110, 111, 15, 85, 5, 43]. Once again, by applying a current pulse, AlNiCo can be magnetized or demagnetized without influencing the magnetization of the NdFeB magnet by following the fact that NdFeB magnets have a higher coercivity. As a consequence, NdFeB magnets ensure a constant high flux density in the air gap and AlNiCo varies the flux density. Two types of magnetization/demagnetization are possible: AC-demagnetization [110, 111, 15, 85, 5, 43, 59, 46, 60] or DC-demagnetization [112, 56, 113]. The basic difference between these two is that in AC-demagnetization, the magnets are demagnetized by using the d-axis current pulse to magnetize or demagnetize and for DC-demagnetized motor, an extra coil may be needed in most cases to magnetize or demagnetize the magnet. Note that performances can vary according to the arrangement of the magnets in the rotor [5] and that due to re-magnetization, fatigue of the magnet has been observed [95].

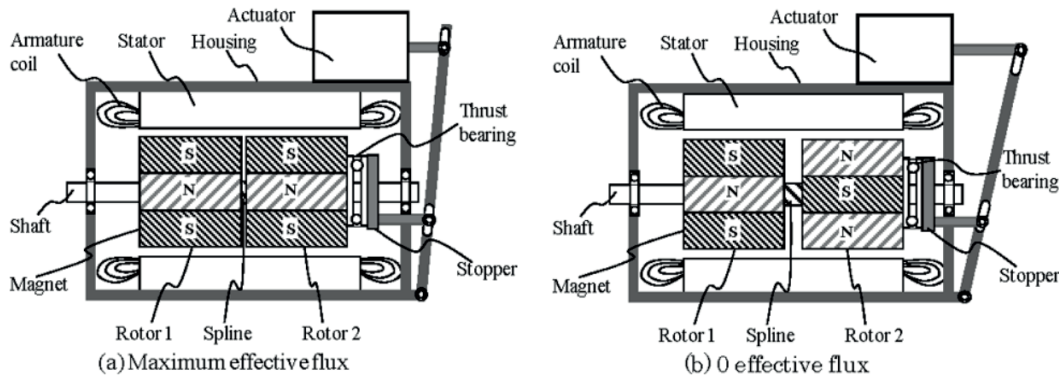
Another possibility to reduce the air gap flux density is the use of a combination of permanent magnets and an excitation magnetic circuit (coils). The excitation can either be in series or in parallel. In series excitation, the coils can either be placed in the rotor [61, 26] which is an added excitation that allow field regulation or the stator [7, 97]. For parallel excitation, a winding is added, which has a different flux. In this case, by injecting a current in the coil, magnetic iron poles are created and the flux flows from one pole to another. Nevertheless, such motors are complicated to manufacture and the added winding increases the stator volume and reduces the power density in the airgap [97]. Finally, the magnets can also be an hybrid combination of AlNiCo and NdFeB combined with an armature winding which improves the motor power density [58].

Mechanical method

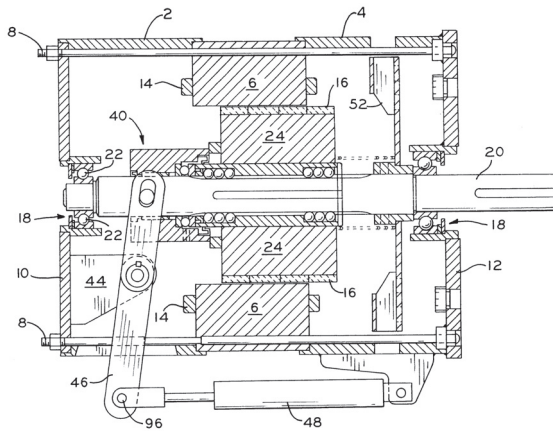
The magnetic flux can also be modified by mechanical actuation. Indeed, the mechanical methods can be focused on the magnet [114, 115, 108] or on the iron [62, 70]. A mechanical approach is to axially displace the rotor. The magnet thus becomes misaligned (figure 2.3b), and the flux seen by each phase can be controlled as a consequence. Another possibility is

Chapter 2. State of the art

to separate the rotor in two parts composed of magnets as shown in fig. 2.3a. By misaligning the magnet on the second part, the flux can also be modified. Another option is to modify the volume of the iron by inserting or removing iron parts as shown in figure 2.3c. As a result, the permeance of the magnetic circuit increases or decreases, which leads to a modification of the flux. Note that mechanical modification of the flux requires an external actuator. Therefore, the motor as a whole becomes sizeable and will consume more power which decreases its efficiency. Moreover, by adding a new degree of complexity, the reliability of the overall system decreases.



(a) Variable magnetic flux motor [115]



(b) Variable axial rotor/stator alignment [114]



(c) Mechanically adjusted variable-flux [70]

Figure 2.3 – Variable magnetic flux

2.1.4 Winding reconfiguration

The variation of the magnetic flux seen by the winding induces an electromotive force in the winding according to Faraday's law of induction. Depending on the winding configuration, the amplitude and the phase of the back-emf changes. As a consequence, by changing it, the motor's intrinsic characteristic is modified.

Star-Delta-Series-Parallel

Changing the winding connection from star to delta decreases the torque constant of the motor. This implies that, at constant voltage, the motor will be able to increase its speed by a factor of $\sqrt{3}$. As the torque is directly proportional to the torque constant of the motor, its value will also decrease by the same factor. The same reasoning applies in the opposite case.

Another option is to change the winding configuration by splitting the winding in two and placing each group of turns in series to parallel. Subsequently, the torque constant of the motor will decrease by a factor of two [13] and will increase the speed by the same factor. Reciprocally, the same development can be carried out for the opposite change. Mixing series-parallel and star-delta reconfiguration has already been presented in [13, 65, 66].

These changes may suggest that putting all the turns in parallel will allow a drastic increase of the speed and setting all the turns in series will give a significant gain to the speed. The main issue processing that way is that the number of switches will drastically increase [65] along with losses.

When it comes to mutliphase permanent magnet motors, changing the winding connection can also be considered. For five-phases electric machines [83, 82], for instance, it is possible to place the winding in : star, pentagon or pentacle configuration as shown in figure fig. 2.4. Each of them have different torque-speed characteristic and by changing from one to the other one, it is also feasible to obtain a motor with different intrinsic characteristics.

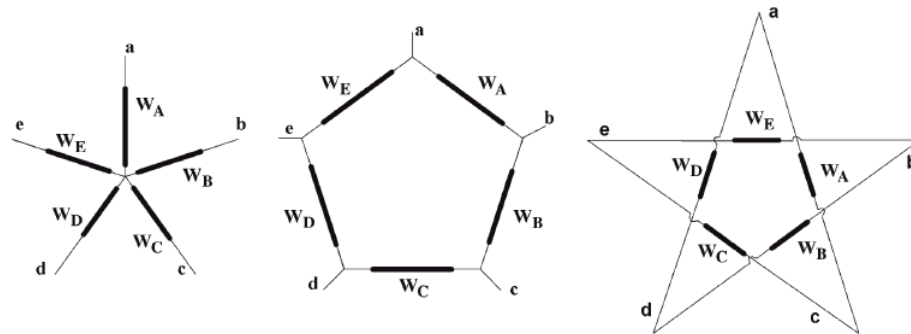


Figure 2.4 – 5 phases reconfiguration possibilities [82]

Modifying the number of turns

When it comes to increasing angular velocity, an easy solution is to reduce the back-emf. By bypassing a portion of the winding whereas the coils are in series, the total back-emf of the winding is reduced, which allows the motor to increase the limit speed regardless of the losses in the winding [51, 9]. The opposite is also conceivable. By adding turns, the available torque is greater but the maximum speed is smaller [51].

Some research has further investigated this possibility and have developed a matrix motor

where each winding is connected to solid-state switches as shown in fig. 2.5 [38, 40, 39]. This allows the user to switch between series or parallel concentrated winding. Online winding reconfiguration methods have also been carried out. Nevertheless, the integration of the switching circuits has not been considered.

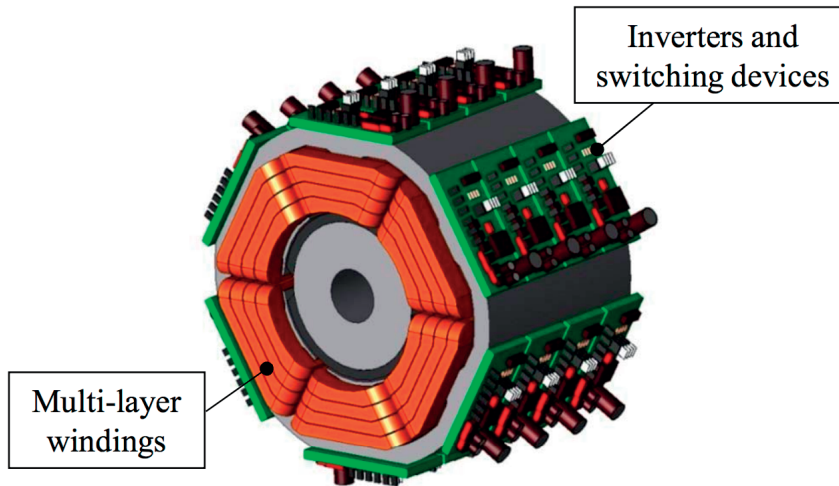


Figure 2.5 – Matrix motor [40]

2.1.5 Choice of the method to change the motor intrinsic characteristic

In order to increase the motor intrinsic characteristic when the source power is limited three methods are possible. It is possible to add a circuit in order to boost the input voltage or current, to adapt the motor control or to modify the internal structure of the motor.

- By adding a boost to the motor source, the limitation of the voltage or the current can be overcome. However, the power of the source stays constant. This excess is made at the expense of the other named parameter. As a result the maximum torque or maximum speed will be increased while the other one will be more limited.
- Flux weakening is an interesting solution due to the fact that by adapting the commutation angle, the overtake of the back-emf and the voltage on the resistance over the source voltage can be overcome. Nevertheless, such technique includes drawbacks. For brushless DC motor, it is impossible to do flux weakening without an external inductance as the inductance for such motor is small. Furthermore, the efficiency is reduced because more energy is burned up into the winding. Furthermore, flux weakening can induce Eddy currents in the rotor permanent magnet and generate unwanted radial forces.
- The motor structure and its material properties define the intrinsic characteristic. In order to increase the latter, the variable magnetic flux method let the motor operate in a wide range of power. However, the control is complicated because of the magnetization

2.2. Possibilities to modify the winding configuration

or demagnetization process of the targeted magnets. Furthermore such structures are complex and are hard to manufacture. Contrary to the latter solution, the winding reconfiguration method is not complicated to implement and offers multiple intrinsic characteristics for the same power supply.

Table 2.1 shows the comparison between the different methods presented. Red marks are used to indicate unfit solutions for our study. In this study, no drive modification is wanted and no current boost is accepted. As a result, the winding reconfiguration method comes out. Nevertheless, further investigation has to be undertaken in order to have an integrated solution .

Table 2.1 – Comparison of the different methods to increase the motor intrinsic characteristic

| | Motor Supply | Control | Motor | | Winding Reconfiguration |
|---|--------------|----------|------------------------|----------|-------------------------|
| | | | Variable magnetic flux | | |
| | | | Electric | Mechanic | |
| Flux density | Normal | Normal | Smaller | Normal | Normal |
| Risks of demagnetization | No | Possible | Yes | No | No |
| Current/voltage available modified¹ | Yes | No | No | No | No |
| Manufacture | Normal | Normal | Complex | Complex | Medium |
| Efficiency | Unchanged | Reduced | Reduced | Reduced | Unchanged |

¹ at the expense of the other one

2.2 Possibilities to modify the winding configuration

The reconfiguration of the winding resides in a change of the electric connections between the coils. Therefore, commutators are needed. The most critical point lies in the choice of the switching mode because each switch faces a major challenge: the commutator must bear the maximum current and the maximum voltage. Adding components increases the phase resistance. Finally, as the applied voltage and current will be positive and negative, a four-quadrant switch is needed. In order to answer this problematic, a state of the art for the switches is made before discussing their implementation.

2.2.1 Commutators

The commutators can be divided into two parts: solid state switches and mechanical switches. Because it is requested that the commutations should be performed online, purely mechanical solutions are rejected. Efforts are focused on solid state switches and on current or voltage controlled mechanical switches.

Depending on the application, there exists different types of switches that have different properties. The switch can be unidirectional in voltage and current (single quadrant), current bidirectional (two quadrants switch), voltage bidirectional (two quadrants switch) and finally

Chapter 2. State of the art

bidirectional in voltage and in current (four quadrants switch). Table 2.2 compares the different types of switches. Red marks are used to indicate unfit solutions and orange marks are used when the solution is taken up by the intrinsic diode.

Table 2.2 – Comparison between commutators

| | | Controllable | | Bidirectional | | Size | Turn on/off speed |
|-------------|----------|--------------|---------|---------------|---------|--------------|-----------------------|
| | | Closing | Opening | Voltage | Current | | |
| Diode | Bipolar | No | No | No | No | Small | VeryFast (ns) |
| | Schottky | No | No | No | No | Small | VeryFast (ns) |
| Solid State | Bipolar | Yes | Yes | Yes | No | Small | VeryFast (ns) |
| | Mosfet | Yes | Yes | Yes | Yes | Small | Very Fast (ns) |
| | IGBT | Yes | Yes | Yes | No | Small | VeryFast (ns) |
| | SCR | No | Yes | No | No | Medium | Fast (μ s) |
| Thyristor | ASCR | No | Yes | No | No | Medium | Fast (μ s) |
| | RCT | No | Yes | Yes | Yes | Medium | Fast (μ s) |
| | GTO | Yes | Yes | No | No | Medium | Fast (μ s) |
| | Triac | No | Yes | Yes | Yes | Medium | Fast (μ s) |
| Relay | | Yes | Yes | Yes | Yes | Medium-large | Medium-Fast(μ s) |

From table 2.2, the transistor mosfet and the relay come out.

2.2.2 Mosfet

Mosfet transistors are not really four-quadrant controllable circuits. However, there exists multiple setups combining these transistors with diodes that exhibit four-quadrant properties as shown in fig. 2.6.

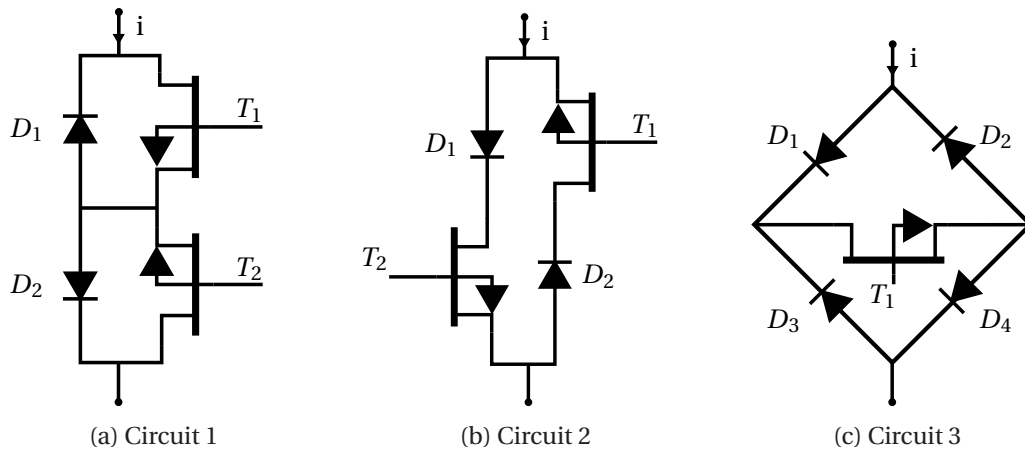


Figure 2.6 – Different types of four-quadrant circuits with transistor

The circuit presented in fig. 2.6a and the one presented in fig. 2.6b are working quite similarly. Indeed, by turning the transistor T_1 on the current flows through the latter and diode D_2 . When the current needs to flow in the opposite direction, transistor T_2 is this time turned on and diode D_1 is conducting. In the case presented in fig. 2.6c, the transistor T_1 is turned on and the current flows through it. Thus, when the current flows in one direction, it can flow through the diode D_1 and D_4 and in the other direction the current flows through D_2 and D_3 .

2.2. Possibilities to modify the winding configuration

In order to turn the transistor on, a positive voltage across the gate terminals and the emitter is required. By having multiple coil placed in series, a floating voltage will appear. As a consequence, this positive voltage can not be insured. Several circuit exist in order to counteract this problem. A non exhaustive list is presented below.

Bootstrapping

The idea beneath this circuit is to load a capacitor which will act as a floating supply, referenced at the upper switch emitter terminal. The capacitor is reloaded at the control supply through the bootstrap diode as show in fig. 2.7. The advantage of this circuit is that it is a cheap solution. Note that if the floating voltage does not go below bootstrap supply, the capacitor can not reload.

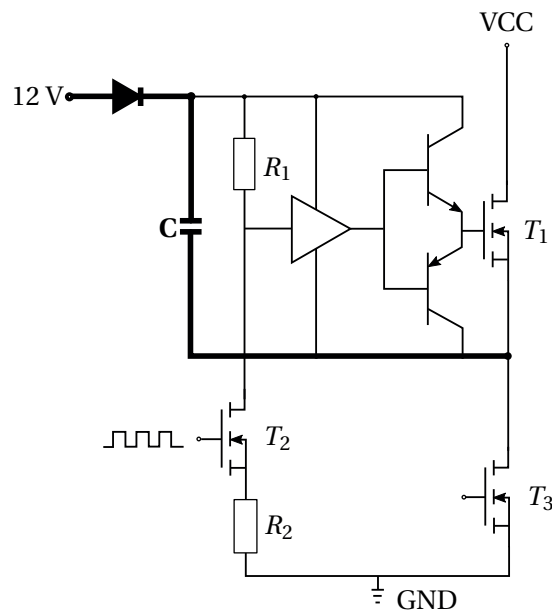


Figure 2.7 – Bootstrap circuit

Recently, a novel type of mosfet - i.e. called photomosfet - has become available on the market that removes the floating voltage problem infrared emitting diode actuation method. However, in order to drive sufficient current, the conducting resistance of such mosfet is currently too high.

DC-DC converter

The DC-DC converter is the easiest method to be implemented but the most expensive one. It consists in a device that converts a DC supply to another floating one. Nevertheless DC-DC converter are quite voluminous solutions.

DC-DC transformer

It is also possible to imagine a transformer with a single primary circuit and multiple secondary circuits. Fig. 2.8 show a non exhaustive list of possible circuits for the primary circuit (fig. 2.8a) and the secondary circuit (fig. 2.8b,2.8c,2.8d).

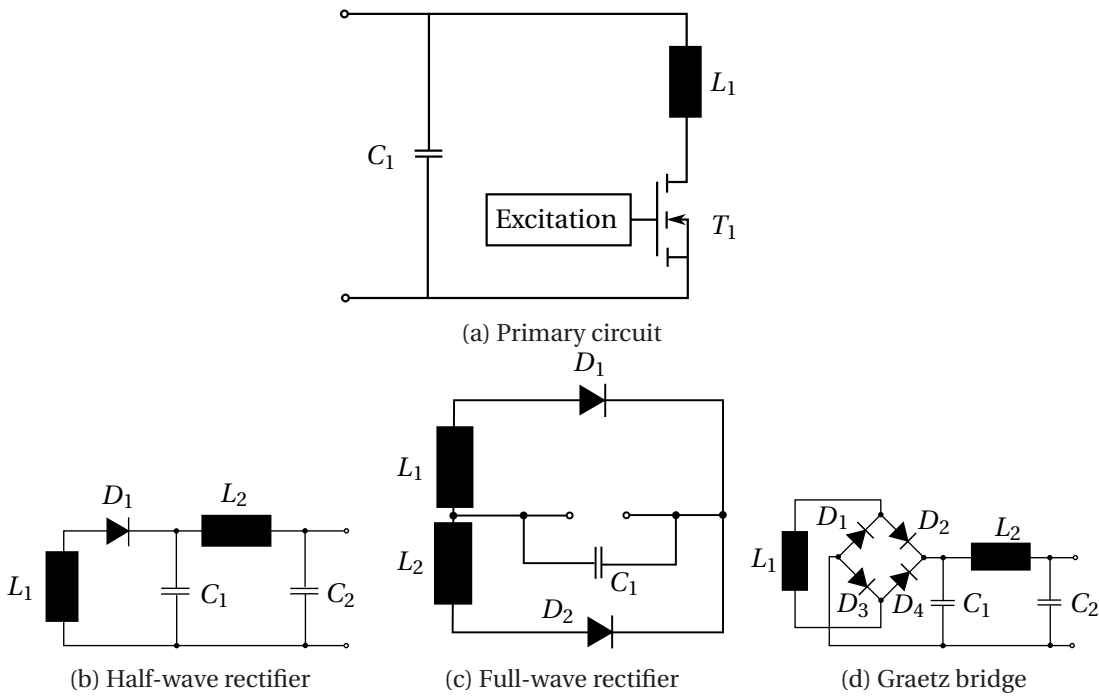


Figure 2.8 – Transformer

2.2.3 Relay

The relays are active switches where the signal is isolated from the command. As a consequence, the signal can be bidirectional for the voltage and the current. Furthermore it is also possible to control for the opening and the closing of the component. Moreover, the current can be of any amplitude or frequency as well as the voltage. As there is no current leakage when the relay is turned off, no circulating current due to this leakage, torque drop or inadvertent ignition will occur. However, it is necessary to qualify the fact that to open the relay at an inappropriate moment (when the current is not zero) would result in the apparition of spikes that will damage the contacts. Furthermore, the switching time of such component has to be taken into consideration as it is a little bit slower than other solid state switches. As shown in table 2.2, relays are sizable which can be a problem for integration.

2.2.4 Implementation

The winding reconfiguration from one configuration to another needs commutators. Depending on the number of different topologies, the number of switches varies. In [66], the author shows the necessary number of switches in function of the number of coils per phase wanted. It reveals that an increase of the number of topologies, drastically expands the number of switches required.

Table 2.3 – Number of available configurations and number of switches needed [66]

| Number of coil per phase | Number of combination | Number of switches |
|--------------------------|-----------------------|--------------------|
| 1 | 2 | 5 |
| 2 | 4 | 14 |
| 3 | 6 | 23 |
| 4 | 12 | 38 |

Note that an increase of the number of combination is not proportional with the increase of number of coils. Certain different combinations have the same properties. As result, the intrinsic characteristic of the motor is the same.

2.2.5 Choice of the solution

As shown in section 2.2.4, the number of switches is correlated to the number of wanted combinations. The number of commutators increases drastically with the number of combinations. As a consequence, mosfets are not suitable for on-board solutions because of the numerous components required for this solution. Indeed, with an important number of switches, the number of components necessary to have a four-quadrant circuit will double/quadruple as shown in fig. 2.6. Furthermore, in order to counteract the problem with the floating voltage presented in section 2.2.2, additional circuits are required. As a result, the number of components increases once again. Because of the numerous components necessary to reconfigure the winding, relays are preferred. Nonetheless, relays are voluminous. For this reason, MEMS relays are chosen.

2.3 Conclusion

Different methods to change the motor intrinsic characteristic have been presented. It is possible to modify the power supply, adapt the command or to modify the flux density or the winding configuration. Winding reconfiguration is chosen because of its ease of implementation which will not increase the motor size and because the motor efficiency will not be reduced. Furthermore, all turns will be used in order to maintain the same number of losses in the winding.

Chapter 2. State of the art

In order to reconfigure the winding, switches have been investigated. Using mosfet transistors seems to be a good solution due to their small sizes and their easy manipulations. However the number of needed circuits in order to switch the component on and off is consequent and requires a lot of space. This solution can not be an on-board solution considering the whole circuit. Besides, relays are easier to manipulate to switch the circuit on and off. However the size of these components is considerable and can hardly be used as an on-board solution. Further investigations on MEMS relays as well as its operating principle will be presented in section 4.

3 Circulating current

Contents

| | | |
|------------|--------------------------------------|-----------|
| 3.1 | Types of circulating currents | 24 |
| 3.2 | The motor | 25 |
| 3.3 | Modelling | 27 |
| 3.3.1 | The back-emf | 27 |
| 3.4 | Winding layouts | 30 |
| 3.4.1 | Radially grouped | 30 |
| 3.4.2 | Tangentially grouped | 34 |
| 3.4.3 | Generalization | 35 |
| 3.5 | Conclusion | 36 |

The geometric distribution of the turns of a reconfigurable winding shall be studied. When the coils are reconfigured in a parallel configuration e.g. star-series to star-parallel or delta-series to delta-parallel, circulating current may appear due to an unbalanced voltage between the parallel conductors. A theoretical analysis based on an analytical modelling of the motor is undertaken, after which different scenarios resulting in different winding layouts will be proposed and will be compared. Measurements performed on a prototype have been shown to support the theoretical study.

3.1 Types of circulating currents

Two types of circulating currents exist: between the phases and between the conductors as shown in fig. 3.1. A circulating current between the phases appears when the winding is in delta configuration. It can be due to the presence of triplen harmonics of the back-emf or due to eccentricities of the motor geometry, i.e. a winding distribution that is not uniform. It can appear as well when the phases are not exactly 120° spaced. On the other hand, a circulating current between conductors is caused by the distribution of the turns. For instance, if a turn is placed further from the magnet, then the linkage flux will be different. As a consequence, due to the fact that the supply voltage is the same between two parallel conductors and that the back-emf induced in each of the parallel conductors are different, a circulating current will appear to ensure that the voltage between the two parallel conductors remain the same.

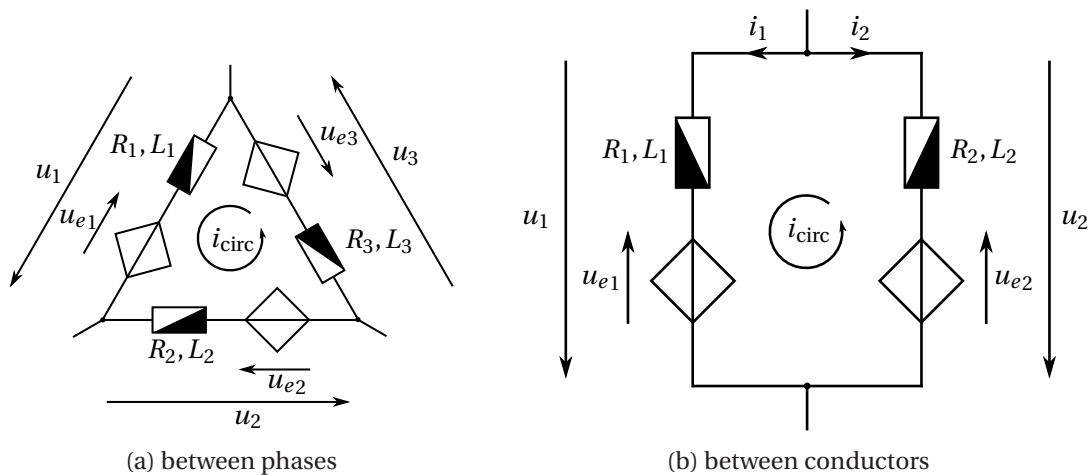


Figure 3.1 – Circulating currents

These circulating currents generate unwanted losses, which are usually neglected, as they pass through conductors. However for high speed applications, such as dental or surgical, they become significant and cannot be unheeded anymore. Frequently, parallel conductors are twisted so that both of them see the same linkage flux, which reduces the circulating currents [30]. However, this solution can be difficult to manufacture or unfit for windings made of flexPCB. Most of the studies in the field of circulating currents are carried out for motors working under faulty conditions such as static rotor eccentricity [27, 20, 91, 63, 81]. In this condition, circulating currents can be used to detect motor faults [81] or as a diagnostics tool [63]. However, in the literature, the winding distribution is always predefined and the brushless motor is always slotted. Due to emergent technologies such as flexPCB, which offer a finer control on the distribution of the turns, studying its spatial layout especially for self-supported winding, is appropriate to complete the literature on the subject.

3.2 The motor

The brushless DC motor family can be divided into two main categories: slotted brushless DC motors and slotless brushless DC motors. As explained in section 3.1, the difference of the back-emf induced in each of the parallel conductors generates circulating current. Due to the internal geometry of the motor the distribution of the flux density in the air gap is different.

- For slotted brushless DC motors, the flux mainly passes inside the teeth and there is almost no leakage flux and fringes as shown in fig. 3.2a. As a result, for the parallel conductors placed in the same slot, the distance to the magnet will have merely no influence on the flux density but depending on the distribution of the winding, the flux density may not be the same.
- As there is no iron slot for slotless brushless DC motors, the flux is distributed in the air gap as shown in fig. 3.2b. Consequently, the flux density decreases in the air gap depending on distance to the magnet. Furthermore, depending on distribution of the winding, the conductors will not see the same flux density.

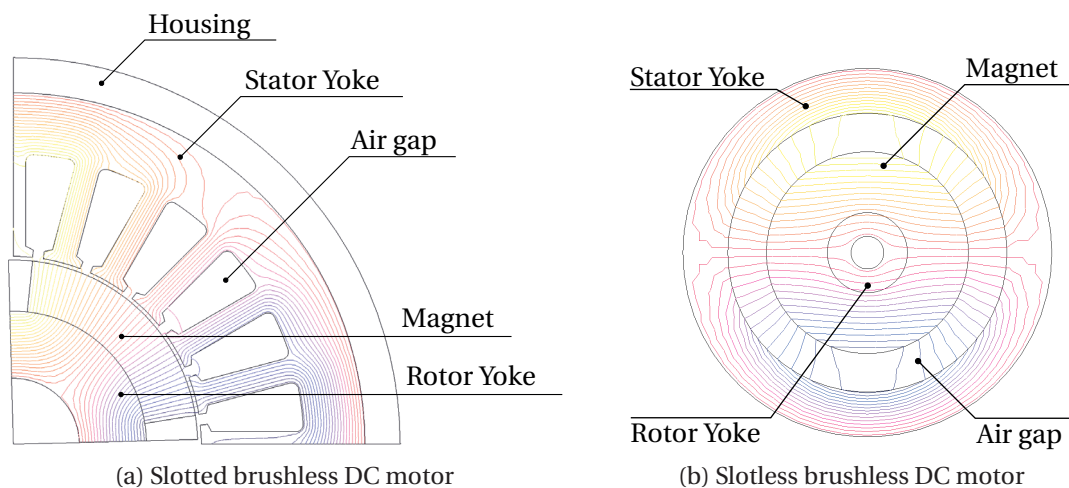


Figure 3.2 – Flux density in the motor

In this chapter, circulating current for slotless brushless DC motors is studied because the variation of the flux density in the airgap is more subtle compared to slotted ones. Furthermore, there exists different winding turn geometries [79] in this sub-family. Nonetheless, the same reasoning can be transposed for all permanent magnet brushless DC motors.

Consequently, the considered motor for the following development is a 3-phase slotless brushless DC motor, as shown in fig. 3.3. The diametrically magnetized magnet has one pair of poles and its opening completely covers the magnetic pole. The magnet is mounted on the internal rotor.

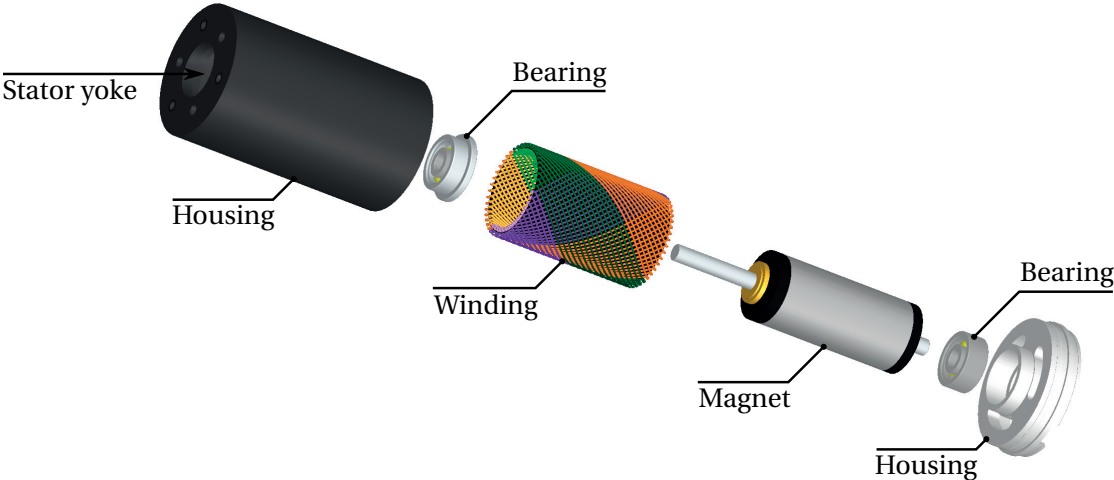


Figure 3.3 – Exploded view of the brushless DC motor

The self-supported winding is in zigzag and is regularly distributed with an angle of $\frac{2\pi}{3}$. Each phase winding has two coils placed one above the other, as represented in fig. 3.4 with the full winding representation.

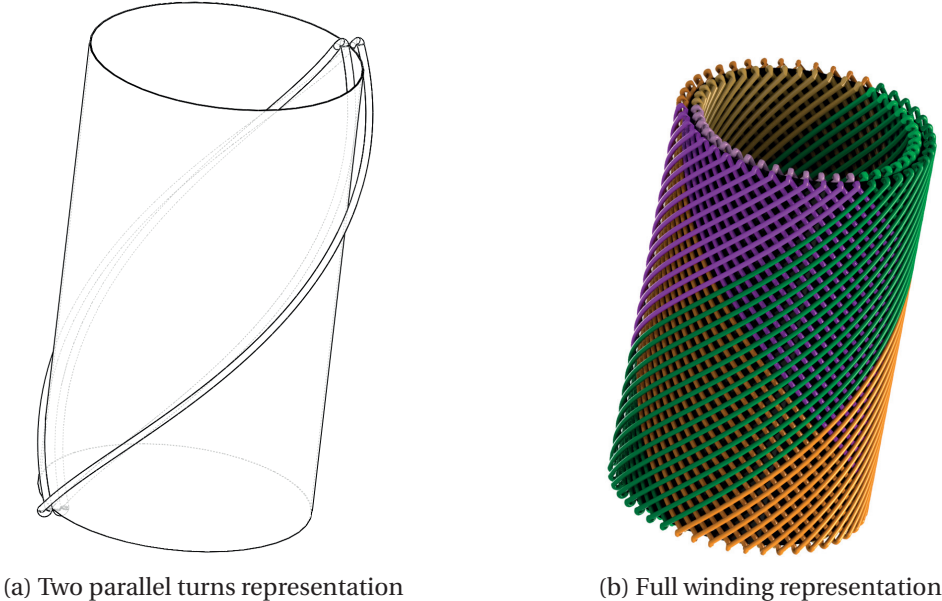


Figure 3.4 – Representation of the motor's winding

3.3 Modelling

Focusing on Kirchhoff's voltage law, the parallel circuit presented in fig. 3.1b can be expressed as follows:

$$u_1 = R_1 \cdot i_1 + L_1 \frac{di_1}{dt} + M \frac{di_2}{dt} + u_{e1} \quad (3.1a)$$

$$u_2 = R_2 \cdot i_2 + L_2 \frac{di_2}{dt} + M \frac{di_1}{dt} + u_{e2} \quad (3.1b)$$

where u and R are the conductor voltage and its resistance, i is the current flowing through the conductor, and u_e is the generated back-emf.

As the end connections of the parallel conductors are connected, the voltage is fixed: $u_1 = u_2$. Consequently, considering that the impedance is identical for each of the conductors, two cases can be considered:

- if $u_{e1} = u_{e2}$, there is no circulating current,
- if $u_{e1} \neq u_{e2}$, a circulating current appears in order to ensure the condition $u_1 = u_2$.

As a result, the back-emf will be modelled and different winding configurations will be tested in order to reduce circulating currents.

For the upcoming development, several hypotheses are made:

1. the impedance is the same for each coil,
2. the dimensions of the motor are flawless,
3. the leakage flux and the fringes are not considered,
4. the permeability of the iron is considered to be ideal ($\mu_{\text{iron}} = \infty$),
5. the magnet is diametrically polarised and completely covers the magnetic pole,
6. the magnetic quantities only involve the permanent magnet and do not take into account the influence of the winding.

3.3.1 The back-emf

According to Lenz's law, a variation of a magnetic flux inside a conductor produces an electromotive force. For the motor, the permanent magnet produces a magnetic flux between the rotor itself and the stator yoke. As the winding is placed in the air gap, the magnetic flux flows

Chapter 3. Circulating current

through it and, as the motor rotates, the magnetic poles are cycled sequentially, which produces this variation. As a consequence, the back-emf model can be derived from the magnetic flux. Usually, the latter is evaluated through the vector potential (\vec{A}) which is defined as shown in eq. (3.2) and in eq. (3.3).

$$\nabla \times \vec{A} = \vec{B} \quad (3.2)$$

$$\nabla \cdot \vec{A} = 0 \quad (3.3)$$

As the presented motor is a cylinder and due to the stated hypotheses 2, 3, 4 and 6, the vector potential defined in this frame is:

$$A_z(r, \varphi) = \sum_{n=1}^{\infty} f(r) \cdot g(\varphi) = \sum_{n=1}^{\infty} (a_n r^n + b_n r^{-n}) \cdot (c_n \cos(n\varphi) + d_n \sin(n\varphi)) \quad (3.4)$$

with a_n , b_n , c_n and d_n some constants and φ the abscissa of the polar coordinates. To simplify the presentation, only the main results are reported here. The full development is presented in appendix A.

As:

- $A_z(r, \varphi)$ is a odd function
- $A_z(r, \varphi)$ has a zero mean value

The following equation can be formulated:

$$A_{z_i}(r, \varphi) = (e_i r + f_i r^{-1}) \cdot \sin(\varphi) \quad (3.5)$$

where i stands for the domain in which the vector potential is evaluated.

As a result using the parametrization shown in fig. B.1 (see appendix B), the vector potential for the motor in the air gap is:

$$A_{z_3}(r, \varphi) = (e_3 r + f_3 r^{-1}) \cdot \sin(\varphi) \quad (3.6)$$

with:

$$e_3 = B_0 \frac{r_2^2 (r_1^2 - r_2^2)}{(r_1^2 + r_2^2) \left[\mu_0 \mu_{dr} (r_2^2 - r_3^2) + \frac{r_1^2 - r_2^2}{r_1^2 + r_2^2} (r_2^2 + r_3^2) \right]} \quad (3.7a)$$

$$f_3 = e_3 \cdot r_3^2 \quad (3.7b)$$

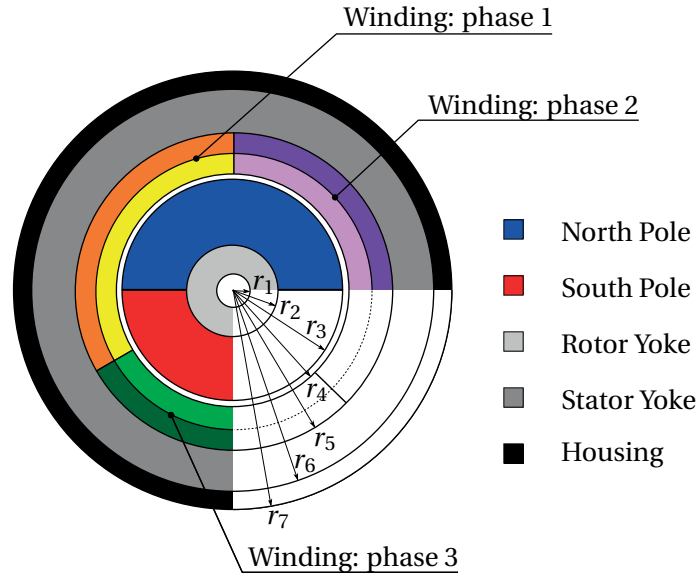


Figure 3.5 – Internal radius parametrization

Note that due to the definition of the vector potential stated in eq. (3.2)

$$\vec{B} = \nabla \times \vec{A} = \begin{bmatrix} \frac{1}{r} & 1 & \frac{k}{r} \\ \frac{\partial}{\partial r} & \frac{\partial}{\partial \varphi} & \frac{\partial}{\partial z} \\ A_r & A_\varphi & A_z \end{bmatrix} = \begin{bmatrix} \frac{1}{r} \frac{\partial A_z}{\partial \varphi} \\ -\frac{\partial A_z}{\partial r} \\ 0 \end{bmatrix} \quad (3.8)$$

the radial component of the flux density in air gap is:

$$B_r(r, \varphi) = \frac{1}{r} \frac{\partial ((e_3 r + f_3 r^{-1}) \cdot \sin(\varphi))}{\partial \varphi} = (e_3 + f_3 r^{-2}) \cdot \cos(\varphi) \quad (3.9)$$

Now that the flux density has been evaluated with respect to the internal geometry of the motor, the back-emf can be found while not considering the iron saturation.

$$u_e = \frac{\partial \Psi}{\partial t} = N \frac{\partial \Phi}{\partial t} \quad (3.10)$$

with

$$\Phi = \iint_A \vec{B} ds \quad (3.11)$$

The surface integration of the flux for a zigzag winding has already been presented in [79]. The full development will not be shown here. However, in the studied configuration, different combinations and dispositions of the winding do not produce the same total flux. As a consequence, the flux density taken at the middle of the phase can not be calculated as presented in [79], but it has to be adapted for each turn and their back-emf has to be summed.

A summary of the parametrization used for the previous calculations is illustrated in fig. 3.6.

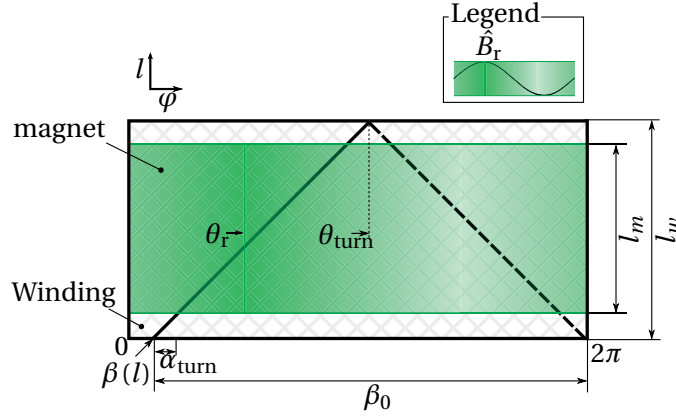


Figure 3.6 – Parametrization of the winding

$$\Phi_{\text{turn}}(B_r, \theta_r) = \int_{-\frac{l_m}{2}}^{\frac{l_m}{2}} \int_{\theta_{\text{turn}} - \frac{\beta(l)}{2}}^{\theta_{\text{turn}} + \frac{\beta(l)}{2}} \hat{B}_r(r) \cos[(\varphi - \theta_r)] d\varphi dl \quad (3.12a)$$

$$= \frac{8\hat{B}_r l_w}{\beta_0} \sin\left(\frac{\beta_0}{4}\right) \sin\left(\frac{\beta_0 l_m}{4l_w}\right) \cos(\theta_{\text{turn}} - \theta_r) \quad (3.12b)$$

The total flux for a turn is:

$$\Psi(B_r, \theta_{\text{turn}}, N) = \sum_{k=0}^{N-1} \Phi_{\text{turn}}(B_r, \theta_{\text{turn}}) = \sum_{k=0}^{N-1} \Phi_{\text{turn}}\left(B_r, \theta_b + \alpha_{\text{turn}}\left(k - \frac{N-1}{2}\right)\right) \quad (3.13)$$

The back-emf is obtained using eq. (3.10) and eq. (3.13)

$$U_e = \frac{\partial \Psi(B_r, \theta_{\text{turn}}, N)}{\partial t} = \frac{\partial (\hat{\Psi} \cos(\theta_{\text{turn}} - \theta_r))}{\partial \theta_r} \frac{\partial \theta_r}{\partial t} = -\Omega \hat{\Psi} \sin(\theta_{\text{turn}} - \theta_r) \quad (3.14)$$

3.4 Winding layouts

Two different winding layouts are conceivable in order to place the turns in parallel. It is possible to group them either radially or tangentially as shown in fig. 3.7.

3.4.1 Radially grouped

The simplest solution for this configuration is to split the winding in two parts radially. Each of these parts forms a coil that covers the phase completely. The parts are connected in parallel. One coil is closer to the magnet than the other one. This implies that the amplitude of the flux density seen by each coil is not the same. Consequently, as revealed by equations (3.12b), (3.13) and (3.14), the back-emf is different for each layer of the coil as well. Note that the closer the coil is to the magnet, the higher the back-emf amplitude will be and reciprocally as shown

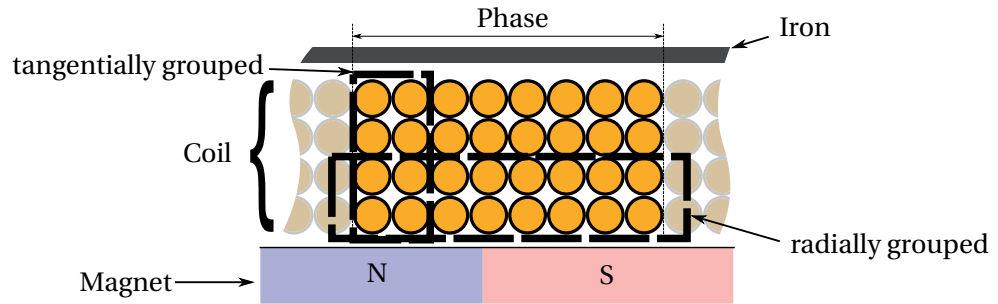


Figure 3.7 – Choice of spatial distribution of the winding - Cross section

in fig. 3.8a. In this figure, the back-emf is given as a function of the rotor position with respect to the position of the center of the coil. The simulated motor turns at a speed of 3'000 rpm.

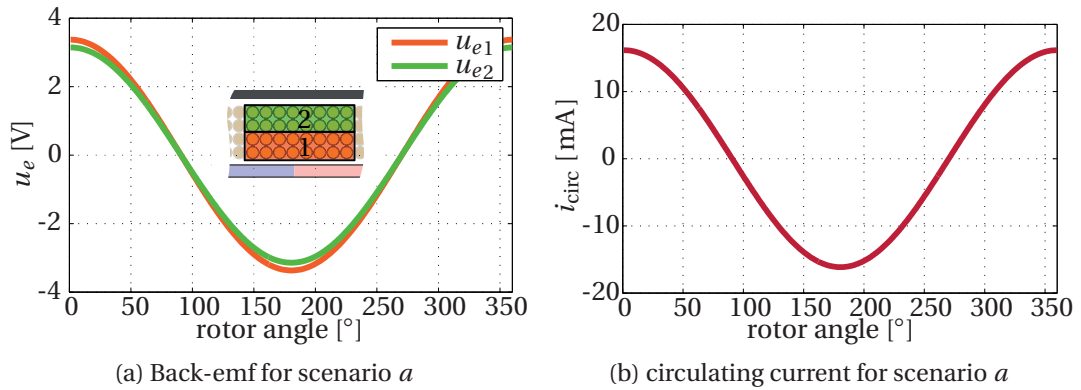


Figure 3.8 – Results for scenario *a* - radially grouped

In order to confront the analytical results to the measurements, the motor presented in 3.2 is used. It is driven by a DC motor and the back-emf is measured and compared to the model as shown in fig. 3.9.

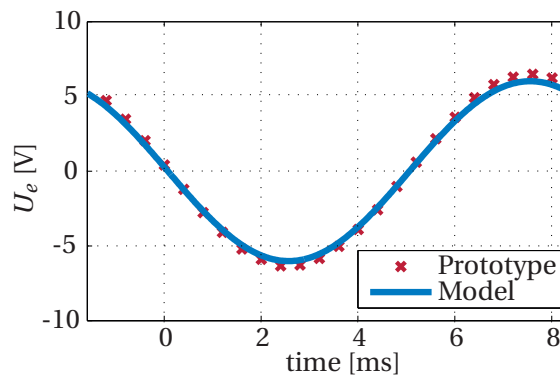


Figure 3.9 – Comparison of the back-emf between the model and the measurements

A relative error of 5.09% between the model and measurements is found. This difference can be explained by the fact that the leakage flux and the fringes are not considered in the

Chapter 3. Circulating current

model and that the dimensions are considered flawless. In reality, during fabrication of the self-supported winding, the latter is heated and compressed. As a result, asymmetries may appear, which may lead to a phase that is displaced further or closer than originally predicted. This is revealed by the measurement performed on each separated winding where (a) stands for closer conductors and (b) stands for further conductors, as shown in fig. 3.10.

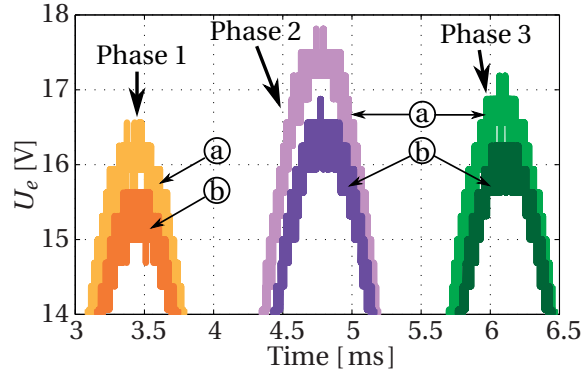


Figure 3.10 – Back-emf for each conductor at 15'000 rpm

As expected, circulating currents appear due to the difference in the amplitudes of the back-emf. In fig. 3.11, the motor is rotating at 3'000 rpm.

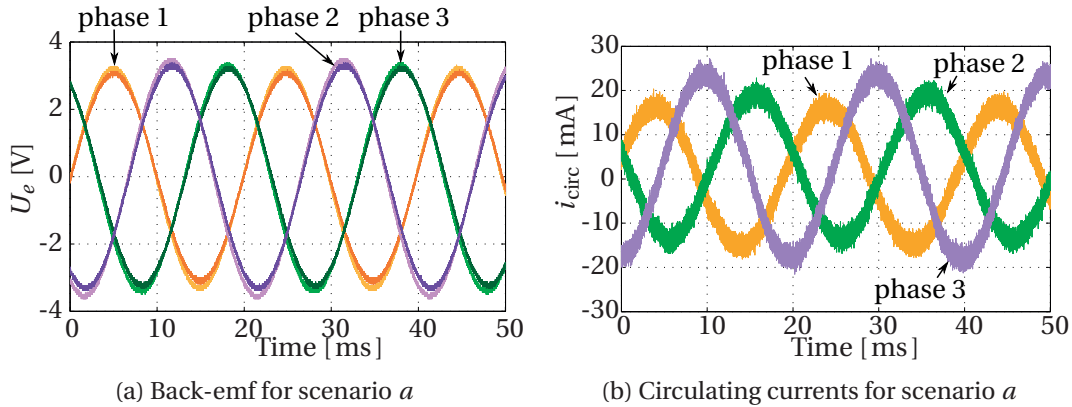


Figure 3.11 – Results for scenario *a* - radially grouped

In table 3.1, the phase resistances of the prototype are reported and the Joule losses are evaluated.

Table 3.1 – Joule losses at 3000 rpm

| | phase 1 | phase 2 | phase 3 |
|-----------------------|---------|---------|---------|
| R [Ω] | 12.51 | 12.59 | 13.23 |
| I_{rms} [mA] | 11.8 | 12.6 | 14.9 |
| P_j [mW] | 1.7 | 2.0 | 2.9 |

Due to the difference of the phase resistance and to the fact that the back-emf do not have

the same amplitude for each phase, the circulating currents do not have the same amplitude as well. As a result, Joule losses are not exactly the same. For 3000 rpm, Joule losses between 1.7-2.9 mW have been found. By rotating the motor faster, the circulating current increases with the rise of the amplitude difference of the back-emf as shown in fig. 3.12.

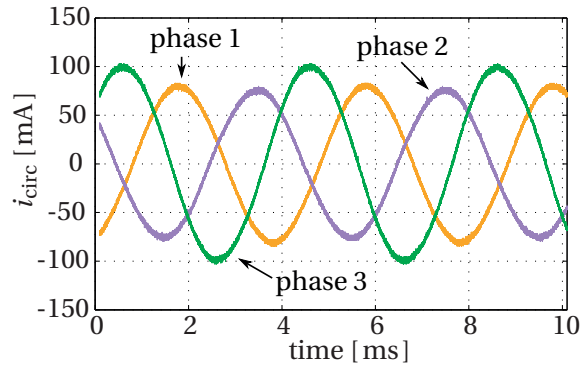


Figure 3.12 – Circulating current at 15'000 rpm

As shown in fig. 3.12, by increasing the speed of the motor by a factor of 5 (from 3'000 rpm to 15'000 rpm), Joule losses increase by a factor 25. As expected, the amplitude of the circulating current is proportional to the rotating speed. This motor can reach up to 30'000 rpm, which means that the losses will be 100 times higher.

In order to reduce the losses, it is possible to split the phase winding in four parts instead of two and combine them in parallel. More combinations are possible as shown in fig. 3.13 and fig. 3.15. Three cases can be considered:

1. coils 1 and 2 in series, in parallel with coils 3 and 4 in series [scenario *b*],
2. coils 1 and 3 in series, in parallel with coils 2 and 4 in series [scenario *c*],
3. coils 1 and 4 in series, in parallel with coils 2 and 3 in series [scenario *d*].

Note that by placing coils 1 and 2 in series, in parallel with coils 3 and 4 in series, gives the same result as dividing the winding into two parts.

The different scenarios are compared and the results for the circulating currents are shown in fig. 3.13. This figure shows that the circulating current can decrease according to the combination used to place the turns in parallel. In the case of scenario *d*, there is nearly no circulating current because the back-emf amplitudes and phases are almost the same for each winding. As a consequence, the circulating current in scenario *d* is decreased by a factor of 110 compared to the one of scenario *b*.

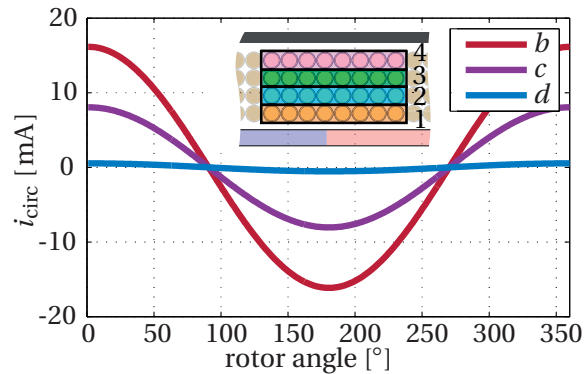


Figure 3.13 – Circulating current for scenario *b* , *c* and *d* - radially grouped

3.4.2 Tangentially grouped

It is also possible to combine the turns tangentially, as shown in fig. 3.7. Contrary to the radially grouped winding, each group of turns sees the same magnetic flux intensity. However, as they are spatially distributed, each group of turns does not see the same variation of magnetic flux at the same time. As a result, a phase shift in the back-emf appears between the groups of turns as shown in fig. 3.14a resulting in the apparition of a circulating current as shown in fig. 3.14b. In this figure, the phase winding is split into two parts in the middle of the phase.

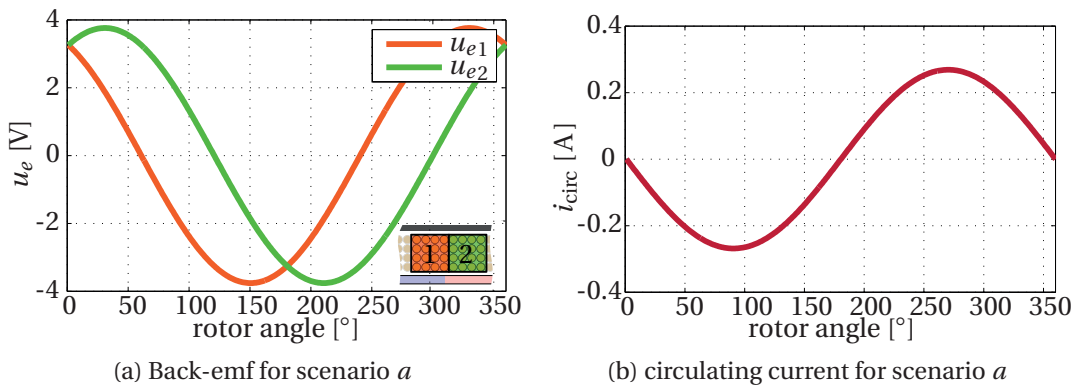
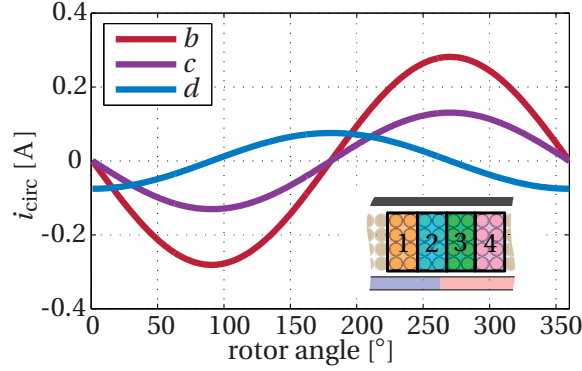


Figure 3.14 – Results for scenario *a* - tangentially grouped

Once again, by splitting the winding into four parts instead of two, more combinations are possible to reduce the circulating currents. The same scenario presented for radially grouped turns can also be used for tangentially grouped turns. The results of the different scenarios are given in fig. 3.15

The scenario *b* gives the same results as scenario *a* because the turns are arranged in the same manner. By comparing scenario *b* and scenario *d* , the amplitude of the circulating current is reduced by a factor of 4 due to the reduction of the phase-shift between the generated back-emf.


 Figure 3.15 – Circulating current for scenario b , c and d - radially grouped

3.4.3 Generalization

As shown in the two studied cases, circulating currents can have two different origins. If there is a difference of amplitude of the back-emf between two parallel conductors, or if there is a phase shift between them due to the arrangement of the turns or to manufacturing imperfections, all of these can generate circulating currents in the winding. For two parallel conductors, circulating currents are expressed as shown in eq. (3.15).

$$i_{\text{circ}} = \frac{1}{R_1 + R_2} \sqrt{U_{e1}^2 + U_{e2}^2 - 2U_{e1}U_{e2} \cos(\gamma)} \cdot \sin \left(\omega t + \tan^{-1} \left(\frac{\frac{U_{e2}}{R_2} \sin(\gamma)}{\frac{U_{e2}}{R_2} \cos(\gamma) - \frac{U_{e1}}{R_1}} \right) \right) \quad (3.15)$$

where γ is the electric phase shift between the two back-emf.

Radially grouped

When the conductors are radially grouped, there is no phase shift between them if the dimensions of the motor are ideal ($\gamma = 0$). As a consequence, eq. (3.15) is simplified as shown in eq. (3.16) considering that the impedance is the same between the two conductors.

$$i_{\text{circ}} = \frac{U_{e2} - U_{e1}}{2R} \cdot \sin(\omega t) \quad (3.16)$$

This implies that in order to reduce the circulating current, the difference of amplitude of the back-emf between the two groups of turns have to be reduced as well. Furthermore by having more groups of turns, it becomes easier to fine tune this difference of amplitude.

Tangentially grouped

When the conductors are tangentially grouped, each group of turns has the same back-emf ($U_{e1} = U_{e2} = U_e$). However, the phase angle is not the same for each one of them. As a result, eq. (3.15) is simplified as shown in eq. (3.17).

$$i_{\text{circ}} = \frac{1}{2R} \sqrt{2U_e^2 (1 - \cos(\gamma))} \cdot \sin\left(\omega t + \tan^{-1}\left(\frac{\sin(\gamma)}{\cos(\gamma) - 1}\right)\right) \quad (3.17)$$

In order to reduce the circulating current when the turns are tangentially grouped, eq. (3.17) implies that γ should be as small as possible. The optimal solution to attain this goal is to twist the parallel conductors [30]. Nonetheless, the winding takes more placed, which reduces the copper filling factor. Furthermore, for flexPCB technology, the turns of the parallel conductors have to be placed one after the other as the turns can not be twisted.

3.5 Conclusion

A circulating current appears in two parallel conductors when the back-emf are not the same. It comes from a difference of amplitude or a phase shift between the two back-emf of the conductors. Contrary to studies found in the literature which focus on the appearing of circulating current due to rotor eccentricity or are used as a fault detection tool, this chapter deals with the apparition of the circulating current between conductors due to the spatial distribution of the turns specially for slotless brushless DC motor. The parallel conductors can be twisted to avoid this problem even if the copper filling factor is reduced. However, when it is not possible - e.g. twisted or the winding is in flexPCB - due to manufacturing reasons, the arrangement between the two conductors is important. They can be arranged radially or tangentially. The modelling has proved that the circulating current can be reduced. If the conductors are radially distributed, the circulating current can be reduced if the amplitude of the back-emf of each conductor is the same. In subdividing the winding into four parts the circulating current can be reduced by a factor of 110. If the conductors are tangentially distributed, the circulating current can be reduced by distributing the turns for each conductor. As a result the phase shift between them will decrease.

Publication related to this chapter:

- F. Copt, C. Koechli and Y. Perriard, Study on the Layout of the BLDC Motor's Winding in Order to Minimize the Circulating Current, The Seventh Annual IEEE Energy Conversion Congress & Exposition (ECCE 2015), Montreal, Canada, September 20 - 24, 2015.

4 Design of the MEMS relay

Contents

| | |
|--|-----------|
| 4.1 Introduction | 38 |
| 4.1.1 MEMs relays technologies | 38 |
| 4.1.2 Existing geometry in electrostatic MEMs | 45 |
| 4.2 Design | 47 |
| 4.2.1 Resistance of the relay | 48 |
| 4.2.2 Modelling using the Lagrange formulation | 55 |
| 4.2.3 Breakdown voltage | 62 |
| 4.2.4 Dynamic response analysis | 63 |
| 4.2.5 Modal analysis | 66 |
| 4.3 Design example | 66 |
| 4.3.1 Influence of the microfabrication tolerances | 67 |
| 4.4 Summary and conclusion | 69 |

In this chapter, the design of the relay which will be used to dynamically reconfigure the winding is pursued. The environmental constraints linked to the integration in the motor limit the choice of the actuation scheme. The latter will be discussed and the most fitting solution will be highlighted.

In order to design the relay, different aspects such as the contact and the mechanical structure will be discussed to define its dynamic and its electrical properties.

Finally, as it is intended to manufacture the relay using cleanroom fabrication techniques, the influence of the limitation of these techniques on the characteristics of the relay will be explored.

4.1 Introduction

4.1.1 MEMs relays technologies

The MEMs relay family can be divided into two categories: Ohmic and Capacitive.

Capacitive switches are frequency switches that work through a variation of their capacitance. Their bandwidth can be adapted in moving their electrodes closer or further to each other.

Conversely, ohmic switches consist in mechanical on/off switches that drive or stop the connections between two tracks. This is the type of behavior expected in this project. Several actuation schemes are conceivable: electrothermic, shape-memory alloy, piezoelectric, electrostatic and electromagnetic.

Thermal

Under heat, solids deform and elongate proportionally to their thermal coefficient. While considering thermal stain, Hooke's law is expressed as shown in eq. (4.1) [22].

$$\epsilon = \epsilon_{\text{Mechanic}} + \epsilon_{\text{Thermal}} = \frac{\sigma}{E} + \alpha \Delta T \quad (4.1)$$

with ϵ , σ , α , E and T respectfully stand for the strain, the stress, the thermal coefficient, the Young modulus and the temperature.

Thermal switches use this deformation to connect a deformed part with a static part. Two possibilities exist: with one material or with the combination of two different materials. If the second possibility is chosen, the two materials will deform but the strain will not be the same. This difference in the deformation will force the structure to bend. Using this principle, a moving plate can be set into motion and a connection can occur. This methodology has already been used in [77] (fig. 4.1). This relay could drive a 3 A current and switch at a frequency of 5 Hz while locally increasing the temperature to 220 °C for the deformation. In order to keep the contacts closed without constantly heating the beams, it is possible to use a latching system composed of two separated beams placed at 90 degree from each other [6] (fig. 4.2). After activation, a constant deformation is kept, which generates a permanent force between the contacts because of the beam stiffness.

The switching time of thermal actuators depends on the thermal resistance and on the thermal capacity. A low thermal resistance implies a faster actuation. Nevertheless, the power needs to be increased in order to produce sufficient Joule losses to heat up.

The main advantage of the electrothermal actuator is its simplicity of fabrication. However, the power needed to heat the actuator is relatively high. Furthermore, because of the slow time response of the order of hundreds of milliseconds as well as the thermal environment in which the relay will be integrated, this solution is not suitable.

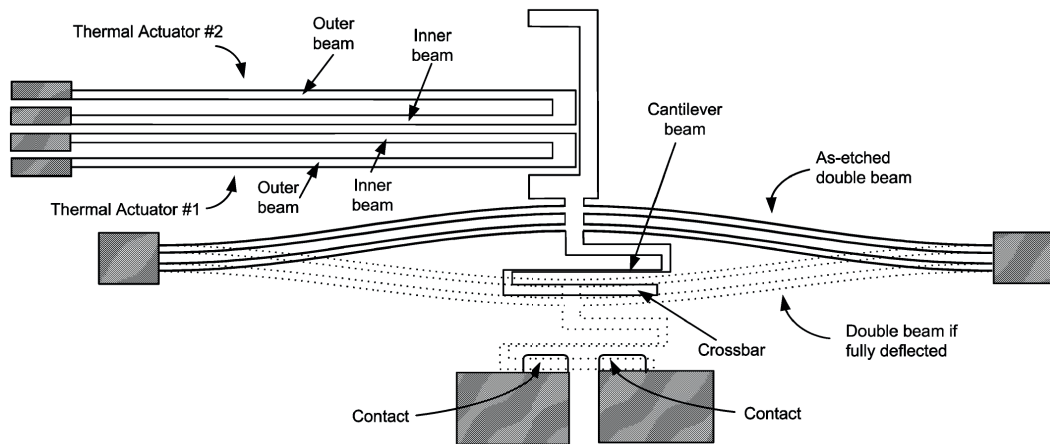


Figure 4.1 – Bi-material thermal switch [77]

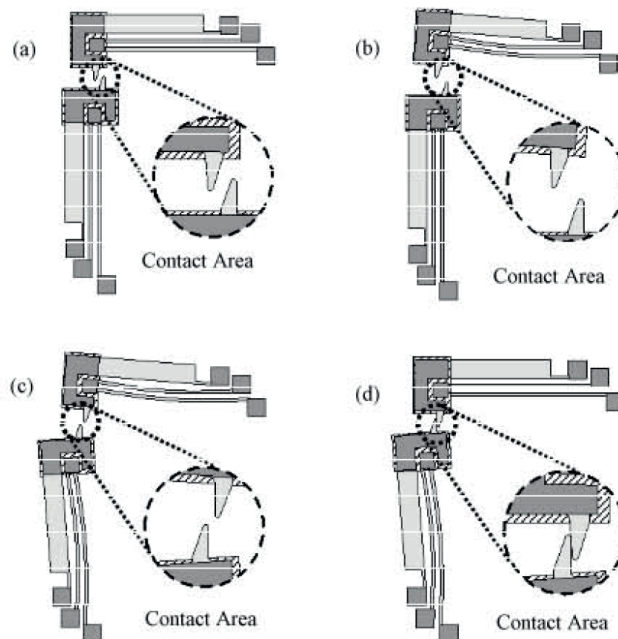


Figure 4.2 – Thermal latch principle [6]

Shape-Memory alloy

Shape-memory alloy (SMA) has also been used as a MEMS relay [2]. Its mechanical scheme works in three steps. Firstly, the SMA is in the twinned Martensite-phase (M-phase). When a stress is applied, the SMA is deformed and becomes detwinned in the M-phase. As the SMA is heated, it transforms from the M-phase to the Austenite-phase (A-phase). This results in recovery of the strain caused by the previously applied stress. Lastly, as it cools down, the SMA reverts back to the twinned M-phase where it can be deformed once again. In terms of performance, such material has a slow response time in the range of 0.1 second [104] to the

seconds [72, 73]. SMA works well below 100°C but some of them can be activated at higher temperatures [35].

Piezoelectric

Another possible actuation scheme is the use of a piezoelectric actuator. Under an electric field, mechanical strains occur and deform the piezoelectric component expressed in eq. (4.2) [1].

$$\begin{cases} \mathbf{S} = \mathbf{s}\mathbf{T} + \mathbf{d}^t \mathbf{E} \\ \mathbf{D} = \mathbf{d}\mathbf{T} + \boldsymbol{\epsilon}\mathbf{E} \end{cases} \quad (4.2)$$

with S for the strain, s for the elastic compliance, T for the stress, d for the strain constant, E for the electric field, D for the electric charge density displacement, ϵ for the permittivity .

Two possibilities exist in order to use piezoelectricity as an actuation mechanism: a direct use of the piezoelectricity or using a mechanical amplifier.

Usually piezoelectric displacements are small. In order to have a high pressure, the strain has to be as low as possible or the voltage needs to be increased. In order to increase both the displacement and the insulation together, it is possible to stack multiple layers of piezoelectric material, each subject to the same applied voltage, in order to increase the displacement. Nonetheless, it is complex to fabricate.

Using the mechanical amplifier technique, a bending moment can be created in order to activate the switch [53, 76, 8]. Fig. 4.3 shows an example of design [53]. In this example, 2.5 V were necessary to activate the switch for 3 μm of displacement and could switch on in 4 μs . A similar switch has been designed [76], that has two activation voltages as shown in fig. 4.4. In the literature, low contact resistance found for this scheme are usually between 7 (for 55 V [75]) and 35 Ω (for less than 5 V [76]). The lowest contact resistance reported is 0.1 Ω [90]), but in this example no information is given on the actuation voltage. Note that lower contact resistance should be obtained using a direct actuation. Furthermore, no optimization of this resistance has been found in the literature. In [8], it has been shown that a piezoelectric actuator can sustain a current amplitude of 1 A at a frequency of 10 MHz.

The piezoelectric switches have a fast response, a low power consumption, and a low wear because there is no moving part apart from the deformation of the piezoelectric itself. However, its contact resistance is high compared to those obtained under electromagnetic and electrostatic actuation.

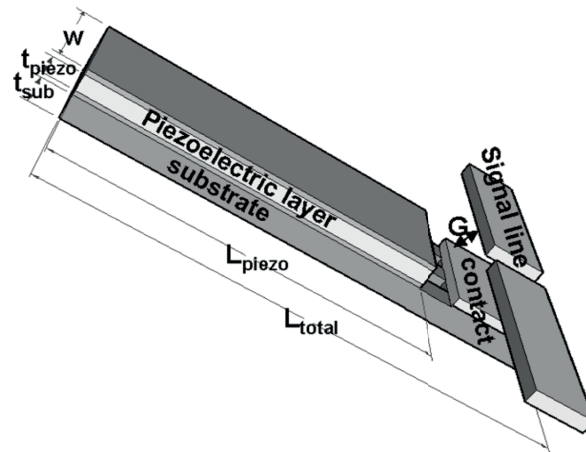


Figure 4.3 – SPST MEMs [53]

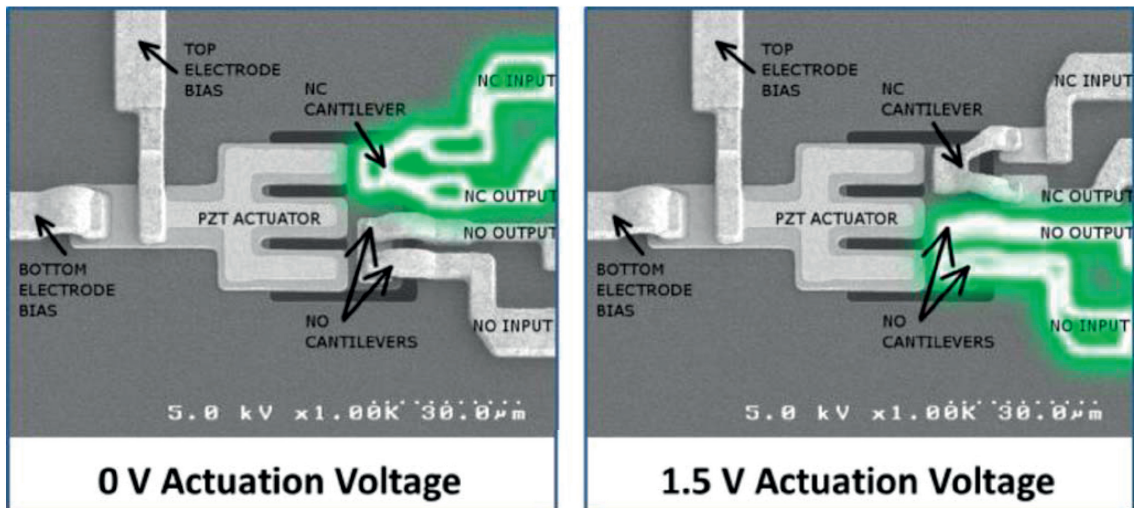


Figure 4.4 – SPDT MEMs [76]

Electromagnetic

A relay can be turned on using a combination of a magnet, a ferromagnetic part or a coil. The applied force can be evaluated from the energy density (W) [44]:

$$\vec{F} = -\nabla(W_{\text{magnetic}}) \quad (4.3)$$

with

$$W_{\text{magnetic}} = \int_V \int_0^B \vec{H} d\vec{B} dV \quad (4.4)$$

where H and B are respectively the magnetic field and the magnetic flux density

Chapter 4. Design of the MEMS relay

There are two types of magnetic MEMS relays. Reed switches (fig. 4.5) are standalone devices for which the actuation part is external to the cantilever. They can be activated by an external magnet, a current flowing in the coil or a combination of both. Reed relays are a monolithic version of the Reed switches including both the switching part and the activation part (4.6).

Reed switches are usually composed of a cantilever and two alloy parts made of iron and nickel. Under a magnetic field, these two parts will be attracted to each other and a connection will occur. When the magnetic field is removed, due to the spring force of the beam, the connection will cease.

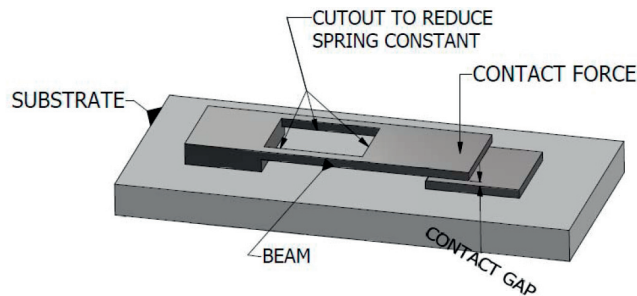


Figure 4.5 – MEMS reed switch (the external magnet or coil is not represented) [19]

As said, Reed relays are a monolith version of the reed switches. The internal activator coil can have different shapes such as helicoidal [31], meander [100] (fig. 4.6a) or planar [16] (fig. 4.6b). Under a constant magnetic field, a magnetic force is created by supplying the coil. The cantilever is then set into motion until the switch is turned on. Another possibility is to use the electromagnet principle. By using a magnetic circuit and a coil, it is possible to attract the free magnetic circuit part to reach a contact and switch on the device.

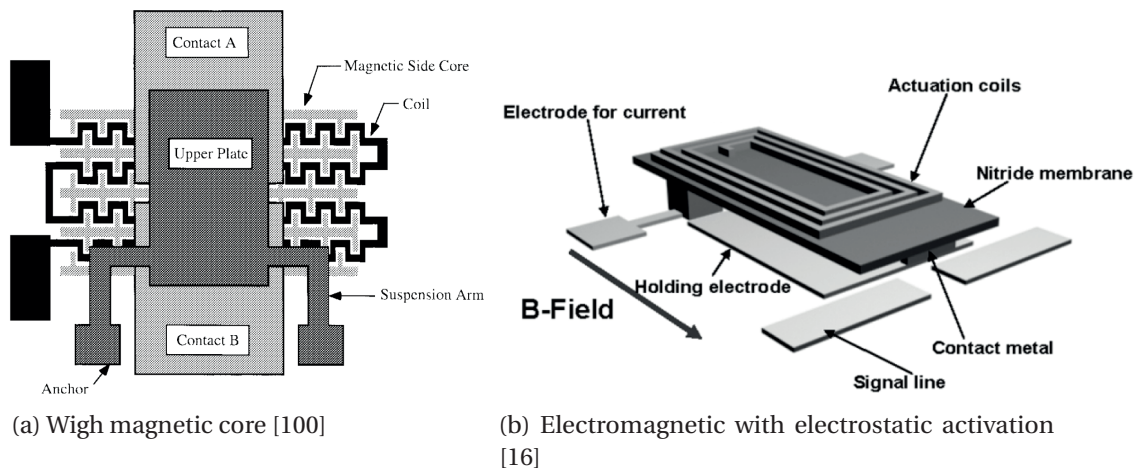


Figure 4.6 – Reed relay

The main issue with electromagnetic reed relays is the constant current feed needed. For this reason, methods mixing electrostatic and electromagnetic have appeared [16]. By using

the larger force offered by electromagnetic actuators, it is possible to have large gaps. Then by using the electrostatic forces, it is possible to keep the connection close with low power consumption (leakage current). The environment in which the relay will be placed is magnetic. As a consequence flux leakage from the magnet rotor can influence the relay. Therefore, an additional shielding may be required.

Electrostatic

The electrostatic actuation scheme is the most used because of its low power consumption, fast response and also because its fabrication is complementary with CMOS technology. This method uses the electrostatic force between two electrodes in order to move them. The force is given by [44]:

$$\vec{F} = -\nabla (W_{\text{electric}}) \quad (4.5)$$

with

$$W_{\text{electric}} = \int_V \frac{\epsilon_0}{2} |\vec{E}|^2 dV \quad (4.6)$$

where ϵ_0 is the vacuum permittivity and E is the electric field.

The electrostatic force depends on the surface of the plate, the voltage, the distance between the two plates and the material between them. For a given distance a trade off between the surface of the plate and the actuation voltage needs to be made if the total surface of the switch or its electronics are limited. Note that the voltage can not be indefinitely increased. Indeed, electrostatic breakdown can occur. This limit is illustrated by the modified Paschen curve [105].

There are two main types of electrostatic actuators: broadside MEMs-series (fig. 4.7a) and incline MEMs-series switches (fig. 4.7b). For broadside switch, the contact region is located at the end of the cantilever. While the switch is on, the contact part moves until it reaches the contact tracks. For the incline switch, the connection is made through the beam.

In order to activate the MEMs, it is possible to lower the threshold voltage using an adequate mechanical system such as torsion springs and leverage [36]. Note that, the gap between the cantilever and the contact should be large enough for RF isolation. Furthermore, it has been shown that electrostatic MEMs relay can bear currents of amplitudes between 1-2.6 A [71].

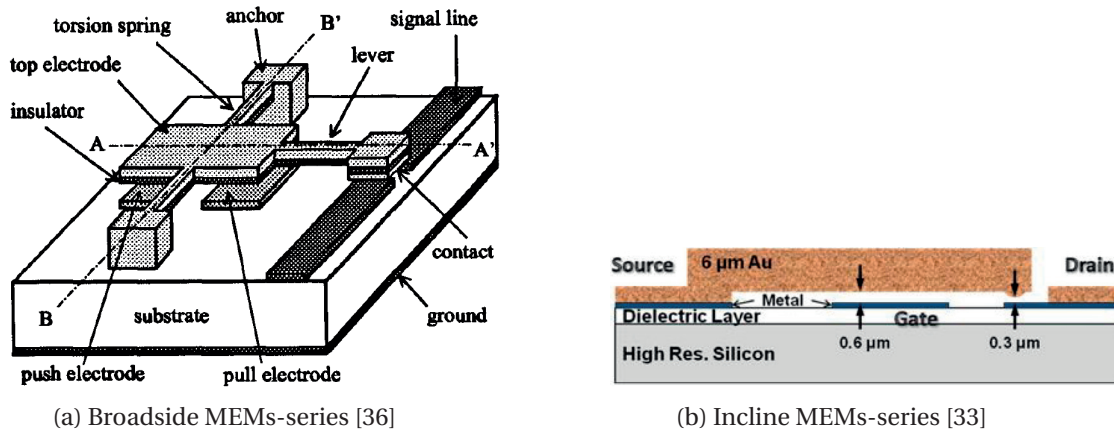


Figure 4.7 – Electrostatic MEMS

Choice of the switch technology

Table 4.1 compares the different activation schemes possible for MEMS relays

Table 4.1 – Summary of the MEMS relay values found in the literature

| | Thermal | SMA | Piezoelectric | Magnetic | Electrostatic |
|---|------------------|-----------------|----------------------|------------------------|-------------------|
| Switching time [μs] | 200-3000 | $>1 \cdot 10^6$ | 0.1-4 | 200-5000 | 0.1-5 |
| Activation | 10-100mA | $>100\text{mA}$ | 1.5-10V | 10-100 mA 30-200 mT | 6-80 V |
| Contact resistance [$\text{m}\Omega$] | 60-300 | <1000 | 100-4000 | 20-500 | 15-1500 |
| Force | μN -N | $>\text{mN}$ | $10 \mu\text{N}$ -mN | mN | μN -mN |

As discussed previously, electrothermal MEMS switches are easy to fabricate, however the power consumption needed is high and devices are used at a slow rate (1-10 Hz). Furthermore, this technology is thermal dependant, which makes it unwise. The actuation time of the SMA is so slow that it removes this actuation scheme from the possible solutions. Piezoelectric MEMS switches have a low consumption and can switch fast (0.1-10 μs). However, they are usually used for small gaps. If a higher distance gap is needed, the activation voltage increases. Nevertheless it is possible to reduce the activation voltage using a mechanical amplifier. Furthermore, a high displacement means a reduction of the output force and as a consequence an increase of the contact resistance. This technology is also complex to manufacture [54]. For these reasons, these three actuation schemes will not be considered.

Electromagnetic MEMS switches need a constant current feed if not coupled with an electrostatic latch but offer the possibility to have a higher gap than electrostatic MEMS switches system. Magnetostatic solutions have the drawback of being influenced by the motor magnet and also need a constant current supply. Fig. 4.8b shows the variation of flux density under the motor in function of the distance using FEM. If the switches are placed 3 mm away from the stator yoke, the flux density is around 15 mT. In the literature, the flux density necessary to switch is about 200 mT [100] for a coil and magnetic circuit switch. This means that the switch

will be slightly influenced (7.5%) by the magnet. As the flux is variable, a special care has to be taken in order to avoid resonance. Nevertheless, a small disc of iron can be added between the switches and the motor in order to isolate them. If this solution were to be chosen, it would be necessary to couple it with an electrostatic one in order to minimize the power consumption and heating.

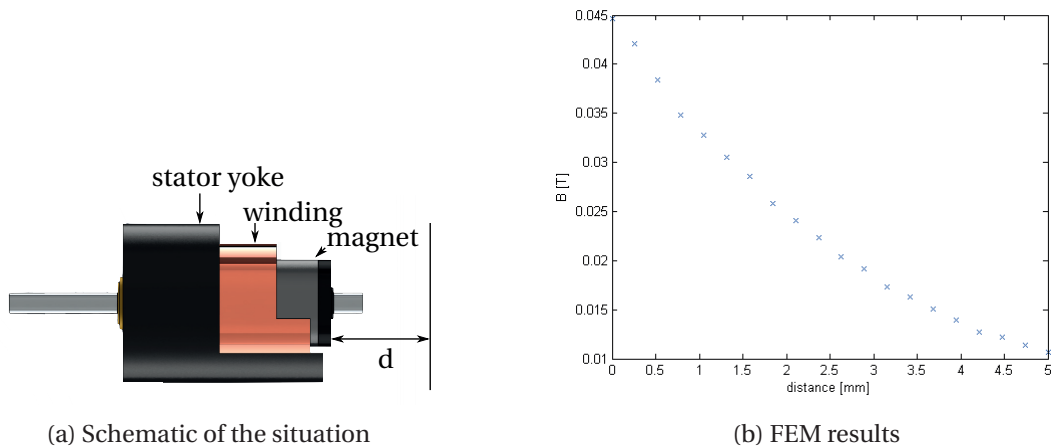


Figure 4.8 – Measurement of the induction under the magnet using FEM

Electrostatic actuation is a good candidate because of its low power consumption, fast response time and low contact resistance even if it needs a smaller air gap than the electromagnetic solution. Consequently this actuation scheme is the one that has been considered throughout this research.

4.1.2 Existing geometry in electrostatic MEMs

In the literature, different actuation strategies exist for electrostatic relays. They can be separated into three different categories:

- The relay can be composed of two terminals only i.e. a source and a drain. The actuation scheme of this relay follows the principle that when a difference of electrical potential is applied between the two terminals, the electrostatic force is generated and the terminals are closed. The current can flow between them. However, there is no control for the opening or closing. This relay works only under the reaction of the applied voltage. The main issue with this system is that when the contact is made, the source potential and the drain potential are at about the same potential. Contacts can easily break and therefore reliability is a major issue for this type of relays. Furthermore control of the relay is mandatory in order to avoid short circuit problems. For this reason, this solution does not fit the requirements.

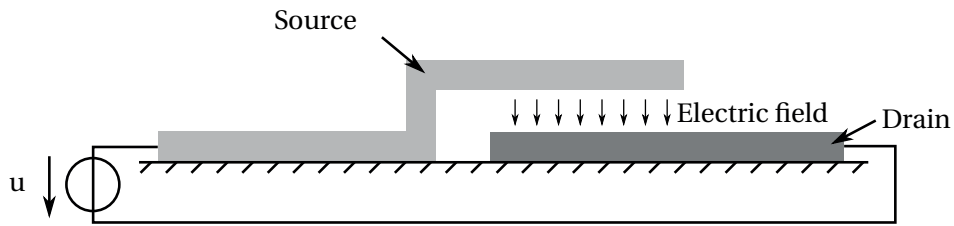


Figure 4.9 – Two terminal relay

- In order to actively control the behavior of the relay, a third terminal is added: the gate [103]. Here, the current flows between the source and the drain but the opening and closing are controlled by a difference of potential applied between the gate and the source. The main advantage of partially separating the command from the signal is the possible improvement of the contact. By optimizing the actuation part, a greater contact force can be produced and by extension a reduction of the contract resistance can be obtained. However, as the command and the signal are not completely isolated, due to the presence of floating voltages this relay can not be placed in series. This is the same problem as discussed in section 2.2.2.

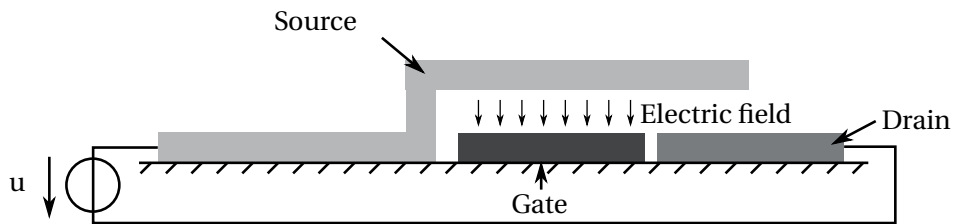


Figure 4.10 – Three terminal relay

- The floating voltage problem discussed above can be solved by completely isolating the command from the signal [50]. Here, the contact can be optimized as well. As a consequence, this topology is adequate and has been chosen.

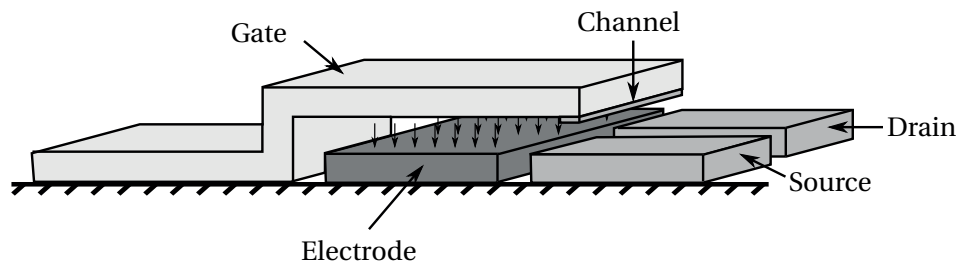


Figure 4.11 – Four terminal relay

4.2 Design

Now that the MEMS technology and that the geometry have been decided, the design of the relay is undertaken. The relay behavior is defined by its mechanical dimensions. This includes the stiffness of the structure, the switching time and its actuation voltage. Furthermore, if the manufacturing method is not considered, the relay design will not be feasible or dimensions will not be correct resulting in a modification of the expected dynamic of the relay. The design routine is presented in fig. 4.12 or can be described in the following steps:

- The mechanical design is undertaken. This part includes the calculation of the contact resistance, which is going to be determinant in the electrical circuit heating. As explained in [78], a flat contact is needed to minimize the contact resistance and ensure a good contact. For this reason, the design of the contact part is crucial. Then, the actuation part is designed conjointly with the anchor in order to be able to actuate the relay at the right voltage.
- From the mechanical design of the relay, its switching time is verified. It needs to be smaller than a phase commutation otherwise short circuits or torque losses would be noticeable. This will be discussed in more detail in section 6.3.
- Depending on the spacing between the electrodes, an electrical breakdown can occur and can lead to the relay malfunctioning or its destruction. In order to prevent this situation, a dielectric layer can be added to increase the insulation resistance, which will be discussed in section 4.2.3.
- As the relays will be manufactured through microfabrication techniques and because they suffer from limitation and tolerance, their feasibility is checked. In order to ensure the correct relay behavior, the manufactured dimensions have to be as close as possible to the designed ones. For example, due to the mask selectivity or due to the isotropy or anisotropy of the etching techniques used, the dimension of the etched pattern can be influenced. Moreover, this issue is magnified by the resolution of the UV lithography process. Then, as different metals will be used to manufacture the relay, chamber contamination can occur, which will prevent from the use of certain methods such as gas etching. All these problems have to be accounted for at the design stage.
- In order to integrate the relay inside of the motor, the motor is subject to internal resonance frequencies, which are due to the components of the motor. It is therefore necessary to verify that the resonant frequencies of the relay are above the ones of the motor and that they will not influence each other.

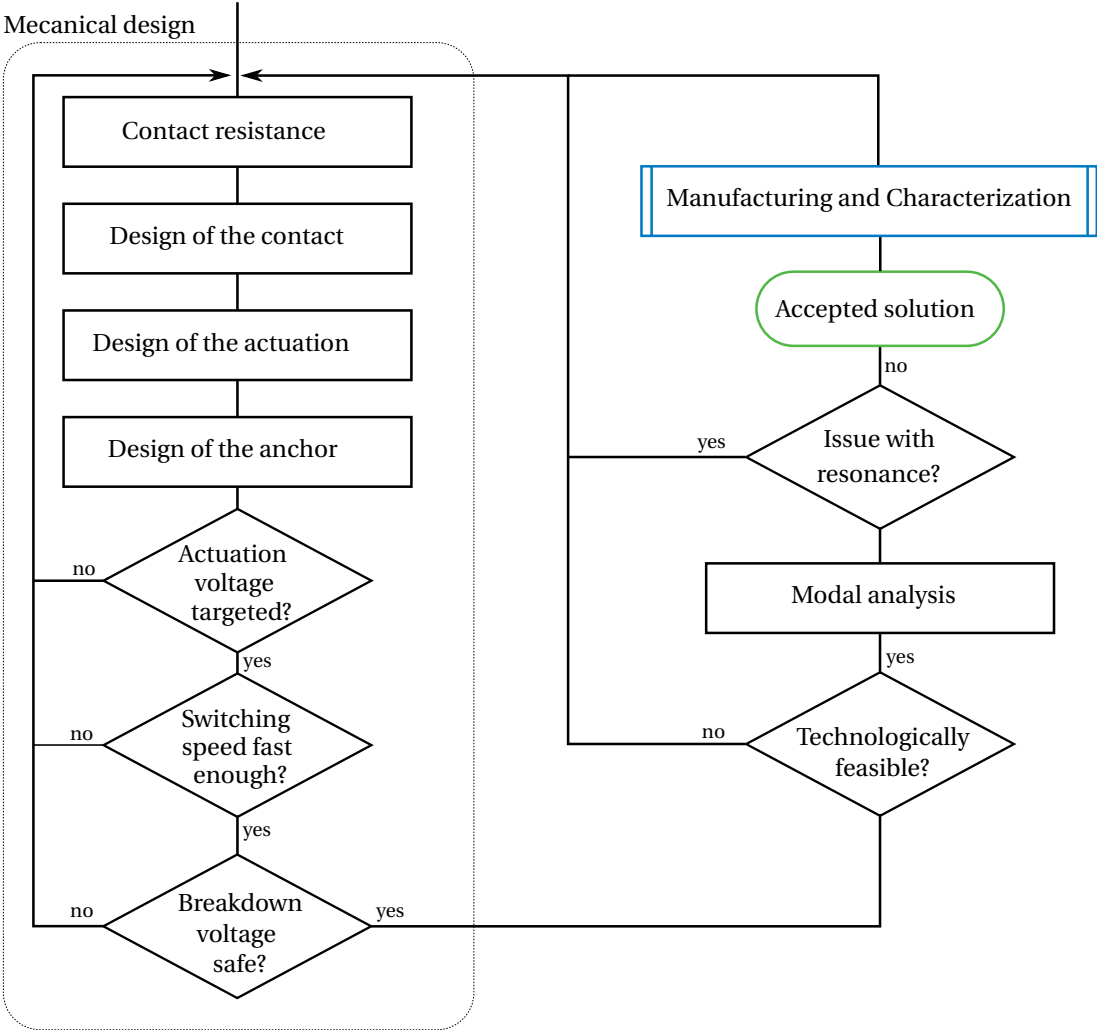


Figure 4.12 – Design routine

4.2.1 Resistance of the relay

Different resistances can be found in a relay:

$$R_{on} = R_{source} + R_{drain} + R_{channel} + 2 \cdot R_{contact} \tag{4.7}$$

Source, drain and channel resistances are bulk resistances calculated using :

$$R = \frac{\rho l}{S} \tag{4.8}$$

with ρ the resistivity, l the length of the track and S the cross section of the track.

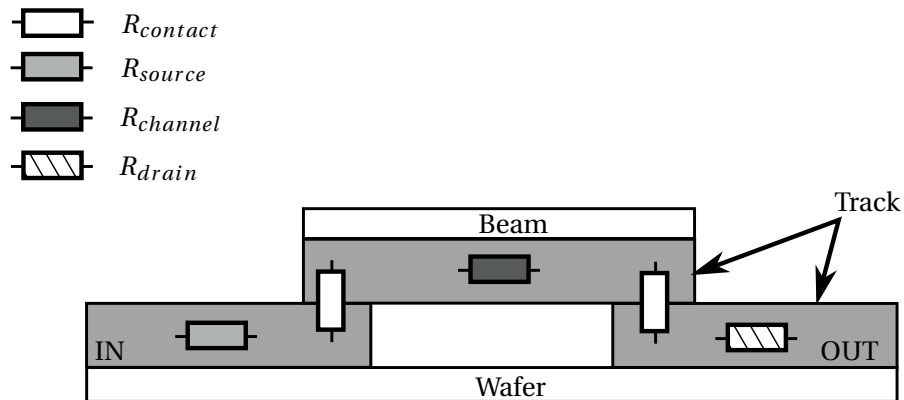


Figure 4.13 – Resistance of the relay in on state

Contact resistance

The main problem with the design of an ohmic relay is that the resistance is going to produce Joule losses. When the relay is turned on, the main resistance of the relay is the contact resistance, which is largely limited to the contact resistance at the contact dimple.

The contact resistance depends on three majors parameters, which are the contact force, the contact area and the hardness. The contact force is a function of the electrostatic actuator voltage. When a voltage is applied between two parallel plates, an electrostatic force is produced and the two plates attract each other. The contact area is the most complicated parameter to find. Because of the material roughness, the real contact surface is much smaller than the apparent contact surface. Fig. 4.14 shows real contact areas called a-Spot[41] in the apparent contact area.

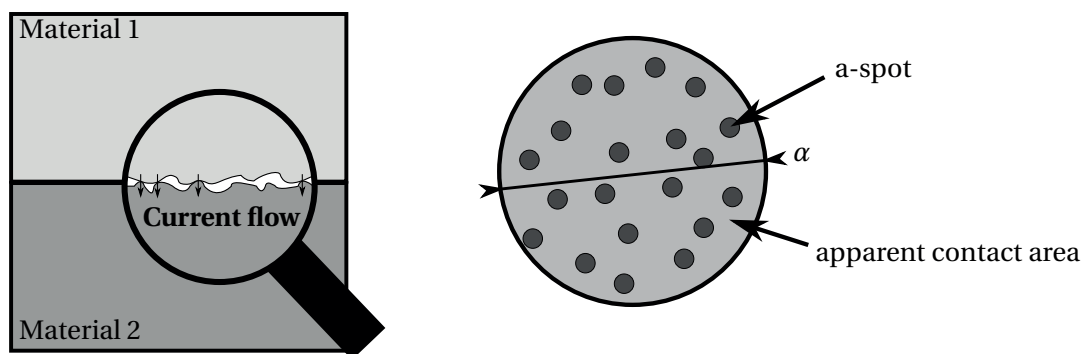


Figure 4.14 – Contact surface

In order to evaluate the contact resistance, two aspects have to be taken into account: the deformation of the contact and the transport of the electrons.

Chapter 4. Design of the MEMS relay

The deformation of the contact depends on the force applied on them. The deformation can either be elastic, plastic or elastic-plastic depending on the force applied on the contact. Usually, plastic deformation is considered because in order to achieve a low and stable contact resistance, the contact force applied to the contact spot is higher than $200 \mu\text{N}$ [52]. As a result, the effective contact radius a is expressed as:

$$a = \sqrt{\frac{F_c}{H\pi}} \quad (4.9)$$

with F_c the contact force and H the hardness of the softest of both materials. In the literature, this value is 1 GPa for electroplating deposition and 3 GPa for sputtering deposition because the full plastic deformation is influenced by the hardness of the substrate [80]

Holm's contact resistance formulation are based on several hypothesis:

- the a-spot have zero thickness,
- the contamination between the contacts are ignored,
- the contact member are bulk conductors.

There are three types of electron transport mechanisms that take place in MEMS switches that depends on the radius of the contact compared to the electron mean free-path:

- Ballistic if the radius of the contact is smaller than the electron mean free-path [106]
- Diffusive and ballistic if the contact is comparable to the electron mean free-path [42]
- Diffusive if the radius of the contact is bigger than the electron mean free-path [41]

In a thin gold layer, the electron mean free path has been calculated and a value of 11 nm has been found [18]. A contact radius of 561.4 nm is found using Holm's formula[41]. As the contact radius is bigger than the electron mean free path, Maxwell's formula can be used to find the contact resistance.

$$R_c = \frac{\rho_1 + \rho_2}{4a} \quad (4.10)$$

where a depends on the type of deformation of the contacts and ρ_1 and ρ_2 are respective resistivities of the different contact materials.

The contact resistance for different materials is reported in fig. 4.15.

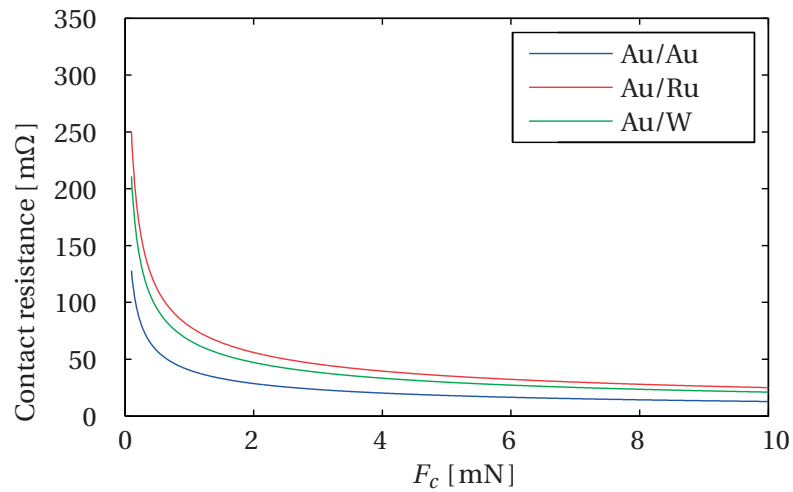


Figure 4.15 – Contact resistance for different material

As shown in figure fig. 4.15, the contact force should be at least higher than 2 mN in order to get a low and stable contact resistance. Furthermore, fig. 4.15 also shows for 5 mN that tungsten or ruthenium combined with gold gives similar contact resistances (35.4 mΩ for Au-Ru contact or 29.8 mΩ for Au-W). The value found is higher than what would be obtained by using only gold contacts. However, combined metals give a better stability over time and less stiction problems.

The contact structure

Section 4.2.1 reveals that the contact resistance depends on the contact force, the hardness of the material and the contact surface. Based on Holm's work and assumptions, Greenwood has developed a more realistic model of the contact resistance based on a statistically modelling that consider clusters of contact spots instead of a single a-spot between two flat surfaces. Consequently, the contact resistance equation becomes [34]:

$$R_c = \rho \left(\frac{1}{2na} + \frac{1}{2\alpha} \right) \quad (4.11)$$

where a is the effective contact radius, α is the radius of the cluster of contact spots and n the number of contacts

As the radius of the contact spot cluster increases, the overall contact resistance decreases. This is implied in [78] when it said that the flatness of the contact improves its quality. Furthermore, in order to have a high current flowing through the track, it is preferred to have more contact points because less current will flows in each contact. This reduces the risk of burning a single

Chapter 4. Design of the MEMS relay

contact point. For this reason, the flatness of the contact needs to be guaranteed.

Not knowing the dispersion of the contact spots, as both Holm model and Greenwood model give similar results, Holm formulation is preferred for a first design.

When contacts are closing, the contact occurs between the two parallel plate at first. Then, as the electrostatic force keeps pulling the contact down and increases the contact force, the contact will start bending as shown in fig. 4.16. The contact surface will be drastically reduced

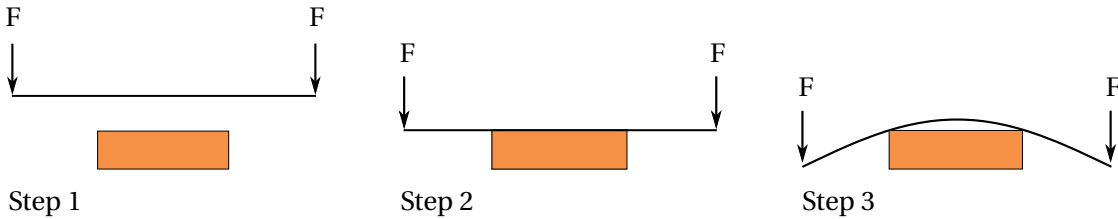


Figure 4.16 – Bending of the contact while the contacts are closing

However, it possible to reduce this bending moment and improve the contact by modifying the stiffness of the contact.

The contact part can be subdivided into two parts:

- the contact itself,
- the anchor between the contact and the electrode.

The overall system can be modelled as shown in fig. 4.17 when the contact is closed. The electrodes are considered as rigid bodies. F_a and F_b are the reacting force of the contact, F is the generated force by the electrodes, F_m is the gravity force applied on the contact due to the volume added above it in order to stiffen the structure. E is the Young's modulus and I is the inertia.

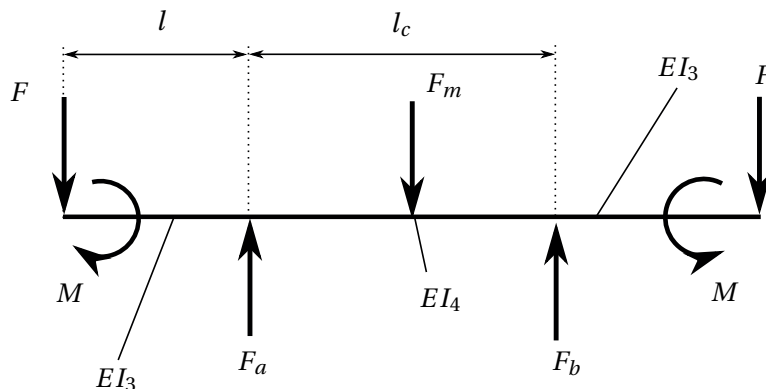


Figure 4.17 – Schematic of the contact part

In order to reduce the bending moment, the influence of the geometrical dimensions and

properties is studied using the following parameters: α is the ratio between the length of the contact (l_c) and the length of the link part between the contact and the electrode (l) and β is the ratio between the equivalent flexural rigidity of the center of the beam and the equivalent flexural rigidity of the named link. Note that the inertia depends on the geometry used. α is used in order to minimize the size of the relay. Moreover, when β increases, the rigidity of the contact part increases and it bends less. The following development shows how α and β are linked together with the contact structure and the curvature of the contact produced.

$$\alpha = \frac{l}{l_c} \quad (4.12)$$

$$\beta = \frac{EI_4}{EI_3} \quad (4.13)$$

The contact curvature is parametrized using the representation shown in fig. 4.18:

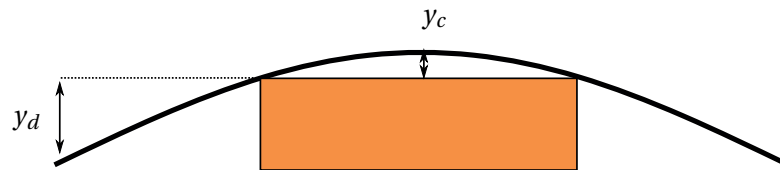


Figure 4.18 – Parametrization of the bending moment

- A maximum curvature allowed at the center of the contact (y_c) depends on the roughness of the material. For example gold sputtering gives a peak to peak height of 5 nm [101].
- The final deflection (y_d) of the electrode when the power pads are in contact

y_d and α have to be chosen considering the geometric limitation and the breaking stress of the link. β can be found by solving the following system as shown in fig. 4.18. Note that the bigger is y_d and the smaller α , the more stress is applied to the link.

By solving the mechanical part presented in fig. 4.17, using the boundary conditions shown in eq. (4.14)

$$\begin{cases} y1(0) & = y_d \\ y2(\alpha \cdot l + \frac{l}{2}) & = y_c \end{cases} \quad (4.14)$$

the following equations are found:

Chapter 4. Design of the MEMS relay

$0 < x < l$:

$$y_1(x) = \frac{(\alpha \cdot l - x)(16 \cdot \alpha^2 EI_4 \cdot F \cdot l^2 + 8 \cdot \alpha \cdot F \cdot l \cdot (3 \cdot EI_3 \cdot l - EI_4 \cdot x) - 3EI_3 \cdot F_m \cdot l^2 - 8 \cdot EI_4 \cdot F \cdot x^2)}{48 \cdot EI_3 \cdot EI_4} \quad (4.15)$$

$l < x < l + \frac{l_c}{2}$:

$$y_2(x) = \frac{(\alpha \cdot l - x)(4 \cdot \alpha^2 \cdot l^2 (6 \cdot F + F_m) + 8 \cdot \alpha \cdot l \cdot (3 \cdot F \cdot (l - x) - F_m \cdot x) + F_m \cdot (4 \cdot x^2 - 3 \cdot l^2))}{48 \cdot EI_4} \quad (4.16)$$

As a result, β is found:

$$\beta = \frac{-24 \cdot \alpha^2 \cdot F \cdot y_c - 6 \cdot \alpha \cdot F \cdot y_d + 3 \cdot \alpha F_m \cdot y_c + F_m \cdot y_d}{16 \cdot \alpha^3 \cdot F \cdot y_c} \quad (4.17)$$

Finally, the flexural rigidity can be found using β :

$$EI_3 = \frac{\alpha \cdot l^3 \cdot (16 \cdot \alpha^2 \cdot \beta \cdot F + 24 \cdot \alpha \cdot F - 3 \cdot F_m)}{48 \cdot \beta \cdot y_d} \quad (4.18)$$

$$EI_4 = \beta \cdot EI_3 \quad (4.19)$$

At this point, a trade-off between the process and the design has to be done because for instance, it is really complicated to manipulate a wafer thinner than 100-200 μm . Furthermore, it is also important to check that the elastic limit is not exceeded.

The total flexure rigidity of two materials (here gold and silicon) placed one above each other is found using eq. (4.20):

$$EI = E_{Au} \cdot f \cdot I_{Au} + E_{Si} \cdot (1 - f) \cdot I_{Si} \quad (4.20)$$

with:

$$f = \frac{V_{Au}}{V_{Au} + V_{Si}} \quad (4.21)$$

and

$$I_i = \frac{w_i \cdot t_i^3}{12} \quad (4.22)$$

with E_i , I_i and V_i as the Young's modulus, the inertia and the volume of the material i respectively.

In order to confront the analytical analysis previously presented, a finite element modelling is used as represented in fig. 4.3 with the dimensions given in table 4.2. This figure represents the cross section deflection for the contact part. Here, a relay with a pull-in voltage of 15 V is used. By applying a 20 V on the electrodes, a relative error of 9% is found between the two models.

Table 4.2 – Values used for the comparison between the two models

| Parameter | Value |
|-----------|-----------------------|
| α | 0.1 [-] |
| β | 7485 [-] |
| d_1 | 3 [μm] |
| d_2 | 200 [nm] |
| l_c | 500 [μm] |
| y_c | 1 [nm] |
| y_d | 200 [nm] |
| E_{Au} | 79 [GPa] |
| E_{Si} | 160 [GPa] |

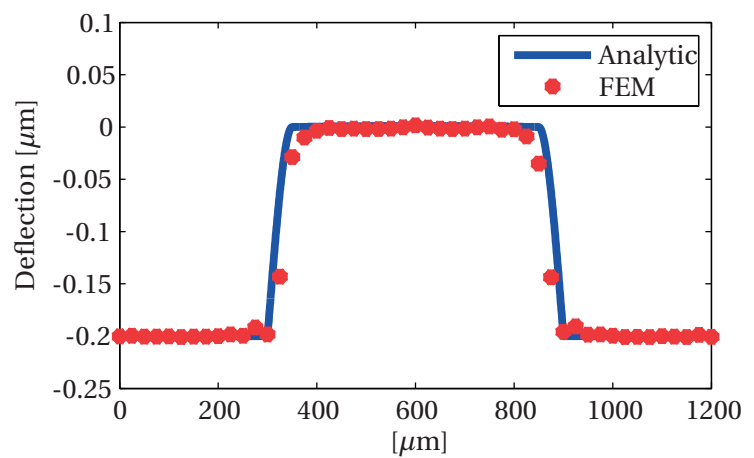


Table 4.3 – Contact deformation

4.2.2 Modelling using the Lagrange formulation

As the relay is a 3 dimensional structure composed of several degrees of freedom, the Lagrange operator can be used to determine the equation of motion. It is the difference between the total kinetic energy (T) and the total potential energy (U) of the system as expressed in eq. (4.23).

$$L = T - U \tag{4.23}$$

where T and U are time dependant.

The equation of motion using the Lagrange formulation:

$$\frac{d}{dt} \left(\frac{\partial L}{\partial \dot{q}_i} \right) - \frac{\partial L}{\partial q_i} = F_{nc}(q_i, \dot{q}_i) \tag{4.24}$$

Chapter 4. Design of the MEMS relay

where q_i is the generalized coordinate, t is the time and F_{nc} are the generalized non-conservative forces of the system.

In the relay case, different forces come into play. The elasticity of the material implies that the system behaves like a spring. Because of the compressive air between the materials a damping effect can be observed. Finally, the mass of the material contributes to an inertial effect on the system. The system is summarized in fig. 4.19.

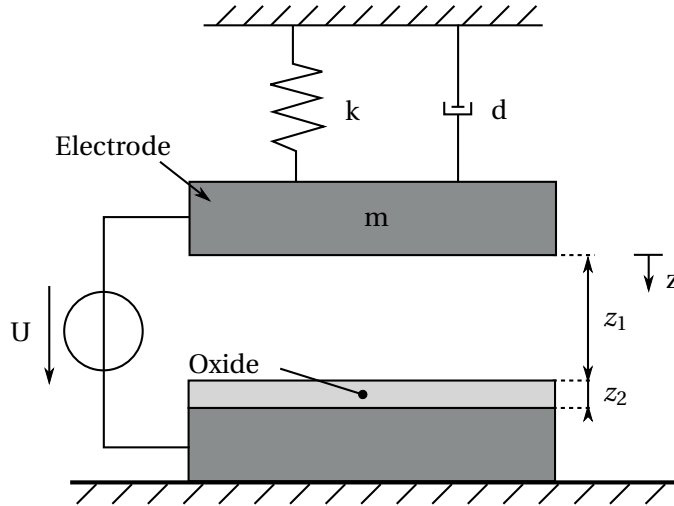


Figure 4.19 – Model of the relay

Non-conservative forces

A force is called non-conservative or dissipative when its work differs depending on the travel path. These forces include the friction force, the viscous force or the normal force. In the relay case, the structure is suspended, as a result the only non-conservative force present in the system is a viscous force named the damping force that will oppose to the relay closure. The damping force can be derived from the Rayleigh dissipation function with the relation

$$F_{\text{damp}} = -\nabla R_{\text{damp}} \quad (4.25)$$

where

$$R_{\text{damp}} = \frac{1}{2} \sum_{i=1}^n \sum_{j=1}^n D_{ij} \dot{q}_i \dot{q}_j \quad (4.26)$$

with D , the damping coefficient.

Conservative energy expression for a MEMS relay

Kinetic energy As the relay is a three dimensional structure that can move in different directions, the kinetic energy shall be expressed for all directions. There are three translations as well as the rotations around every axis.

$$T = T_{\text{lin}} + T_{\text{rot}} \quad (4.27)$$

- The kinetic energy due to linear displacement is calculated as follows:

$$T_{\text{lin}} = \frac{1}{2} \dot{X}^T M \dot{X} \quad (4.28)$$

where $\dot{X}^T = [\dot{x} \ \dot{y} \ \dot{z}]$ and M is the mass matrix.

- For rotational displacement, the kinetic energy is:

$$T_{\text{rot}} = \frac{1}{2} \dot{\Phi}^T J \dot{\Phi} \quad (4.29)$$

where $\dot{\Phi}^T = [\dot{\phi} \ \dot{\theta} \ \dot{\psi}]$ and J is the inertia matrix.

Potential energy As explained in section 4.2.2, due to the elasticity of the material, the suspended structure behaves like a spring, which stores a potential energy. It is expressed as:

$$U = \frac{1}{2} X^T K X \quad (4.30)$$

where $X^T = [x \ y \ z]$ and K is the spring matrix.

Eq. (4.30) expresses the Cartesian potential energy of the spring system. Rotational directions have a potential energy as well. For example, using the representation of fig. 4.20 and the small angle approximation, the potential energy is given by eq. (4.31).

$$U = \frac{1}{2} k_z (L_x \cdot \theta)^2 \quad (4.31)$$

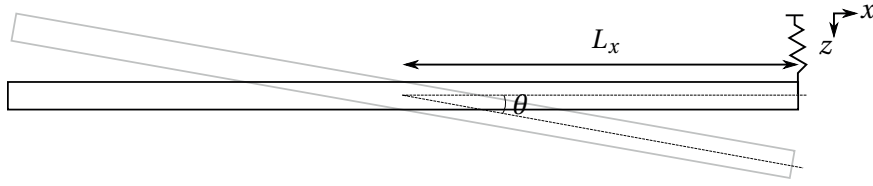


Figure 4.20 – Rotational stiffness

External force

The external applied force is the electrostatic force given by eq. (4.5). By considering the oxide between the electrode and the illustration of fig. 4.19, the energy for the air gap and the oxide are:

$$\begin{cases} W_{e_1} = \frac{1}{2} \cdot C_1 \cdot U_1^2 \\ W_{e_2} = \frac{1}{2} \cdot C_2 \cdot U_2^2 \end{cases} \quad (4.32)$$

with:

$$\begin{cases} U_1 = U \cdot \frac{C_2}{C_1 + C_2} \\ U_2 = U \cdot \frac{C_1}{C_1 + C_2} \end{cases} \quad (4.33)$$

The electrostatic force is:

$$F_{\text{elec}} = \frac{\epsilon_0 \cdot A \cdot U^2}{2} \cdot \frac{\epsilon_{r_1} \epsilon_{r_2} \cdot (\epsilon_{r_1} + \epsilon_{r_2})}{(\epsilon_{r_1} z_2 + \epsilon_{r_2} (z_1 - z))^2} \quad (4.34)$$

where ϵ_0 is the vacuum permittivity, ϵ_{r_i} is the relative permittivity of each domain i , A is the surface of the electrode and U is the applied voltage on the electrodes.

The pull-in voltage

When an electrostatic force is applied between two electrodes, the latter two are attracted to each other, and by the time the electrostatic force surpasses the spring force of the relay, instability is reached and the switch instantly closes. The point where these named forces are equal to each other is called pull-in:

$$F_{\text{elec}} = F_k \quad (4.35)$$

For a given displacement, the pull-in position when the electrostatic force overcomes the spring force occurs when:

$$z_{\text{pull-in}} = \frac{\epsilon_{r_2} \cdot z_1 + \epsilon_{r_1} \cdot z_2}{3 \cdot \epsilon_{r_2}} \quad (4.36)$$

Consequently, the pull-in voltage is:

$$U_{\text{pull-in}} = \sqrt{\frac{8 \cdot k \cdot (\epsilon_{r_1} \cdot d_2 + \epsilon_{r_2} \cdot d_1)^3}{27 \cdot \epsilon_0 \cdot \epsilon_{r_1} \cdot \epsilon_{r_2}^2 \cdot (\epsilon_{r_1} + \epsilon_{r_2}) \cdot A}} \quad (4.37)$$

In order to validate the analytical model, the latter is compared to a finite element model as shown in fig. 4.21, which is reported in fig. 4.22. An error of 2% is found between these two models. However, by considering the deflection of the relay before the pull-in, a maximum error of 13.95% is found for the deflection.

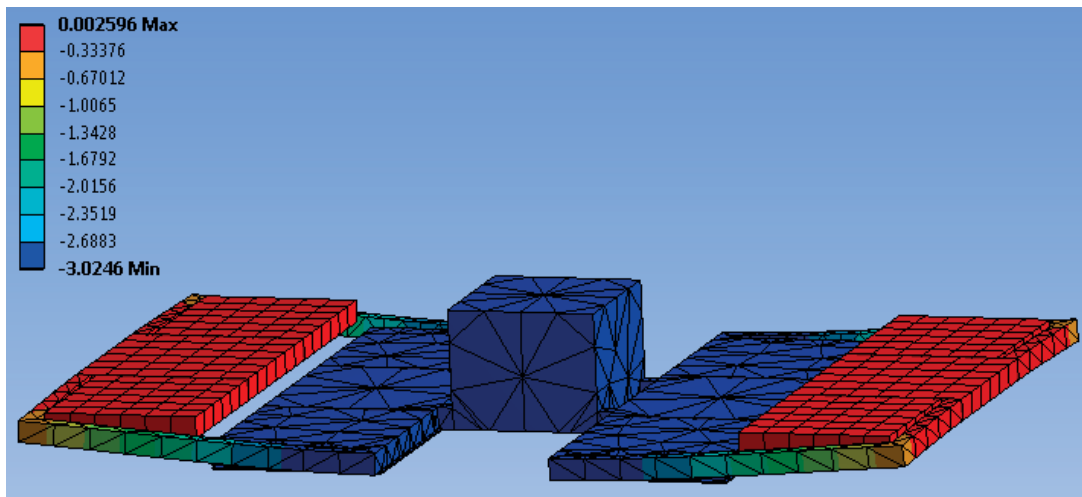


Figure 4.21 – Deflection calculated under 15 V actuation using FEM performed with ANSY

Stiffness

As shown in section 4.2.2, stiffness is present in the 6 degrees of freedom. As the focus is in the actuation direction, the stiffness coming from the vertical displacement is developed here.

Different anchor geometries are possible. The crab-leg one is chosen because of its possible compactness and because its stiffness is smaller for the vertical displacement than the planar one. This means that the vertical displacement will be preferred. The vertical deflection is composed of two mechanisms. Firstly there is the vertical displacement itself and then there is a torsion that appears as the arm goes down as shown in fig. 4.23.

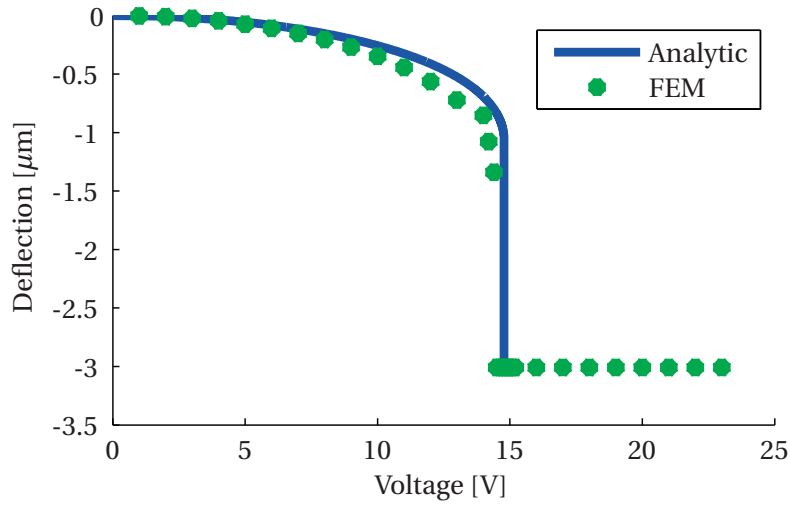


Figure 4.22 – Pull-in simulation

$$\begin{cases} M_1 = M_0 - F_z \xi \\ T_1 = T_0 \\ M_2 = T_1 - F_z \xi \\ T_2 = M_0 - F_z L_1 \\ M_3 = T_2 - F_z \xi \\ T_3 = T_1 - F_z L_2 \end{cases} \quad (4.38)$$

By using the Castigliano theorem for small deformations:

$$\delta_i = \frac{\partial U}{\partial F_i} \quad (4.39)$$

where δ_i is the displacement (linear or rotational) due to the applied constraint F_i .

Consequently, the total displacement is [22]:

$$\delta_i(F_i) = \sum_{i=1}^3 \int_0^{L_i} \left(\frac{M_i}{EI_i} \frac{\partial M_i}{\partial F_i} + \frac{T_i}{GJ_i} \frac{\partial T_i}{\partial F_i} \right) d\xi \quad (4.40)$$

where E is the Young's modulus, J is the torsion constant and G is the torsion modulus given

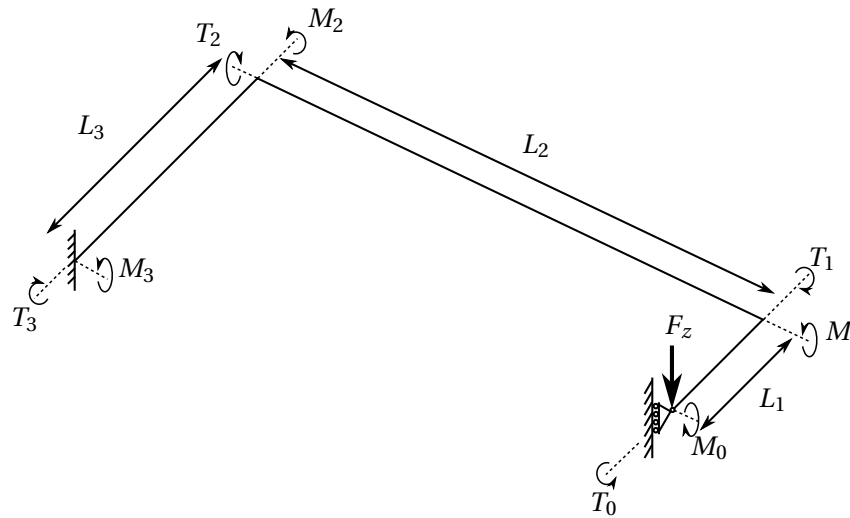


Figure 4.23 – Body diagram of a relay arm

by [22]

$$G = \frac{E}{2(1 + \nu)} \quad (4.41)$$

The system presented in eq. (4.38) is solved using the boundary condition for a guided-end where:

$$\begin{cases} \delta_i(M_0) = 0 \\ \delta_i(T_0) = 0 \end{cases} \quad (4.42)$$

Finally, the stiffness for the vertical displacement is:

$$k_z = \frac{A}{B + C + D} \quad (4.43)$$

$$A = 48EGI_1I_2I_3(EI_1I_3L_b + GJ_2(I_3L_a + I_1L_c))(GI_3J_1L_b + EI_2(I_3L_a + J_1L_c)) \quad (4.44)$$

$$\begin{aligned} B = & 12E^3I_1^2I_2^2I_3^2L_aL_b^3L_c + G^3I_3J_1J_2L_b(I_1I_3L_b^3(I_3L_a + I_1L_c) \\ & + I_2(I_3^2L_a^4 + I_1^2L_c^4 + 2I_1I_3L_aL_c(2L_a^2 + 3L_aL_c + 2L_c^2))) \end{aligned} \quad (4.45)$$

$$C = 4E^2 G I_1 I_2 I_3 L_b (I_1 I_3 L_b^3 (I_3 L_a + J_1 L_c) + I_2 (I_3^2 L_a^4 + I_3 L_a L_c (J_1 L_a^2 + 3J_2 L_a L_b + I_1 L_c^2) + I_1 L_c^2 (3J_2 L_a L_b + J_1 L_c^2))) \quad (4.46)$$

$$D = EG^2 (I_1^2 I_3^3 J_1 L_b^5 + I_2^2 J_2 (I_3 L_a + J_1 L_c) (I_3^2 L_a^4 + I_1^2 L_c^4 + 2I_1 I_3 L_a L_c (2L_a^2 + 3L_a L_c + 2L_c^2))) \quad (4.47)$$

$$+ 4I_1 I_2 I_3 L_b^2 (I_3^2 L_a^2 (J_1 L_a + J_2 L_b) + I_1 J_1 J_2 L_b L_c^2 + I_3 L_c (I_1 J_2 L_a L_b + J_1 J_2 L_a L_b + I_1 J_1 L_c^2)) \quad (4.48)$$

4.2.3 Breakdown voltage

When the voltage increases, there is a limit where the insulator becomes electrically conductive, which is called the breakdown voltage. For the relay design, the electric field passes in two different environments between the two electrodes. There is air and silicon oxide between the electrodes which are both insulators. The role of the oxide is to avoid a contact between the two electrodes and to protect the actuation from breakdown voltage when the relay is closed. Supposing that the resistivity is a constant for each environment, the space between the two electrodes can be modelled as two resistances placed in series, which helps to determine the applied voltage for each domain. When the relay is opened, the influence of the oxide is negligible. Note that, in order to avoid breakdown voltage the relay can be encapsulated and be placed in the void as vacuum discharges are a rare event.

Two scenarios are considered:

- When the relay is open (the electrodes are separated), the critical breakdown voltage is the air. The breakdown voltage for the air gap is evaluated with the modified Paschen curve. As the normal Paschen curve does not consider the field emission, its equation is [32]:

$$\gamma_i + K \cdot e^{-\frac{D_{FN} \cdot d}{U_b}} \left(e^{A \cdot p \cdot d \cdot e^{-\frac{B \cdot p \cdot d}{U_b}}} - 1 \right) = 1 \quad (4.49)$$

where γ_i is Townsend's second ionization coefficient, A and B are gas composition constant, K a constant d is the air gap, p is the pressure and:

$$D_{FN} = (6.85 \cdot 10^7) \frac{\phi^{\frac{3}{2}}}{\beta} \quad (4.50)$$

where D_{FN} is the threshold electric field required for field emission, ϕ is the work

function of the cathode and β is the geometric enhancement factor.

The breakdown voltage for the air at 1 atm is given in fig. 4.24

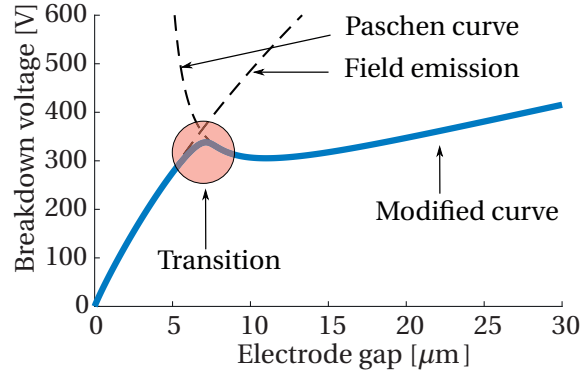


Figure 4.24 – Modified Paschen curve using [32]

The modified Paschen curve is divided into three zones: avalanche for high gaps, transition and field emission for small gaps. The safe zone for the design of the relay is below this curve.

- When the relay is closed, the critical breakdown voltage is at the dielectric. Here the breakdown is calculated using the dielectric strength. Different publications evaluate it from 9.5 [47] to higher than 10 MV/cm. For 200 nm, the measured SiO₂ breakdown voltage is 85-90 V.

As the relay closes, partial gas discharges in the air can occur as explained in [107] but should not damage the dielectric or electrodes.

4.2.4 Dynamic response analysis

When a difference of voltage is applied to the electrodes, the relay closes when the electrostatic force overcomes the resisting spring force. In order to reduce the size of the electric track that supplies the electrode, the current pulse that will be generated during the actuation of the relay needs to be known so that the electric track does not react as a fuse. The mechanical and electrical domains are put in relation in the system presented in eq. (4.51).

$$\begin{cases} C = \frac{\epsilon_0 \cdot A}{d - z - z_2 \cdot (1 - \frac{1}{\epsilon_{r2}})} \\ F_z = \frac{1}{2} \epsilon_0 \cdot U^2 \frac{\epsilon_{r2} \cdot (1 + \epsilon_{r2})}{(z_2 + \epsilon_{r2} \cdot (d - z))^2} \\ \ddot{z} = \frac{F_z}{m} - \frac{B}{m} \cdot \dot{z} - \frac{k}{m} z \\ \dot{u}_c = \frac{U}{RC} - \left(R \frac{dC}{dz} \dot{z} + 1 \right) \frac{u_c}{RC} \end{cases} \quad (4.51)$$

where z is the displacement, F_z is the electrostatic force in the z direction, z_2 is the oxide

Chapter 4. Design of the MEMS relay

thickness, ϵ_r is the permittivity of the oxide, B is the damping ratio, k is the spring constant, R is the series resistance, C is the capacitance of the relay and u_c is the voltage at the capacitor terminal.

In the following development, the values presented in table 4.4 are used. These parameters are based on the representation shown in fig. 4.19. The data presented in fig. 4.25, fig. 4.26 and fig. 4.27 are shown until the first contact is made. Here, the rebounces of the contact are not considered.

Table 4.4 – Value used for the dynamic response analysis

| Parameter | Value | Unit |
|-----------|------------------------|--------------------------------|
| z_1 | 3.2 | μm |
| z_2 | 220 | nm |
| A | $1.9914 \cdot 10^{-6}$ | m^2 |
| B | 0.01 | - |
| k | 2500 | $\text{N} \cdot \text{m}^{-1}$ |
| R | 6.3 | Ω |
| m | $1 \cdot 10^{-6}$ | kg |
| U | 20 | V |

They are two aspects to analyse during the transient closing relay: as soon as the relay is turned on and when the relay structure is closing.

As soon as the relay is supplied, a current peak can be noticed because the capacitor is discharged. As the value of the capacitance is small, this peak is brief but its amplitude is high ($\frac{U}{R}$) as shown in fig. 4.25.

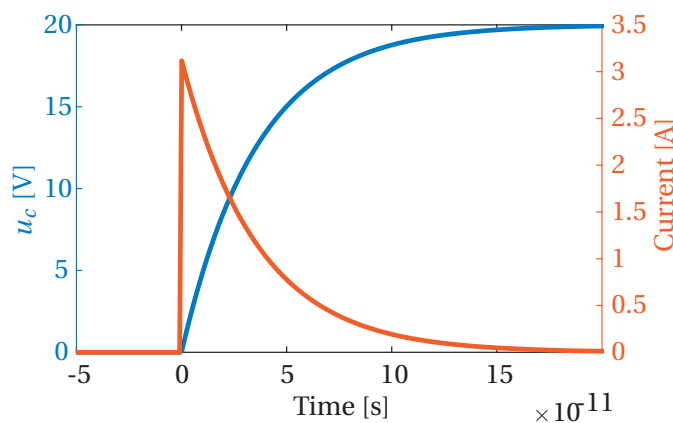


Figure 4.25 – Current peak when the relay is turned on

When the relay is closing, the capacitance of the relay will increase because the air gap decreases as the electrodes are brought together. As a result this variation of the capacitance

induces a current in the track as expressed in eq. (4.52).

$$\frac{dQ}{dt} = \frac{d(C \cdot U)}{dt} \quad (4.52)$$

where Q is the electric charge, C is the capacitance, which is a function of the air gap between the electrodes, and U is the applied voltage to the electrodes.

This second peak is smaller than the previous one as shown in fig. 4.26. If the relay closes more rapidly, the capacitance will increase faster as well. Consequently, the current peak will be higher.

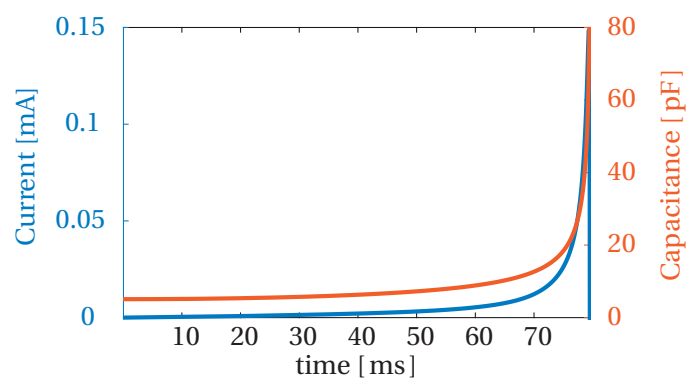


Figure 4.26 – Current increase with the variation of the capacitance

Finally, by increasing the applied voltage, the electrostatic force increases as well. If the applied voltage is bigger than the pull-in voltage, the relay will close faster as shown in fig. 4.27. However, it will be more subject to bounce.

Consequently, the relay should behave normally if the electrodes tracks are able to hold the first current peak or if a resistance high enough is added in series to limit this current. However, this higher resistance will be at the expense of the actuation time.

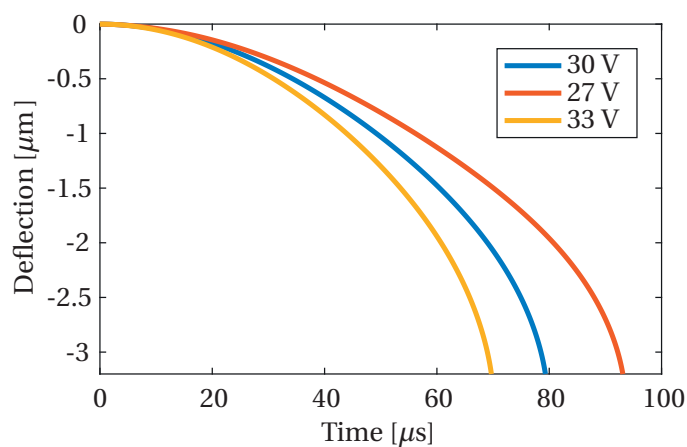


Figure 4.27 – Variation of the switching time depending on the voltage applied

4.2.5 Modal analysis

When it comes to integrate a system inside another, the environment needs to be analyzed. As the motor is placed in rotation, the system will be subject to vibrations. If the natural frequency of the relays coincides with a natural frequency of the motor, they can influence each other and lead to degradation or dysfunction -e.g. unwanted actuation or self-destruction- of the relay. Due to the numerous components of the motor, different natural frequencies can be measured.

These frequencies can be measured through random vibrations and shocks. For example, by using three accelerometers with the motor presented in section 3.2, its natural frequencies in the XYZ axis are reported in fig. 4.28.

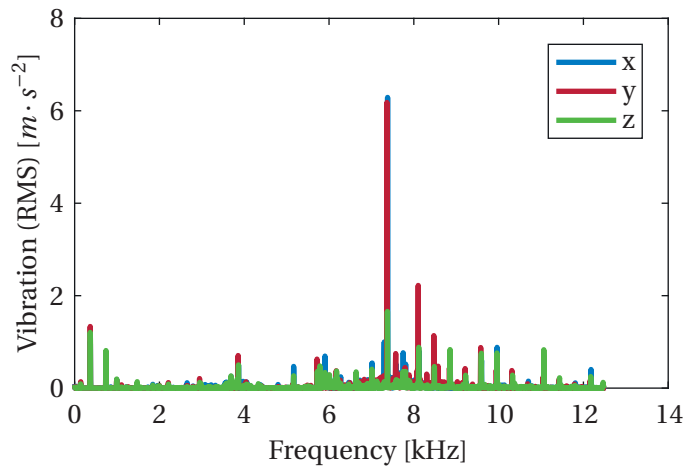


Figure 4.28 – Measures of the motor vibration (motor presented in section 3.2) in the XYZ directions

In order to safely design the relay, its resonant frequencies should be above all the resonant frequencies of the motor for its operating range. As a result, when the motor accelerates, the relay resonant frequencies will never be reached. Moreover, its resonant frequencies or its harmonics will not coincide with the ones of the motor.

Here, only the natural frequencies in the XYZ direction are presented. However, the full study shall contain the measurement performed with the rotational modes by adding a gyroscope or other sensors to analyze them. With the same presented method, the safe natural frequency interval can be deduced.

4.3 Design example

The dimension of the designed relay is show in fig. 4.29. In this figure the anchors are highlight in red, the electrodes are in green and the contact part is yellow. Furthermore, the main physical properties of the relay are given in table 4.5. The first three natural frequencies

calculated by FEM are given. The lower one does not coincide with the motor ones.

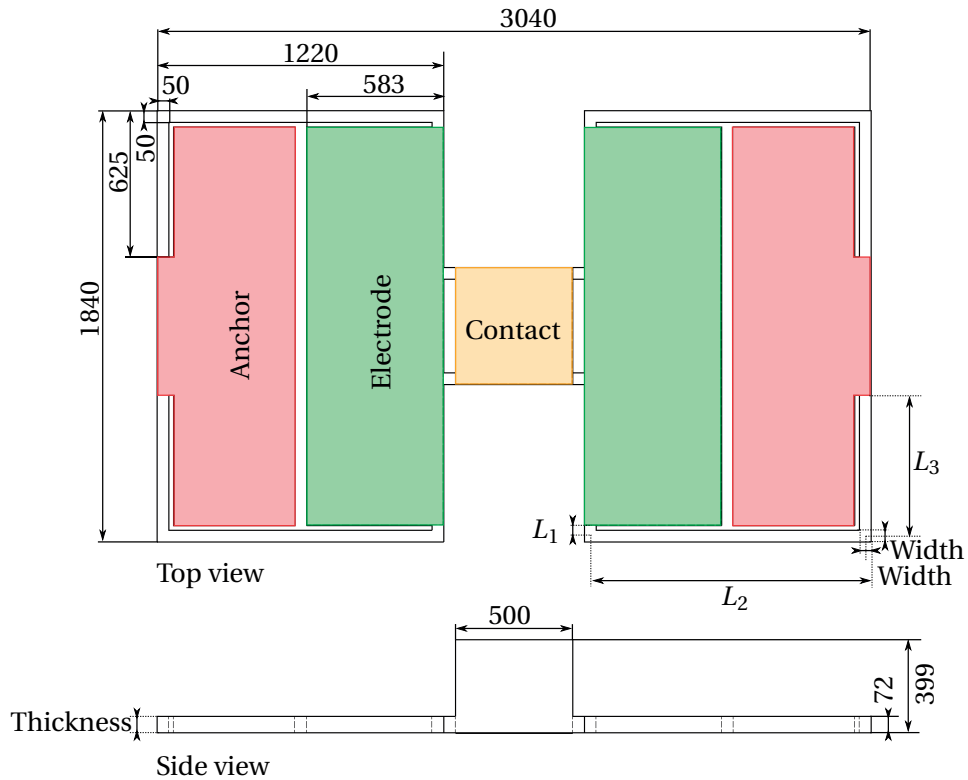


Figure 4.29 – Dimension of the designed relay - dimension in μm

Table 4.5 – Design relay properties

| Parameter | Value | Unit |
|--------------------------|-------|------------------------------|
| Conducting resistance | 168 | $\text{m}\Omega$ |
| Stiffness | 2515 | $\text{N}\cdot\text{m}^{-1}$ |
| Pull-in voltage | 30 | V |
| Switching time | 67 | μs |
| First natural frequency | 9.6 | kHz |
| Second natural frequency | 10.2 | kHz |
| Third natural frequency | 23.7 | kHz |

4.3.1 Influence of the microfabrication tolerances

Depending on the manufacturing method, the machines used suffer from their tolerances. The main aspect that will influence the relay physical behavior is the etching steps.

- During a thinning process, due to the machine tolerance, the obtained thickness may diverge from the targeted one.
- When it comes to etching techniques -i.e. wet or dry-, the etch can be controlled

approximatively by knowing the etching rate. However, these techniques can produce dimension errors if they are not well controlled. Here are different examples that can appear:

Depending on the selectivity of the used mask, the latter can be partially etched and can increase the etching pattern.

The isotropy or anisotropy of the etching can also be an important factor. If the etched material is anisotropic, vertical side walls are created. However, if the material is isotropic, round side walls are produced as shown in fig. 4.30. Additionally, using wet etching with silicon wafers, slopes can be created due to the difference in their etching rates caused by the crystal orientations.

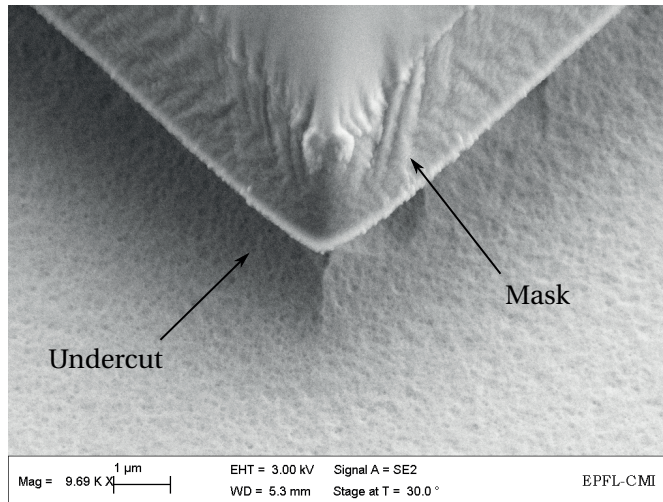


Figure 4.30 – Round under cut

By accounting for the tolerances and considerations that arise from the manufacturing process, it becomes possible to design the relay with the appropriate dimensions. The used geometric parameters are given in fig. 4.29.

One of the main characteristics that defines the relay behavior is the stiffness. If the latter is too high the structure is too rigid and a higher actuation voltage is necessary. An example of the influence of the width (due to an over etch) or the thickness of the wafer -e.g due to grinding or polishing- are compared in fig. 4.31. Furthermore, the Young's modulus is also compared because of its variability with the crystal orientation.

Fig. 4.31 reveals that the main critical parameter is the thickness. For example, a +10% for the latter implies an increase of 32% for the stiffness. The same error for the width implies a variation of 10% for the stiffness. A variation on the Young's modulus has the same influence as a variation of the width.

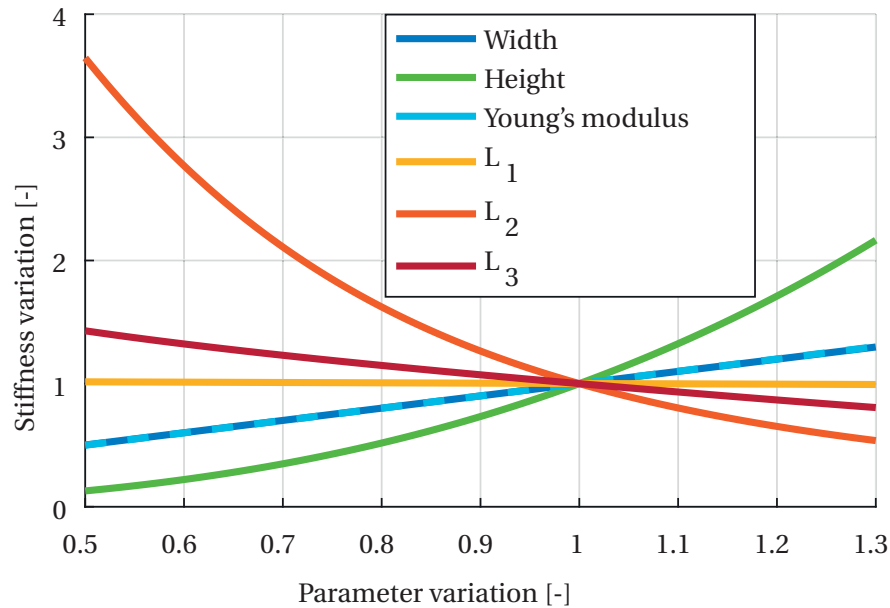


Figure 4.31 – Influence of different parameters variations on the relay stiffness (Normalized value)

4.4 Summary and conclusion

This chapter presents a methodology to design a relay with the aim to integrate it inside the motor. This methodology has been used to design this project's relay. As there are different types of MEMS relay technologies, its choice has required a detailed analysis because of the environmental condition into which the relays will be placed. Consequently, the electrostatic solution has been chosen for its simplicity of fabrication, its low actuation consumption, its low switching time and its force to allow a sufficient low contact resistance.

When the contact is made, the applied force exerted by the pull-in electrode can bend the contact structure resulting in a decrease of the contact surface. In order to achieve a sufficiently low contact resistance, the contact surface is decisive. A mechanical approach based on a variation of the flexural rigidity of the structure is proposed, which significantly improves the flatness of the contact.

Then the mechanical design takes place. Consequently, different aspects are taken care of. Because the designed relay is electrostatic, it can be subject to breakdown voltages. The natural frequencies of the motor can also influence the relay, which can lead to flaws. For this reason, measurements performed on an example of the targeted motors are reported and reveal a set of frequencies to avoid.

Finally, as these relays will be manufactured inside a cleanroom, microfabrication techniques will be used. Consequently, due to their tolerances and limitations, the design possibilities will be limited or induce errors in the relay behavior. For example, it has been shown that an

Chapter 4. Design of the MEMS relay

error of 10% in the thickness of the structure results in an error of 30% in the stiffness or that over etch of 10% of the width of the arm changes the stiffness as well.

Publications related to this chapter:

- F. Copt; C. Koechli; Y. Perriard : Electrostatically actuated MEMs relay for high power applications. 2016. The 19th International Conference on Electrical Machines and Systems (ICEMS2016), Chiba, Japan, November 13-16, 2016.

5 Microfabrication of the MEMS relay

Contents

| | |
|---|------------|
| 5.1 Choice of the relay manufacturing method | 72 |
| 5.2 Manufacturing | 75 |
| 5.2.1 Introduction | 75 |
| 5.2.2 The borofloat wafer process | 78 |
| 5.2.3 The SOI wafer process | 82 |
| 5.2.4 Bonding and release of the relays | 88 |
| 5.3 Measurements and discussion | 94 |
| 5.3.1 Distance between the electrodes | 94 |
| 5.3.2 Stiffness of the structure | 95 |
| 5.3.3 Switching measurements | 98 |
| 5.3.4 Contact resistance | 99 |
| 5.4 Summary and conclusion | 101 |

At the end of chapter 4, a design for the relay has been proposed. Electrostatically actuated relays are chosen considering the working, the magnetic and thermal operation environments, and its low power consumption capability. The micro-manufacturing of a relay differs from the macroscopic one in the sense that cleanroom methods have to be used. Firstly, the manufacturing methods will be discussed and the best one will be chosen. Then, the fabrication process will be described and intermediate results will be presented through measurements and images. Most of the steps have been performed at the center of micronanotechnology (CMI) which is the EPFL's main cleanroom. However, despite the numerous different available machines, the electrodeposition and the thermal compression bonding have been subcontracted to the Swiss Center of Electronics and Microtechnics of Neuchâtel (CSEM). Finally, measurements performed on the manufactured relays are compared to theoretical results.

5.1 Choice of the relay manufacturing method

The literature shows that two main tendencies exist. It is either possible to manufacture the relay layer by layer using a sacrificial layer [96, 88, 87] or by using wafer bonding [29, 50, 86, 17].

Sacrificial layer solution has a major drawback. It can be removed using wet etch and drying or by using dry etch but stiction problems can occur (using wet etch) or residual sacrificial layer (using dry etch) may remain during the release of the structures [98]. For wet etching, capillary forces can pull down the structure into intimate contact. As a consequence, close contact forces such as Van der Waals or electrostatic may appear leaving the movable structure glued into a permanent bond. When possible, an opposite force can be produced in order to separate the contact. For the dry etch solution, an organic sacrificial layer is used and can be removed with an oxygen plasma for example. The releasing process depends on the type of sacrificial layer used. As with wet etch, this method also suffers from stiction when it comes to removing large layers [28]. As a consequence, to avoid this situation, separated wafers are used and then bonded together. Note that a good bonding needs enough contact surface between the two wafers.

Modern wafer bonding techniques are now widely used in microfabrication for packaging in order to protect sensitive microfabricated MEMS or NEMS from environmental contamination or perturbation [89]. They are also used to assemble two wafers together in order to create 3D structures such as relays [29, 50, 86, 17].

Six main different types of wafer bondings can be divided into two categories: the ones that need an intermediate layer and the ones that do not need it. The principle beneath these bonding techniques is to bring the wafers into close contact in applying a pressure on them and heating them up. The created bond can either be covalent, Van der Waals, metallic or ionic. The different bonding techniques depend on parameters such as the temperature, the pressure applied or the surface roughness. They are presented below and their advantages and drawbacks are resumed in table 5.1.

Direct silicon Bonding

Direct bonding also named fusion bonding is a process based on the direct adhesion of two Si wafers with smooth surfaces while placing them in contact and heating them up to a certain temperature ($<450\text{ }^{\circ}\text{C}$, $<800\text{ }^{\circ}\text{C}$ or $>1000\text{ }^{\circ}\text{C}$) [37]. Thanks to the surface previously cleaned, polished so that the roughness becomes smaller than 1 nm and finally turned hydrophilic, the wafers bond together via Si-O-Si bridge during the annealing [10]. As the wafers already adhere at room temperature without applying any pressure, this technique does not require high pressure. Furthermore, as this technique use the same wafer type, the bonded wafers are resistant to thermal expansion mismatch.

Anodic bonding

Anodic bonding is a bonding technique used to attach a silicon wafer and a glass wafer that have a clean surface and a roughness lower than 10 nm. This technique is based on the principle that under an electric field (200-1000 V) and low temperature (200-500 °C), Na^+ cations become mobile and move away from the glass bonding interface toward the cathode creating a depletion layer at the bonded interface. A pressure is applied so that O^{2-} anions can drift towards the silicon [99]. The oxidation of the silicon creates a thin oxide layer contributing to the formation of covalent bonds. Unlike direct silicon bonding, this bonding is more sensitive to thermal expansion mismatch as two different types of wafer are used [55, 11].

Thermocompression

Thermocompression is a bonding technique that uses metal as a bonding layer between the wafers. Usually the metal used is aluminium, copper or gold. When same metals are put into intimate contact, due to the high pressure applied and the temperature, metal diffusion occurs resulting in bond formation [4]. For instance, for a "gold to gold" thermocompression, temperature should be around 260-300°C with a pressure of 1.25 to 120 MPa [102]. Using this simple metal to metal bonding technique offers the advantage of having both mechanical and electrical connections between the two wafers. Nevertheless, satisfactory surface condition are necessary in order to ensure a good bonding.

Eutectic bonding

Eutectic bonding uses alloys that directly turn from solid to liquid at a specific composition without passing through a transition phase. By adding an intermediate alloy layer between the wafers and by increasing the temperature, the metal in contact reaches its eutectic point and by diffusion and solubility, eutectic bonding is created [109]. Because the metal in contact melts, the roughness of the surface is less critical. Note that as an alloy is used, thermal expansion mismatch can result in internal stress and rift.

Glass frit bonding

Glass frit bonding is similar to thermocompression. First of all, a glass layer needs to be deposited. Then, by compression and heating the wafers against each other, the glass melts because of the temperature increase (425-450°C). Due to the viscosity of the glass when it melts, the roughness of the bonding surface is compensated [48]. The bonding between the wafers is formed during the cooling down step. Note that the thermal expansion of the glass is similar to the one of the silicon. As a result, cracks due to internal stress are reduced [49].

Adhesive bonding

Adhesive bonding uses various organic materials or inorganic intermediate layers such as epoxies, polyimides, thermoplasts or photoresists. The choice is done depending on the thermal limitation and the chemical resistance set by the targeted application. An exhaustive list is presented in [3]. First of all, the wafers have to be cleaned. Then, the adhesive layer has to be deposited on the wafer. The wafers are, then, placed in a vacuum chamber, pressed against each other in close contact and heated up (21-450°C) [24]. During this step, the adhesive layer reaches a low viscous phase. During the annealing step, the bonding is formed by a polymerization reaction of the organic molecules that forms polymer chains. As the temperature can be low, this technique is CMOS compatible. Furthermore, its main advantages is that almost any kind of wafer can be bonded using this technique.

Table 5.1 – Wafer bonding

| | Bonding | Advantages | Drawbacks |
|-----------------------------------|--------------------|--|--|
| Without Intermediate layer | Direct | <ul style="list-style-type: none"> • Strong bond strength • No thermal expansion mismatch | <ul style="list-style-type: none"> • Roughness below 1 nm • No electric conduction |
| | Anodic | <ul style="list-style-type: none"> • Strong bond strength • Low thermal expansion mismatch | <ul style="list-style-type: none"> • Roughness below 10 nm • No electric conduction |
| With intermediate layer | Adhesive | <ul style="list-style-type: none"> • Low roughness requirement • Applicable for different wafer types | <ul style="list-style-type: none"> • No electric conduction • Weak bond |
| | Glass frit | <ul style="list-style-type: none"> • Strong bond • Low roughness requirement | <ul style="list-style-type: none"> • No electric conduction • Thermal expansion mismatch |
| | Thermo compression | <ul style="list-style-type: none"> • Strong bond • Electric conduction • Low thermal expansion mismatch | <ul style="list-style-type: none"> • Flat surface |
| | Eutectic | <ul style="list-style-type: none"> • Strong bond • Electric conduction • Low roughness requirement | <ul style="list-style-type: none"> • Thermal expansion mismatch |

Firstly the anodic bonding was chosen for the first prototype because of the ease of backside alignment and good electrical insulation. However, as electrical connection between the wafer could not be guaranteed, this technique was then left out.

As table 5.1 reveals, thermocompression offers both mechanical and electric bonding. This will ensure that the upper electrodes on the top wafer will be connected to respective supplied pads on the bottom wafer and that there will be no open circuit.

5.2 Manufacturing

5.2.1 Introduction

The relay manufacturing has necessitated numerous cleanroom techniques such as lithography, metal and oxide sputtering, metal evaporation, electroplating wet and dry etch, grinding and chemical mechanical polishing. On a single wafer, 88 relays are manufactured in parallel. The final result is shown in fig. 5.1 after the two wafers are bonded together and released. The relay is composed of:

- two tracks for the signal,
- two electrodes for the electrostatic actuation,
- two anchors to hold the moveable part of the relay, hold the wafers together -i.e. bonding- and electrically connect the upper electrodes,
- rigid body for electrical contact.

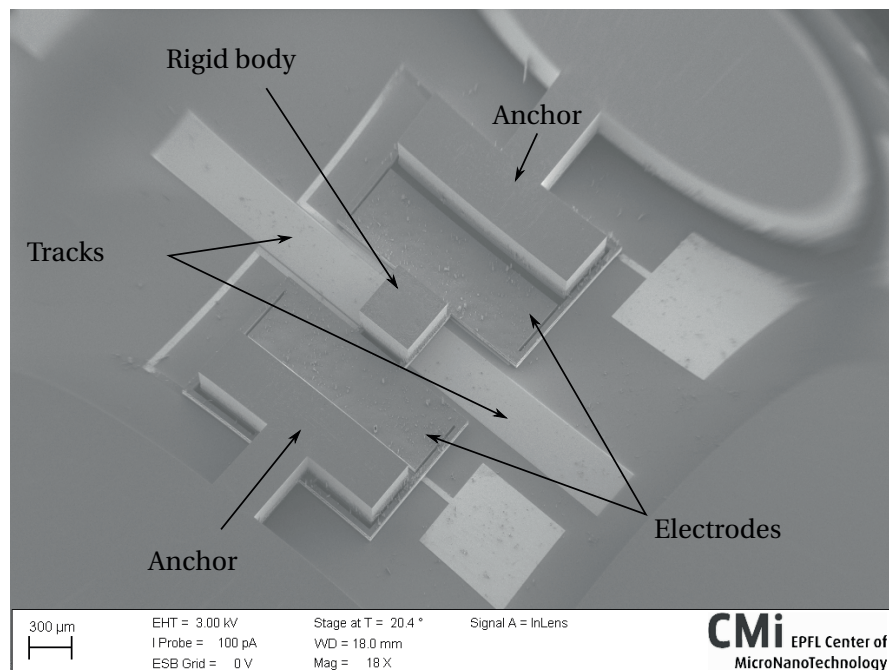


Figure 5.1 – SEM view of the manufactured relay

The relay manufacturing can be separated in four main parts:

- The bottom wafer in borofloat is the base of the structure of the relay. On this wafer, the bottom electrodes, the electrical tracks and the bonding tracks are manufactured

using different gold deposition such as sputtering and electroplating. In order to avoid breakdown voltage and short cuts, an oxide is deposited on the electrode. Finally, a protective platinum (*Pt*) layer is deposited on the exposed gold in order to avoid chamber contamination.

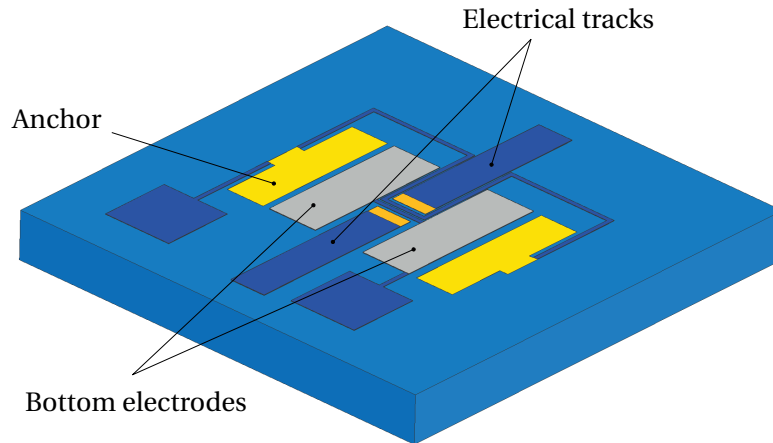


Figure 5.2 – Terminology used for the borofloat wafer

- The top wafer in silicon on insulator (SOI) will form the movable part of the relay. This wafer is thinned and structured to obtain the right relay rigidity and shape. Gold sputtering and electroplating are used to manufacture the electric tracks, the electrodes, the switching track and the surfaces necessary for the bonding (anchors).

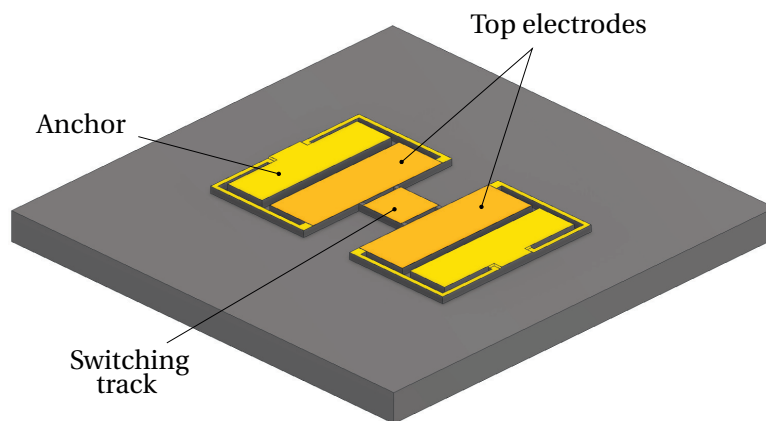


Figure 5.3 – Terminology used for the SOI wafer

- The third step consists of bonding the two manufactured wafers using thermocompression. This step is crucial because any misalignment can be disastrous in the relay operation in the sense that the contact surface may decrease and that the electrostatic force will be reduced as well.
- Finally, the top of the bonded wafer is patterned and dry etched with a Bosch process until the intermediate oxide layer in order to release the structures. The remaining oxide

is removed and the release is complete.

As described above, the manufacturing of the relay requires numerous steps and multiple lithographies, which is a critical step as well as the different etching steps. The main issues in this manufacturing is the use of contaminant materials such as gold that will limit the use of certain machines. For this reason, a good cover up is essential. Furthermore, as the wafer will be bonded, artefacts need to be used. These artefacts ensure that there is sufficient contact surface and that there is no close cavities during the bonding so that the wafers do not break during a pressure change.

For the following development, cut sections are used to emphasize the understanding. The localisation of these cross sections are shown in fig. 5.4. Note that these cross sections are not to scale to improve their visibilities (see fig. 5.4). The full process flow can be found in section C.

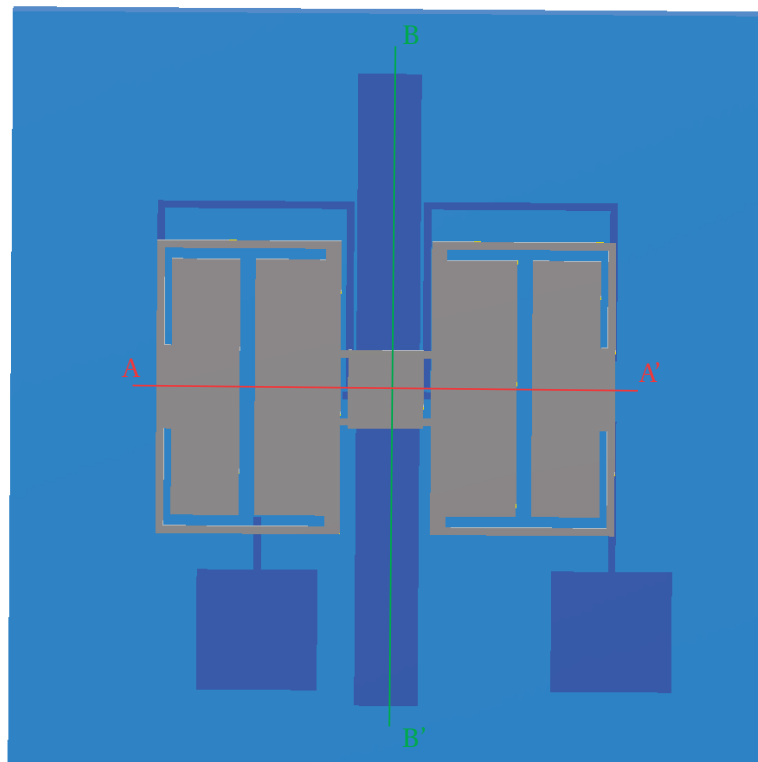

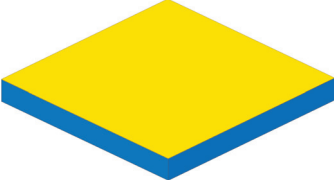
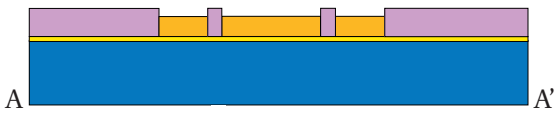
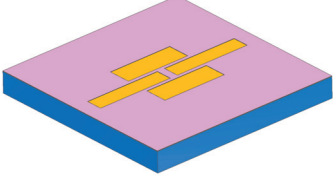

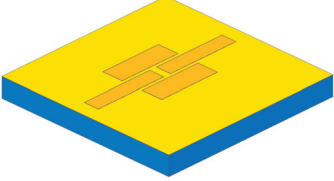

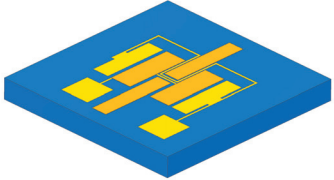

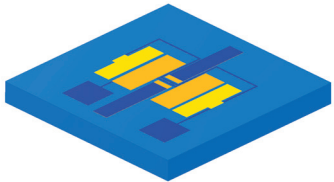

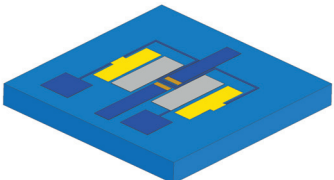

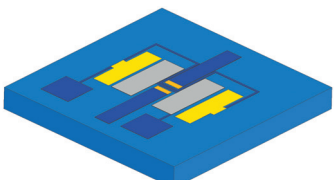


Figure 5.4 – Emplacement of cross section used

5.2.2 The borofloat wafer process

Table 5.2 – Process flow for the borofloat wafer

| Step | Cross section view | Perspective view |
|------|---|--|
| 1 |  |  |
| 2 |  |  |
| 3 |  |  |
| 4 |  |  |
| 5 |  |  |
| 6 |  |  |
| 7 |  |  |

Step 1

The manufacturing of the first wafer starts with a cleaning step performed with a piranha solution which is a mixture of sulfuric acid and hydrogen peroxide ($H_2SO_4(96\%)+ H_2O_2$). It is needed to remove organic traces that can come from the storage location, airborne or possible contaminant absorbed by the wafer surface [84]. This step is determinant as the cleanliness of the wafer has a direct impact on the proper operation of the conceived device as well as its yield.

The conducting resistance of the future relay directly depends on the thickness of the conducting layer. In order to deposit a thick layer of gold with ease it is wiser to use electroplating and grow the gold inside cavities. If sputtering would have been used followed by dry or wet etching step: dry etch would have been affected from re-deposition and wet etch would have suffered from under etch. Electroplating needs a conductive layer for the cathode in sort that positive ions of the material in the plating solutions deposited on the surface. A thin layer composed of a 20 nm adhesive layer of titanium (*Ti*) followed by a 500 nm seed layer of gold (*Au*) and then covered by a 20 nm protecting layer of titanium is then deposited. This seed layer has three purposes: the creation of the lower electrodes as well as the power track. While the first *Ti* layer enhances the adhesion to the substrate, the purpose of the *Ti* layer above the *Au* is to ensure a good protection of the pads before the electrodeposition.

Step 2 and 3

Once the seed layer is sputtered, 8 μm of photoresist is deposited (AZ9221). In order to grow 5 μm of gold inside the resist patterned cavities, a ring is left open at the extremity of the wafer. This is the surface where the current is imposed for the electro-deposition. The exposed titanium inside the pattern and the ring are removed using hydrofluoric acid (*HF*) in order to remove possible resist residue and that there is no adhesion issues. Finally the electro-deposition is performed. When the deposition is over, the resist is stripped off by immersing the wafer inside a remover. The measured cavities before the electroplating is 8.19 μm . Finally the last *Ti* on the gold seed layer is removed after the resist strip by placing the wafer in the *HF* solution.

Step 4

After the electroplating comes the patterning of the conducting tracks. The latter is divided into two etching parts.

Firstly, a 8 μm photolithography (AZ9260) is performed in order to structure the gold and form the electric tracks. Two methods are possible: using dry etch or wet etch. The dry etch is chosen because the wet etch suffers from under etch as shown in fig. 5.5, which can lead to a deterioration of the electric tracks or worst to an open circuit.

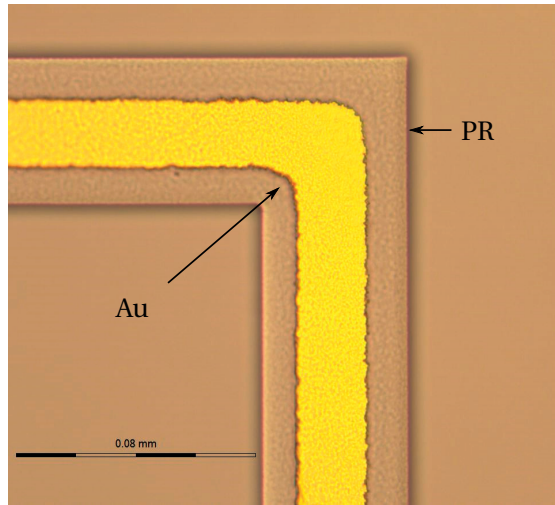


Figure 5.5 – Under etch between the photoresist and the seed layer

For dry etching, when the ion pulse forces out the etched atom of the targeted substrate, redeposition can occur and creates a fence on the side of the resist as shown in fig. 5.6. To prevent from issue, a 2 minutes reflow at 115°C on a hot plate smoothes the resist edges profile.

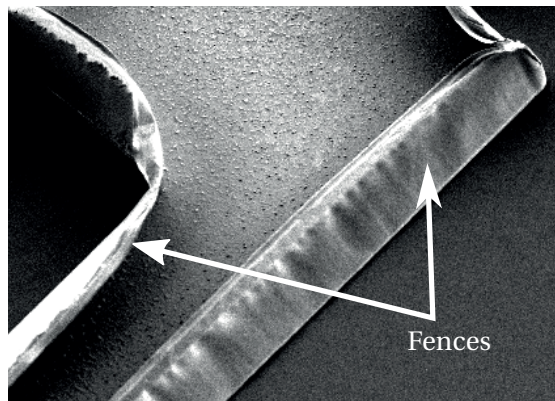
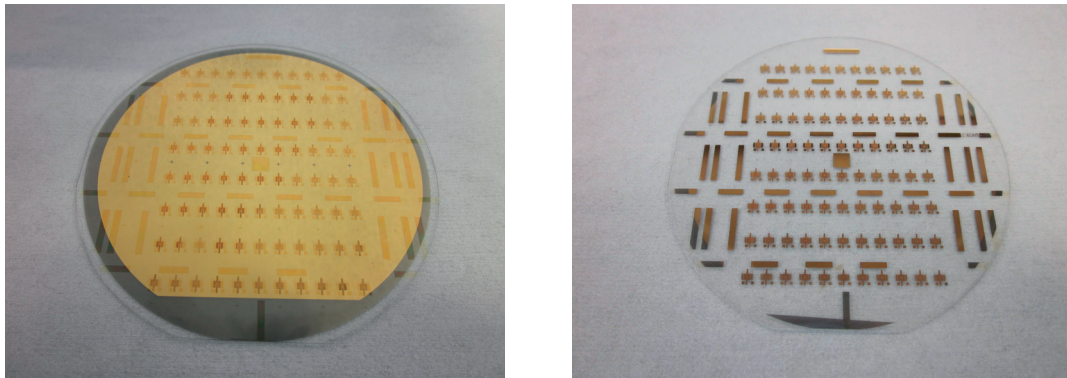


Figure 5.6 – Example of the presence of fences - picture taken after the resist strip

As the chosen etching method is dry etch using an ion beam etcher, it does not engrave the entire wafer. A gold ring is left at the extremity of the wafer. For this reason, another lithography is performed leaving this area open to remove the named gold residue using a wet etch solution composed of $KI(25 \text{ g/l}) + I_2(12 \text{ g/l})$. The resist covers all the structures, which prevents any deterioration or under etch. After the gold residue is removed, the resist is stripped. Fig. 5.7 shows the state of the wafer before and after the structuring of the electric tracks. Note that in fig. 5.7a, the ring etch has already be performed.



(a) Before the gold dry etch when the structures are covered by the photoresist

(b) After the gold dry etch and the resist strip

Figure 5.7 – Before and after the gold dry etch of the borofloat

Step 5

When the relay is finally released after the bonding, the silicon on the backside of the SOI is etched. Due to contamination restrictions, the exposed metal has to be covered. Indeed, if the gold enters in contact with the plasma, the chamber will be contaminated and the process will stop. For this reason a lift-off performed with a 20 nm *Ti* adhesive layer followed by a 100 nm layer of Platinum (*Pt*) is deposited by evaporation. The mask has been designed with an overlay of 5 μm on each dimension to ensure that the pads are completely covered.

Step 6

Now that the electric tracks and pads are manufactured, the electrodes have to be protected. Indeed, during the activation of the relay, upper and lower electrodes will come close to each other. Because of these two surfaces, the electrostatic force increases and they can come into contact in case of a proximity deflection of the electrode surface. For this reason, an insulation layer is inserted between the two electrodes. A silicon oxide (SiO_2) is deposited on the wafer with a titanium adhesive layer by sputtering. The thickness of these layers are 200 nm for the SiO_2 and 20 nm for the titanium. The latter is then patterned with a new photolithography so that the oxide remains only on the electrodes. To ensure that the electrodes are completely covered, a tolerance of 5 μm is taken on the design as in step 5.

Step 7

At this point, the addition of the oxide layer prevents the signal part to close as the electrodes with the oxide layer is higher than the power tracks. In order to solve this problem, a gold lift-off of 500 nm is performed at the contacting part on the power tracks.

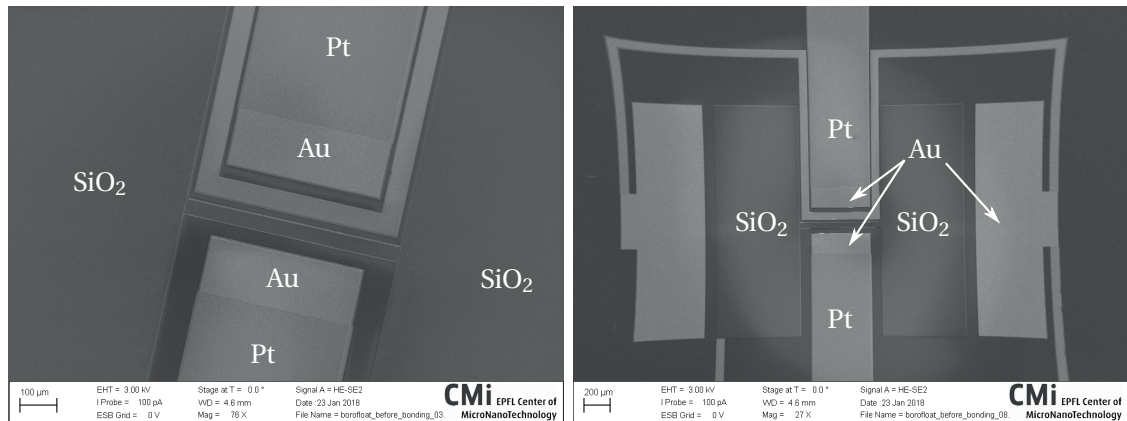


Figure 5.8 – SEM images at the end of the borofloat wafer process flow. The deformation at the extremities of the structure of the left picture is due to the limit of the optics

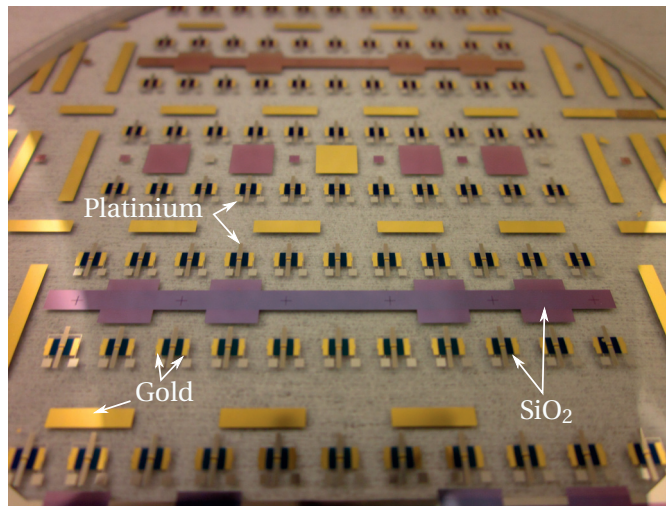


Figure 5.9 – The borofloat after all the steps have been performed

5.2.3 The SOI wafer process

Now that the base of the relay and its pads have been manufactured, the actuating part can be processed. This wafer includes the anchors between the two wafers, the upper electrodes and the power track.

Step 1

The proper operation of the relay depends on its stiffness. For this reason, the thickness of the movable part is crucial. As no SOI wafer found on the market has the targeted thickness, a standard SOI wafer is used and thinned thereafter. Thinning is performed by successively grinding and polishing on both side. The front side of the wafer is the part where the bonding will occur and also where the electrodes and the power track take place. The backside is for

Table 5.3 – Process flow for the SOI wafer

| Step | Cross section view | Perspective view |
|------|--------------------|------------------|
| 1 | | |
| 2 | | |
| 3 | | |
| 4 | | |
| 5 | | |
| 6 | | |
| 7 | | |
| 8 | | |

Chapter 5. Microfabrication of the MEMS relay

the stiffness of the contacting part as discussed in section 4.2.2. Firstly, the grinding is used to roughly reduce the wafer size by $8\ \mu\text{m}$ on the front side and by $48\ \mu\text{m}$ on the back side. The bonding depends on the quality of the contact surfaces of the bonded parts as discussed in 5.1. To ensure that the roughness caused by the grinding does not affect the bonding a polishing step performed by chemical-mechanical polishing (CMP) is necessary. The latter is $5\ \mu\text{m}$ deep on both sides of the wafer. The surface roughness after the grinding is less than $100\ \text{nm}$ with a total thickness variation (TTV) of about $1\ \mu\text{m}$.

The CMP process involves an abrasive and corrosive slurry (chemical) combined with a polished pad (mechanical). It can occur that slurry residues become incrustated on the wafer surface. For this reason, a cleaning step inside a *BHF* (7:1) bath and then into a piranha solution is necessary to remove them.

Step 2 and 3

In order to have the anchor higher than the power track and the electrodes, the top surface of the wafer has to be etched. Two different solutions exist. It is possible to either dry or wet etch the wafer. On the one hand dry etch using a deep reactive-ion etching (DRIE) is an anisotropic etch. This means that the etched slopes are perpendicular to the wafer. On the other hand, wet etch preferentially etch the silicon crystal plans at different speed. As a consequence, slopes of 54.74° appear due to the crystal orientation between the plans (Miller indices $\langle 100 \rangle$ and $\langle 111 \rangle$) as shown in fig. 5.10. In order to electrically connect the upper electrodes to the pads on the other wafer, an electrical connection between this two different heights needs to be done. Using a dry etch solution, the slope will be too steep and a loss of electrical contact can occur as shown in fig. 5.14a. As a result, the wet etch solution is chosen.

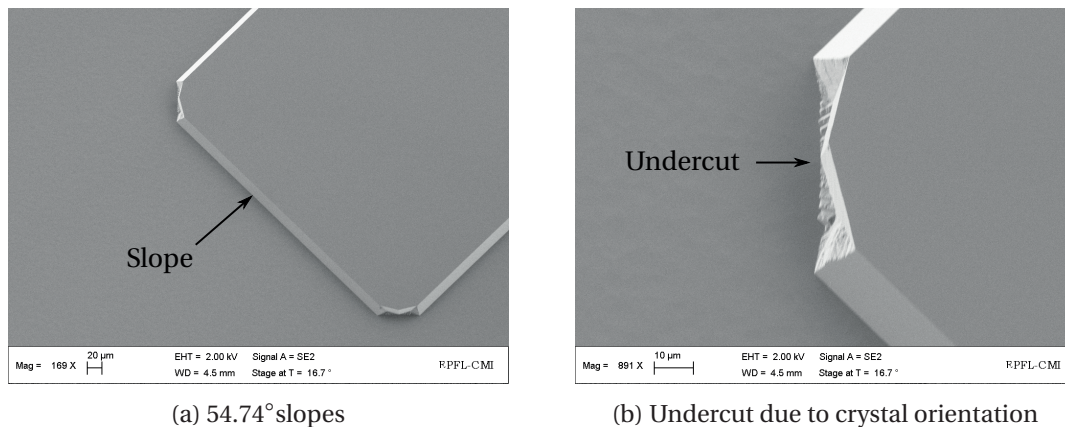


Figure 5.10 – SEM images after *KOH* etching and oxide etching with a *HF* solution

As the wafer is immersed in a 40% *KOH* bath at 60°C , the potassium hydroxide etches the silicon everywhere. In order to protect the non etched zone, a silicon oxide has to be deposited and patterned by *HF* etching. The SiO_2 evaporated deposition is not adapted because the latter is porous and the *KOH* can infiltrate through it. For this reason, a thermal oxidation is

performed after a RCA cleaning. The oxide is then etched on the front side in order to leave the desired pattern. This is possible thanks to a photolithography. The wafer can now be immersed in the *KOH*. The *KOH* etch leaves potassium residue that can be removed by immersing the wafer inside a neutralization bath (*HCl* at 37%) for at least 2 hours. After the wet etch of the silicon, the remaining oxide is removed by immersing the wafer inside a *BHF* (7:1) bath. A new silicon oxide is deposited by thermal oxidation. This oxide will be used as an insulation between the future deposited conducting layer serving for the electrodes and the power tracks and the top Si. Close cavities need to be avoided because of the overpressure that could appear during the heating step of the bonding process. As a results, artefacts are used. This will be discussed in details in section 5.2.4.

Step 4

At this point, two different levels connected by 54.74° slopes are formed. As for the borofloat wafer, a seed layer is deposited for four purposes: the manufacturing of the upper electrodes, the power contact, the electric tracks between the anchors and the electrodes and the needed layer for the bonding. This seed layer is alternatively composed of a 20 nm adhesive layer of titanium followed by a 500 nm layer of gold and then covered by a 20 nm protecting layer of titanium.

Step 5 and 6

As for the borofloat, $5\ \mu\text{m}$ of gold is grown inside the $15\ \mu\text{m}$ patterned cavities of photoresist. This time, the resist is thicker because of the $13\ \mu\text{m}$ difference of topologies between the etched part and non etched silicon parts as discussed in step 3. Thereafter, the exposed titanium is removed from inside of the pattern by immersing the wafer inside a *BHF* (7:1) bath to remove the possible photoresist residue. After the electro-deposition is done, the resist is stripped. When the wafers were returned after the electroplating, it appeared that they suffered from an excrescence around the border of the resist mask into which the gold was growing as shown in fig. 5.11.

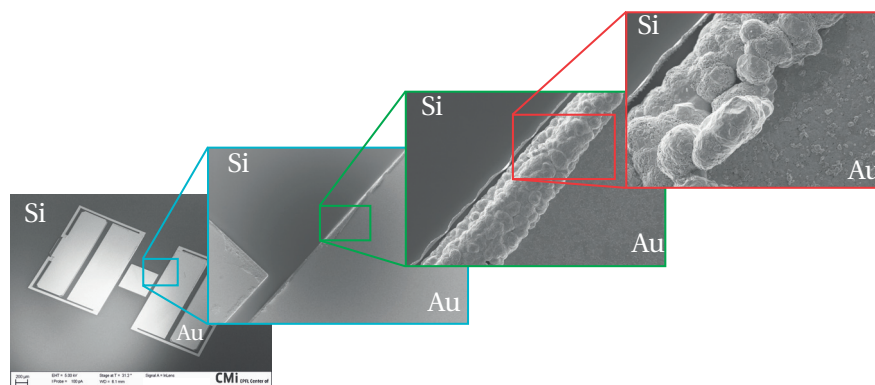


Figure 5.11 – Excrescence during a bad electroplating

Chapter 5. Microfabrication of the MEMS relay

This outgrow has been measured and could reach up to 4 μm higher than the targeted thickness as shown in fig. 5.12. Consequently, the chips where this phenomenon occurs could be obstructed preventing the relay from closing. For this reason this wafer was left out. Under proper electroplating operation the right thickness is reached as shown in fig. 5.13.

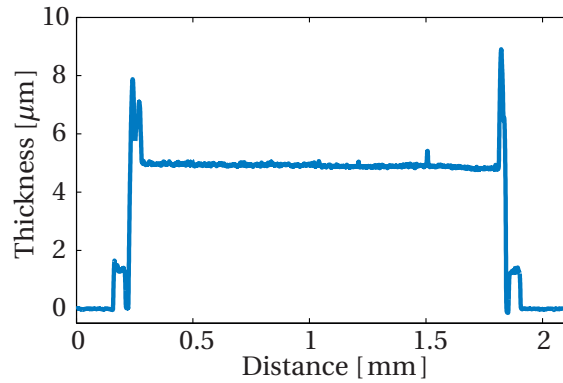


Figure 5.12 – Bad electroplating

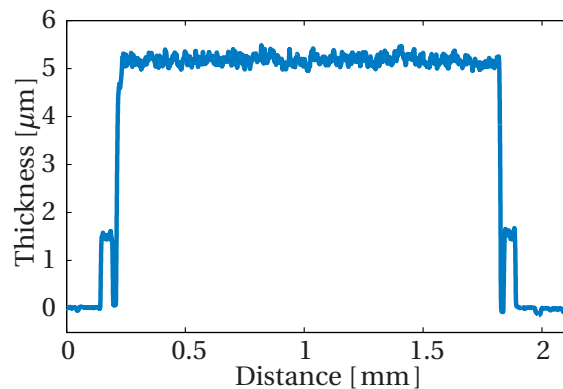


Figure 5.13 – Good electroplating

Step 7

To fabricate the electric tracks, a new photolithography is performed followed by a 2 minute reflow at 115°C on a hot plate in order to smooth the resist edge profile and avoid fences as shown in fig. 5.6. The tracks are created by etching the exposed seed layer. Silicon undercuts have to be avoided because of the risk of open circuit between the topologies. In such cases, at these undercuts, the seed layer would be badly attached, not deposited or broken as shown in fig. 5.14a. For this reason, the gold on these edges are removed and the gold remains only on the 54.74° slopes as shown in fig. 5.14c. The oxide now exposed is then removed by immersing the wafer inside a *HF* bath.

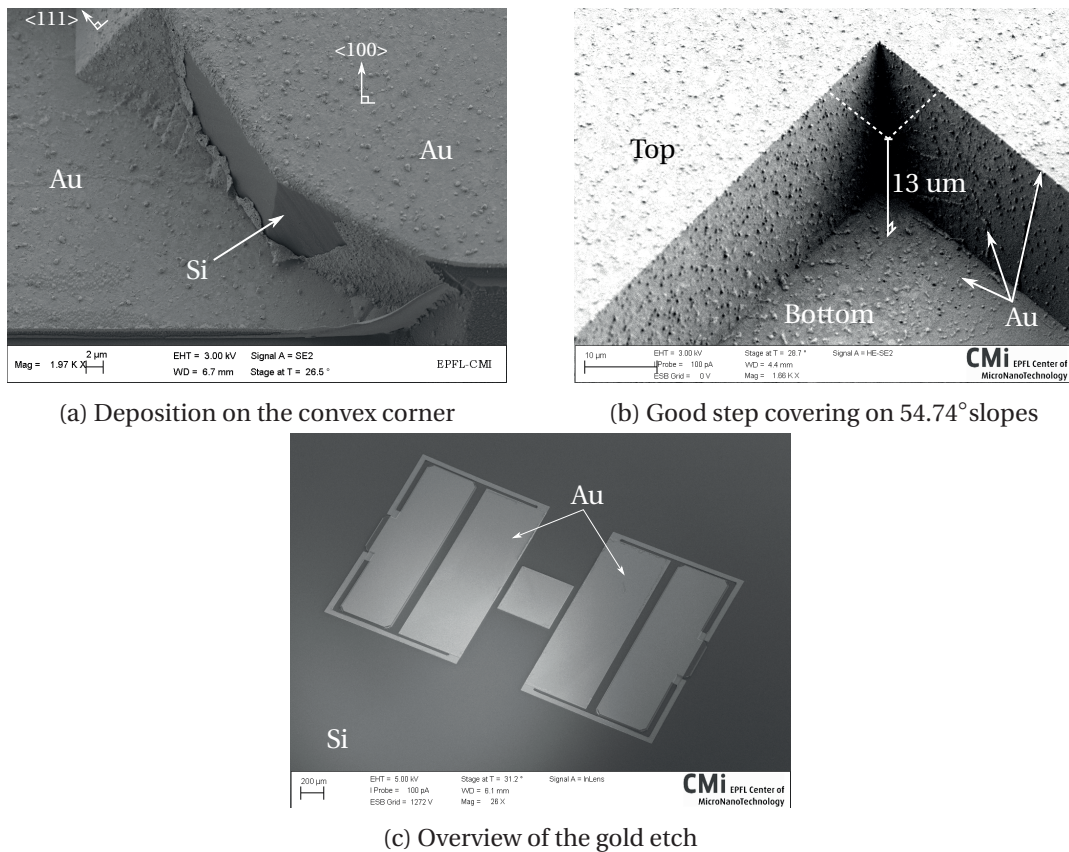


Figure 5.14 – SEM images after the gold etching

Step 8

In order to create the amovable structure, the gold is covered by a $15\ \mu\text{m}$ of photoresist. As for the borofloat wafer, if the gold enters in contact with the plasma, the latter will be contaminated. The $+5\ \mu\text{m}$ tolerance in the mask as shown in figure 5.15, protects the gold of the track even on its side. The silicon is etched on $87\ \mu\text{m}$ until the intermediate oxide layer is reached.

Once the intermediate layer of silicon of the SOI wafer is reached, the $2\ \mu\text{m}$ silicon oxide is dry etched as well using a $He/H_2/CAF_8$ chemistry. Due to a high aspect ratio 1:4.35, certain parts of the silicon oxide might be hard to remove as shown in fig. 5.16. As a result, these parts will be removed from behind after the release of the structure.

At the end of the etch, the protecting resist is stripped.

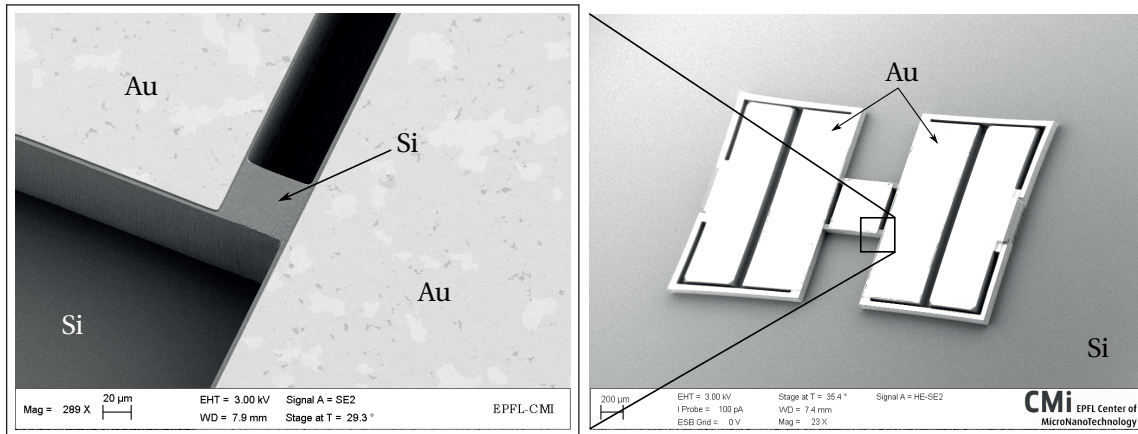


Figure 5.15 – Dry etch of the top silicon to manufacture the relay structure

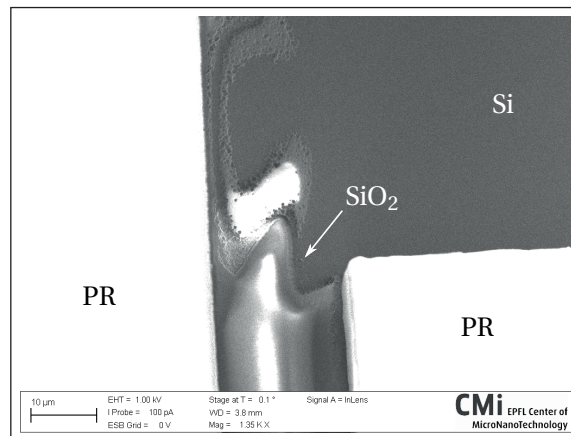


Figure 5.16 – Silicon oxide residue inside cavities

5.2.4 Bonding and release of the relays

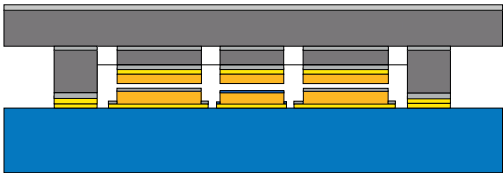
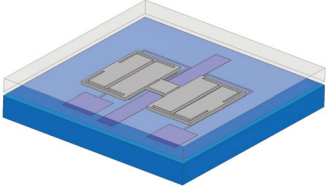
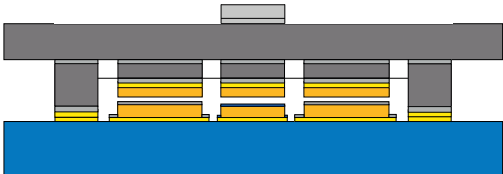
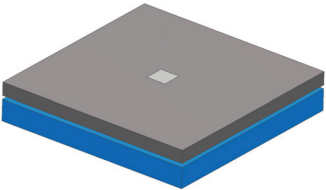
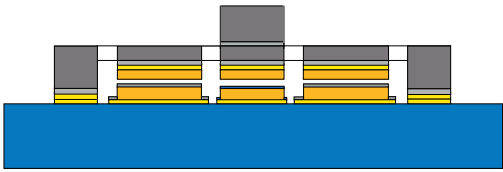
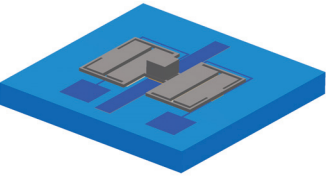
Step 1

Now that the two separated wafers are ready for the bonding, the thermocompression can be done. Firstly, a piranha cleaning is performed just before bonding in order to remove all the photoresist residue or organic contamination and have a clean contact surface. The quality of the bonding is directly dependant of the quality of the bonding surface [23]. Then, the wafers are aligned and assembled through an optical aligner. Finally, the wafers are bonded at 300°C with an external applied pressure of 0.15 MPa.

Step 2

After the bonding, the liberation process of the structure can start. The liberation of the chips can only be performed through dry etch. In the case of *HF* etching, it would have infiltrated

Table 5.4 – Process flow for the bonding of the two wafers and the release of the structure

| Step | Cut section view | Perspective view |
|------|--|--|
| 1 |  |  |
| 2 |  |  |
| 3 |  |  |

between the structures by the openings left for the bonding and would have engraved the structure from the inside. Furthermore, even if the intermediate oxide would have been left, there is no guarantee that it would not be partially broken due to its thinness.

In order to dry etch the back side silicon box, a protective oxide mask has to be used. Due to the selectivity between the silicon and the silicon oxide (150:1), 3 μm of silicon oxide is sputtered.

This layer stresses the wafer stack and a deflection can be measured. Due to the gaz leakage tolerances and the clamping method, such wafer can not be processed depending on the amplitude of the deflection. Three solutions are worth considering.

- If the clamping force can be increased, it is possible to flatten out the bonded wafer and reduce the deflection until the conform conditions are reached. Nonetheless, applying a pressure on the bonded wafer will add stress to the bonded contact and result in breaking of the contacts
- A layer can be added under the bonded wafer that will counter stress the wafer and will minimize the residual stress after the bonding.
- It is possible to use a wafer bond technique. By adding a wafer under the bonded wafer and sticking it with some wafer bond, it is possible to have a flat under surface for the machines. Furthermore, the wafer bond is a better thermal exchanger than the quick

stick. Due to the fact that fluorine etching is exothermic, the better thermal exchange is favoured.

Counter stress seed layer

In order to counteract the deflection, the modus operandi is the following:

1. Firstly, the stack wafer is modelled using an equivalent Young's modulus depending on the thickness of the deposited layers and the bonding in order to calculate the total deflection. As the wafer and seed layer are in series the equivalent Young's modulus using the rule of mixture when the applied force is parallel to the stack of materials is given by:

$$E_s = \sum_{i=1}^n E_i \cdot v_i \quad (5.1)$$

where E_i is the Young's modulus of a material and v_i is its volume fraction.

From eq. (5.1), the radius of curvature can be calculated [94]:

$$R_c = \frac{E_s \cdot t_s^2}{(1 - \nu_s) \cdot 6 \cdot \sigma \cdot t_l} \quad (5.2)$$

where ν_s is the Poisson's ratio of the substrate, E_s is the Young's modulus, t_s is the thickness of the substrate, t_l is the thickness of the deposited layer and σ is the stress of this same layer.

Finally, the deflection (δ) is found using geometry relations between the curvature radius (R_c) and the wafer diameter (d_w).

$$\delta = R_c \cdot \left(1 - \cos \left(\frac{d_w}{2 \cdot R_c} \right) \right) \quad (5.3)$$

2. Then, the model is verified through measurements performed on the stack wafer. The model predicts a deflection of 94.01 μm compared to a measured deflection of 98.52 μm when the protective silicon oxide mask is not patterned. This gives an error of 4.8% compared to the model.

In order to alleviate the stress caused by the silicon oxide layer, a compressive film needs to be deposited. The tungsten is a good candidate because it has a really high compressive coefficient. To evaluate the stress of such material different tests have been performed on a borofloat wafer and a silicon wafer, which is also used as a second verification of the model. The results are reported in fig. 5.17.

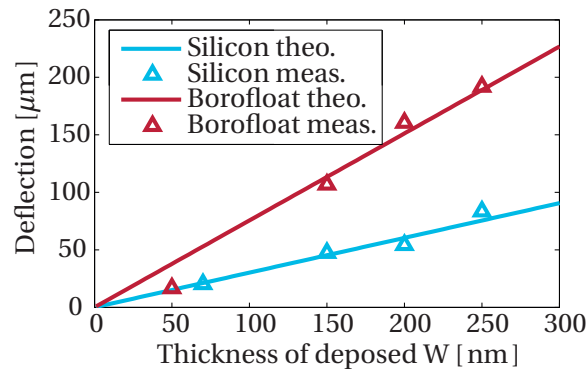


Figure 5.17 – Test of tungsten deposition to alleviate the stress of the stack wafer

The first value of the deflection of the borofloat measured does not coincide with the theoretical one. This is due to a problem of nucleation of the grain when a too thin layer is deposited.

- As the model has been verified through measurements, the necessary tungsten thickness needed is evaluated. A 1081 nm deposition is needed in order to suppress the radius of curvature of the wafer stack as shown in fig. 5.18.

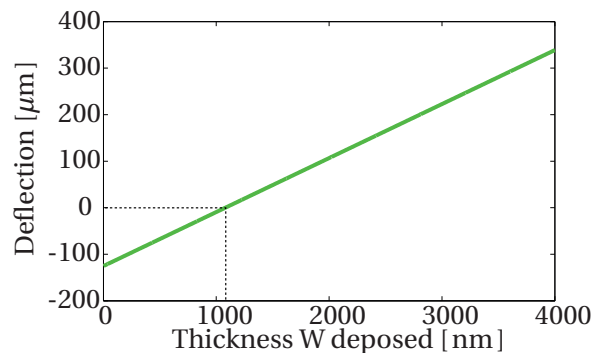


Figure 5.18 – Evaluation of the required tungsten thickness deposition

Note that fine tuning on the thickness is not recommended because multiple successive depositions can lead to stresses between these layers, which leads to delamination.

After different tests performed on wafers, due to the high internal stress of the deposited layer, a thick layer (1 μm) often delaminated. Due to the non-reliability for thick deposition, this solution has been left out.

The wafer bond In order to alleviate the bonding stress of stacked wafers that would result in weakening the bonding, another solution is the wafer bond. This solution has been chosen because of its reliability. The wafer bond technique is divided into 4 main steps:

Chapter 5. Microfabrication of the MEMS relay

- Firstly, the wafer bond is spin coated on the back side of the wafer at 1000 rpm during 1 min,
- A soft baking at 180°C is performed during 2 min,
- Then the carrier is aligned and placed on top of the wafer and the wafer bond. This is the most critical part because, due to the machine's geometrical tolerance, a misalignment could prevent the wafer to enter the machine.
- When the carrier is aligned with the wafer, they are placed in a thermal nanoimprinter between two graphite films to bond them together. The bonding is done at 180°C during 5 min under 0.175 MPa. Once the bonding time has run out, the pressing plates are cooled down and when the temperature reaches 80°C the pressure on the wafers stack is released.

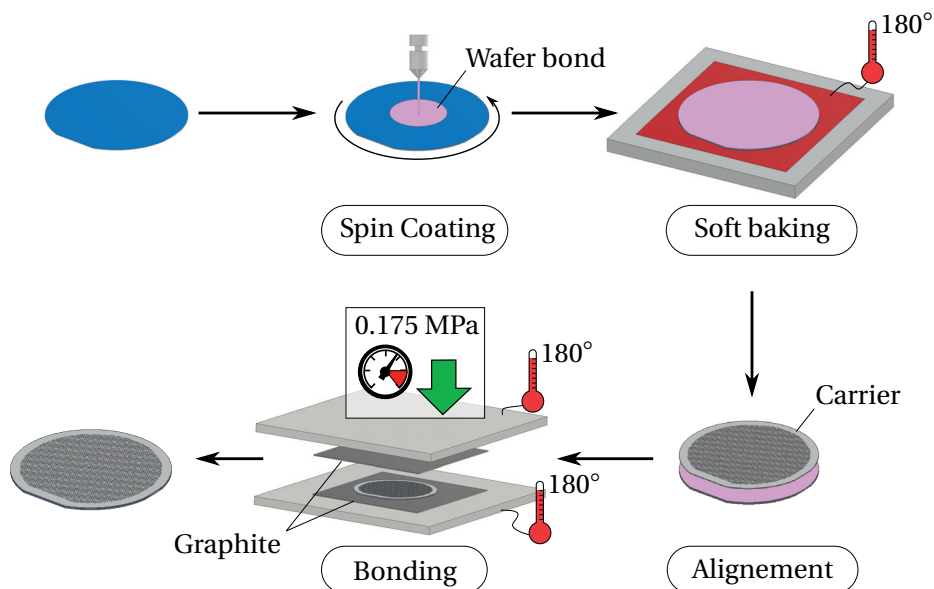


Figure 5.19 – Process flow of the wafer bond

The carrier wafer is a silicon wafer where matrix holes have been etched. Its process flow can be found in section D. The main issue with the wafer bond is its displacement between the carrier and the wafer. When the wafers are pressed against each other, the wafer bond flows through the holes due to its viscosity and increases the adhesion surface. Depending on the hole dimensions and spacing, wafer bond can pass through the holes and stick to the chuck. As a result, the optimized dimensions are holes that have a 400 μm diameter and are spaced by 1 mm for a wafer bond layer of 20 μm between the bonded wafer. Note that the wafer bond thickness depends on the spin coating speed. The carrier wafer is shown in fig. 5.20.

When the wafer bond is used, due to the addition of the carrier wafer, alignment marks under the wafer stack used for alignment of the silicon oxide etching mask are covered. For this reason, the lithography used for the silicon oxide etching should be done before the wafer

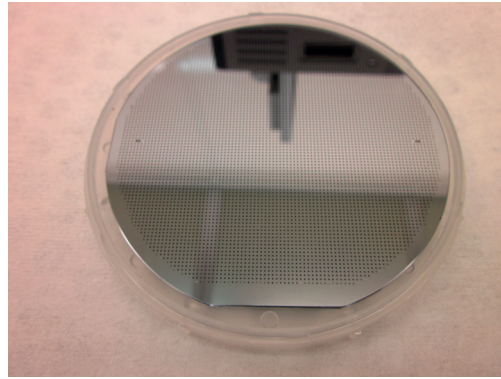
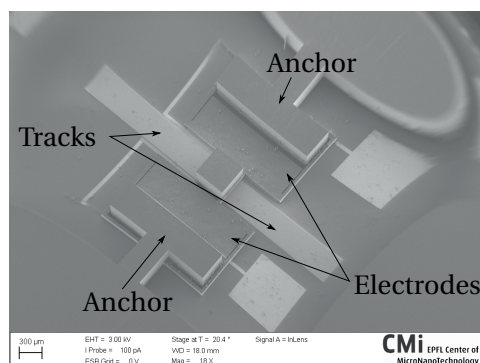


Figure 5.20 – Carrier wafer used for the wafer bond

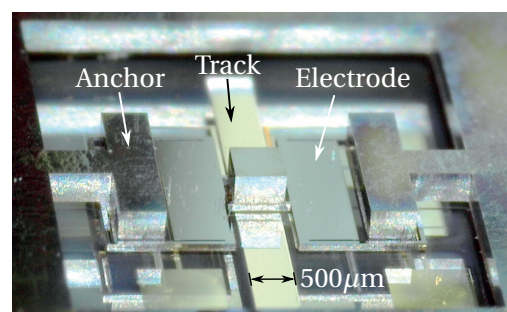
bond. However, positive resists such as AZ9221 or AZ9260 are deformed between 115-130 °C and burned at 160°C, these resists should not be used. Nonetheless, negative resist such as AZnLOF better supports temperature rise and can go up to 250°C while remaining strippable at the end of the process. The photolithography used for the silicon oxide is consequently performed before the wafer bond. Once the wafer bond process is done, the silicon oxide is etched.

Step 3

After the completion of the bonding with the wafer carrier, the relay needs to be released in order to be able to move. It is done by dry etching the backside silicon of the SOI. The silicon etch stops when the silicon oxide is reached and when the structures are released. As discussed in 5.2.3 step 8, a residue of silicon oxide between the structures may not have been completely etched. As a result, the structure may not be completely released. A final silicon oxide dry etch can be performed to clean and remove the remaining oxide. Fig. 5.21a shows the released relay. Note that the deformation on the side of the picture is due to the limitation of the optics of the scanning electron microscope.



(a) SEM view



(b) Optical microscope view

Figure 5.21 – SEM and microscope view of the manufactured relay after the release

5.3 Measurements and discussion

After the liberation, measurements are performed in order to characterize the relay. The proper functioning of the relay is done in different steps:

- verification of the air gap between the electrodes,
- verification of the mechanical properties of the relay. This will be done by measuring the stiffness of the relay,
- verification on the displacement of the relay while applying an electrical voltage between the two electrodes.

5.3.1 Distance between the electrodes

Firstly, in order to verify that there is no stiction problem between the two electrodes after the bonding the air gap is measured. Two procedures are possible:

- The air gap can be deduced by measuring the capacitance of each relay while considering that the electrodes are ideally placed in front of each other. The analytical capacitance for two electrodes placed in parallel is derived from the potential difference between the two electrodes. Starting from Gauss's law, the voltage between the two plates is given by integrating the electric field:

$$V = - \int E dl = - \frac{Q}{A \cdot \epsilon_0} \left(d - t \cdot \left(1 - \frac{1}{\epsilon_r} \right) \right) \quad (5.4)$$

where d is the distance between the two electrodes, t is the thickness of the dielectric, ϵ_0 is the vacuum permittivity, A is the electrode surface and ϵ_r is the relative permittivity of the dielectric. The parameters are illustrated in fig. 5.22.

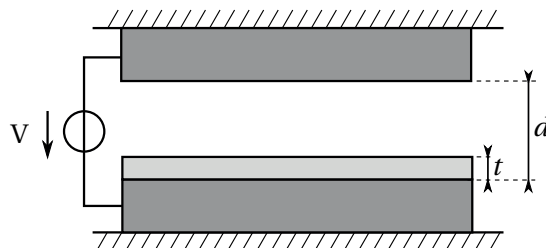


Figure 5.22 – Schematic representation of two parallel plates with a dielectric

Thus, the capacitance between two plates is:

$$C = \frac{Q}{|V|} = \frac{\epsilon_0 \cdot A}{d - t \cdot \left(1 - \frac{1}{\epsilon_r} \right)} \quad (5.5)$$

The capacitance for the relays has been measured using an impedancemeter and the results are reported in fig. 5.23.

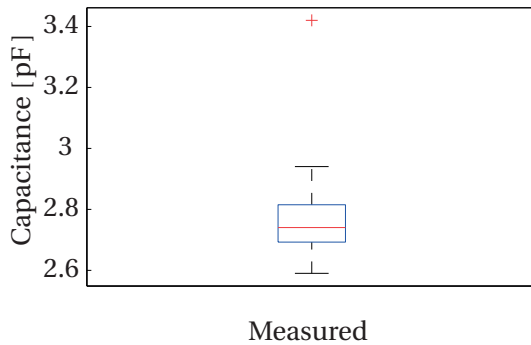


Figure 5.23 – Capacitance measured on the MEMS relays

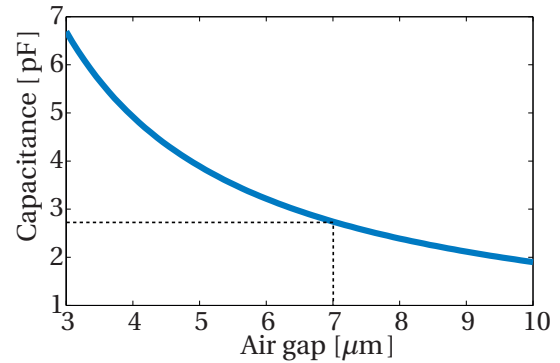


Figure 5.24 – Variation of the capacitance with 220 nm SiO₂ thickness measured according to the analytical model

Depending on the air gap, the capacitance varies. As the thickness of the dielectric had been measured after its deposition with a stylus profiler, the capacitance is deduced using the analytical calculation as shown in fig. 5.24. As a result by taking the mean value of the measured capacitance on the relays, the estimated air gap is 7 μm . As there is a about 4% misalignment measured of the total electrode surfaces, the estimated air gap is 6.73 μm . This values are confirmed by FEM, which gave a 3.57-4% of error compared to analytical results.

- Another possibility to evaluate the air gap is by measuring the breakdown voltage. As shown in section 4.2.3, for an air gap bigger than 4 μm the breakdown voltage is higher than 300 V. In practice, the measurements performed on the prototypes have revealed that the breakdown voltage was occurring at 310 V, which confirms that the air gap is bigger than 4 μm . Nonetheless this method is imprecise for the measurement of a small air gap and is a destructive test that can erode the contacts.

5.3.2 Stiffness of the structure

The theoretical stiffness of the relay has been calculated and presented in section 4.2.2 which derives from analytical and finite element calculation.

The measurements have been performed by a FemtoToolsTM sensor, which measures force up to 300 mN with a resolution of 5 μN . The sensor is fixed to a moving plate placed on a SchneebergerTM rail. The linear guidance is done by an endless screw with a pitch of 200 μm which is fixed to a stepper motor. The latter can theoretically do micro-steps as low as 33 nm up to a 8.33 μm step. A representation of the system is shown in fig. 5.25. As the output of the sensor is an analog signal, a custom ADC board has been developed. By using the same hermaphrodite connector, the PCB can directly be plugged on the sensor, which reduces the

analog noise. In order to measure the plate displacement, a laser is used, which reflects on a flat surface fixed on the movable plate.

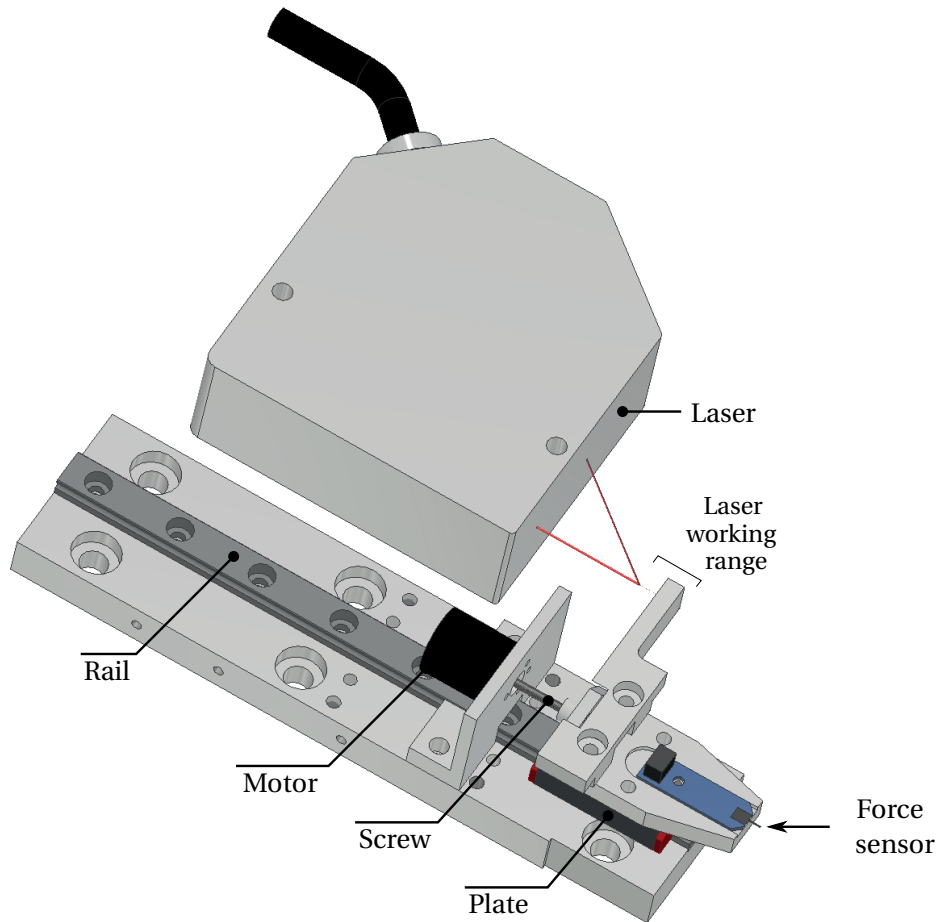


Figure 5.25 – Schematic view of the force sensor system

Different stiffness measurements have been performed on the prototypes using the force sensors as shown in fig. 5.26 and an example of the result is shown in fig. 5.27. In this figure, as the plate is driven further from the laser, the displacement is negative. As the sensor is delicate, the measurements start when the sensor is $50 \mu\text{m}$ above the relay. If the sensor would press against a non-flexible silicon bloc, the infinite counter force would be critically damaging. When the sensor touches the relay, the force applied on the sensor increases with the displacement. The slope is the stiffness, which is calculated using a linear regression. Note that the measurements are performed only in the air gap because when the relay is close the stiffness becomes infinite and the force sensor may break.

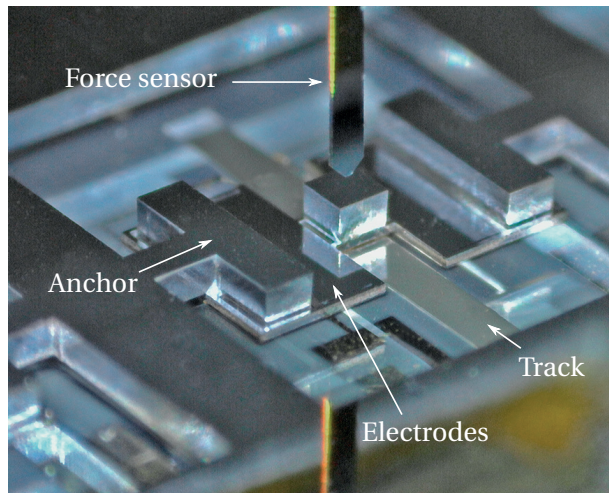


Figure 5.26 – Force-displacement measurement setup

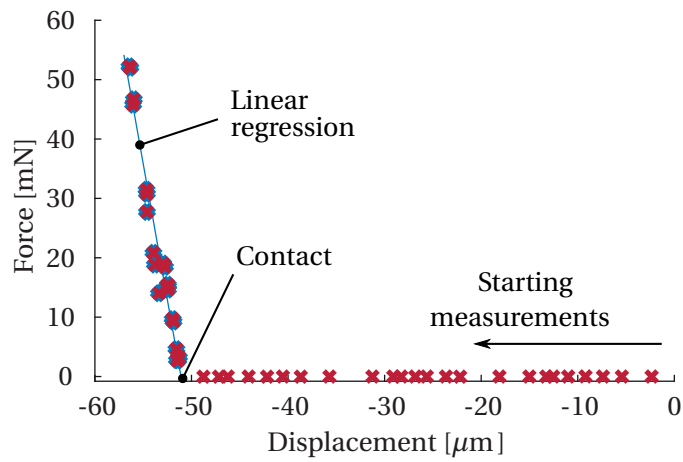


Figure 5.27 – Force-displacement measurements

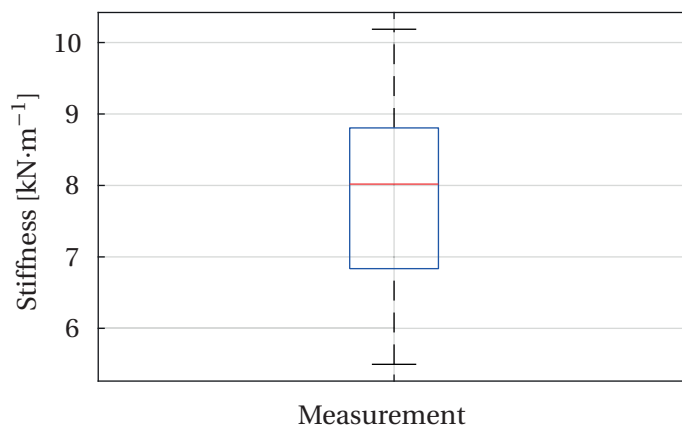


Figure 5.28 – Stiffness dispersion

Chapter 5. Microfabrication of the MEMS relay

The stiffness has been measured on the functional relays using the same presented methodology and the results obtained are reported in fig. 5.28. As a result, the mean value of the measured stiffness is $8019 \text{ N} \cdot \text{m}^{-1}$ contrary to the $2515 \text{ N} \cdot \text{m}^{-1}$ expected by FE simulation. This error mainly comes from the thickness and lateral mismatching.

The SEM measurements, profilometer measurements and laser measurements performed on the manufactured relays have shown that:

- the width of the arms have been over etch by $2.79 \mu\text{m}$
- $L_1 = 46.35 \mu\text{m}$
- $L_2 = 1140.6 \mu\text{m}$
- $L_3 = 598.1 \mu\text{m}$
- Measuring the thickness of the structure, has revealed that its value is higher than the expected one. Measurement performed with a laser has revealed that the arms are $98 \mu\text{m}$ thick. By subtracting the thickness of the gold layer, the thickness is $93 \mu\text{m}$ instead of the expected $72 \mu\text{m}$, which correspond to a 23% error. This variation of the structure implies an increase of 87% of the stiffness of the relay and by extension an increase of the pull-in voltage as explained in section 4.3.1.

A 26% error is found between the theoretical stiffness obtained from these dimensions ($5931 \text{ N} \cdot \text{m}^{-1}$) compared to the mean stiffness measured ($8019 \text{ N} \cdot \text{m}^{-1}$ see fig. 5.28).

5.3.3 Switching measurements

During the electrical test of the MEMS relay, the air gap decreases due to the electrostatic force. This displacement is measured with a laser sensor, which has a resolution of 50 nm . This laser is vertically positioned on the relay and the voltage is applied with two probes with the tip placed on the electrode pads. In fig. 5.29, the measurements performed on 5 relays are reported and two of them confronted to theoretical pull in voltage deduced from the stiffness measurement. As there is a variation of the stiffness, the pull-in voltage shifts according to eq. (4.37).

The shown deflection of the measurements confirms the expected behaviour between the electrostatic force and the spring force. However, a maximum error of 22% is found between the theoretical curve deduced from the stiffness measurements and the measured deflection when a voltage is applied to the electrodes. This error can be justified by the approximation of the stiffness measured due to the present noise (as shown in fig. 5.27) used to project the theoretical value of the deflection.

Once the pull in is done, an electrical contact is performed and the relay is turned on. However during the measurements, a breakdown voltage often occurs after a brief moment following the

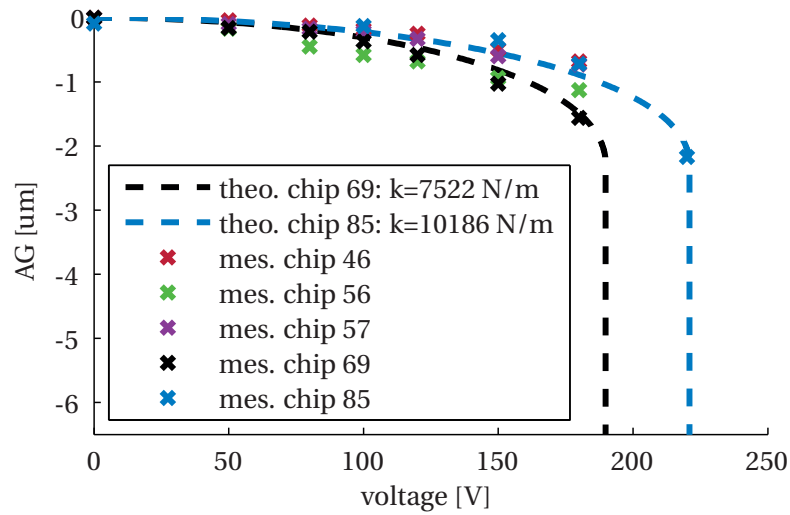


Figure 5.29 – Deflection of the relay due to an externally applied voltage

contact, which was expected. As explained in section 4.2.3, breakdown voltage for sputtered SiO₂ has been measured to be between 85-90 V. This can be avoided by placing the relay inside a hermetic package with an inert gas or by substituting the sputtered silicon dioxide layer with another insulation layer like the polyimide or parylene.

5.3.4 Contact resistance

In order to characterize the contact resistance, the setup presented in section 5.3.2 is once again used. This time, weights are used to simulate the contact force and the contact resistance is measured through four-point measurements. The results obtained are show in fig. 5.30.

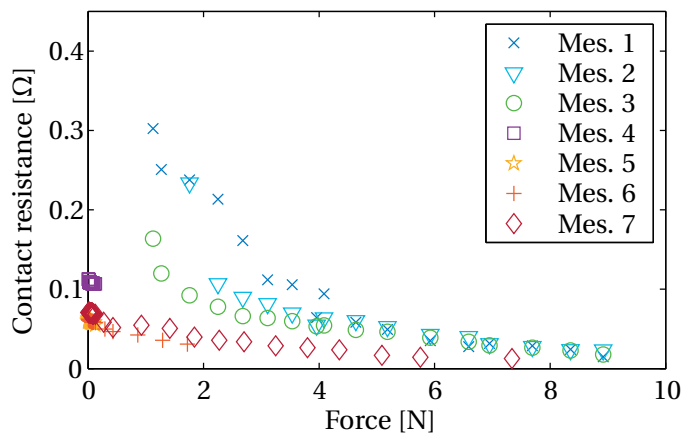


Figure 5.30 – Contact resistance measurement

For this batch of relays, because of electroplating problems, the expected contact resistance measured was far from the 168 mΩ targeted value for the 5 mN applied force. The main reason was because of the poor quality of the plating as shown in fig. 5.31 and fig. 5.32. In fig. 5.31,

Chapter 5. Microfabrication of the MEMS relay

a good contact could not be performed as gold agglomerations were created. Consequently, many contact points could not be guaranteed.

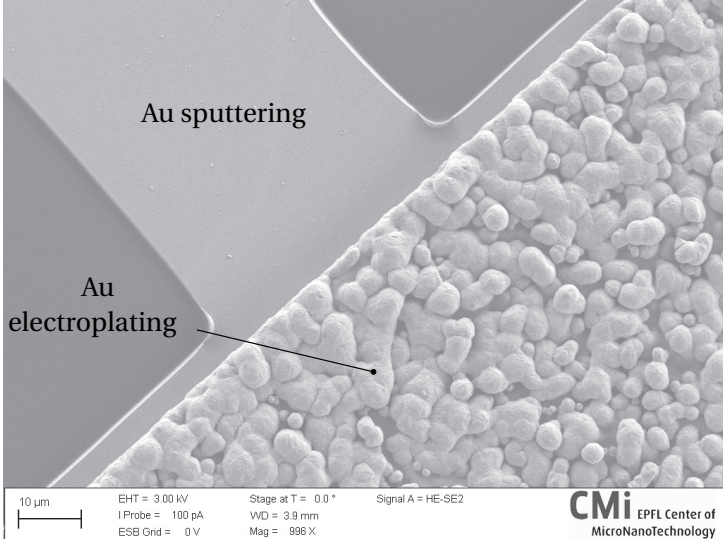


Figure 5.31 – Electroplating result

In fig. 5.32, on the side of the plating, the same type of gold agglomerations could be found but not everywhere on the contact, which decreases the contact surface.

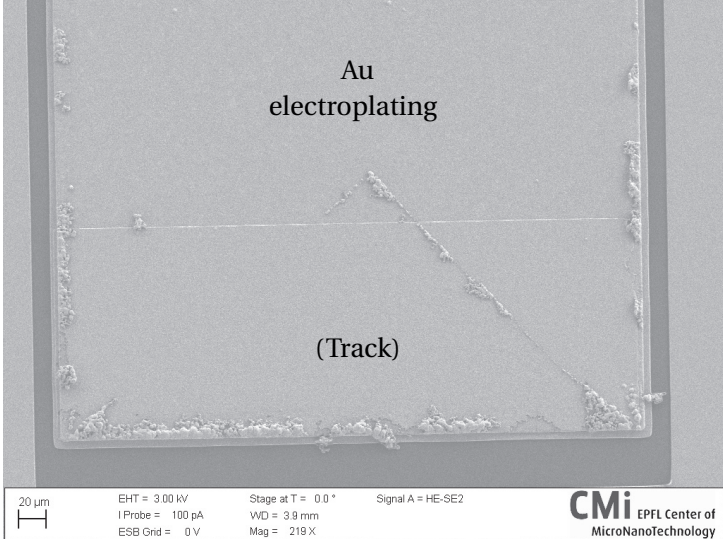


Figure 5.32 – Contact electroplating

After increasing the contact pressure and heating them, the contact resistance decreases as shown in fig. 5.30 with measurements 5 to 7. A zoom on the final contact resistance is shown in fig. 5.33.

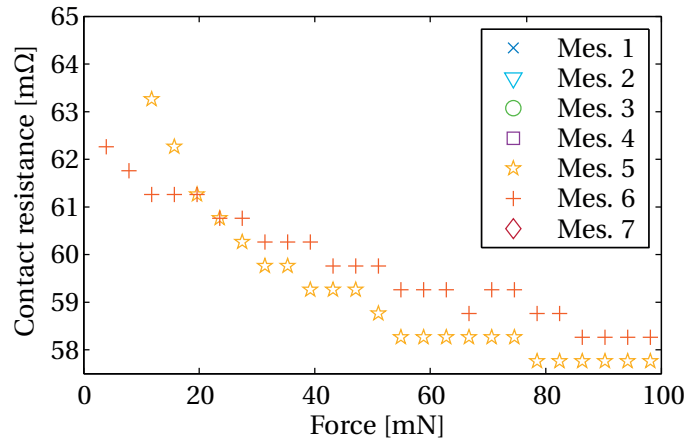


Figure 5.33 – Zoom on the targeted force

In order to solve a bad electroplating quality depot as shown in fig. 5.31 and fig. 5.32, a polishing step would have been performed just after the plating. This would have removed these contact imperfections and could have guaranteed a good flat contact surface and a lower contact resistance.

5.4 Summary and conclusion

This chapter presents the microfabrication and the characterization of the MEMS relay designed in chapter 4. A process flow comprised of 18 main steps has been developed for this purpose. The MEMS relays have been successfully manufactured through the use of two separated wafers that are bonded together. Although the liberation of the structure was a success, due to a 2 minutes over etch at the end of the process flow in order to ensure that no residual silicon dioxide were present, the success rate has drastically dropped to 18%.

In order to characterize the manufactured relays, different tests have been performed. Firstly, the capacitance between the two electrodes has been measured. This has confirmed that there were no stiction problems for the released structures and that the air gap has been measured to be $7 \mu\text{m}$. Then, in order to verify the relays proper behaviour, the stiffness has been measured through a custom designed force sensing system. The extrapolate mean value for the stiffness was $8 \text{ kN} \cdot \text{m}^{-1}$, which is 3.2 times higher than expected. Several conjectures aim to explain this difference. The main explanation is the error on the thickness of the relay, which has been confirmed through measurements and analytical calculation based on the measurements, which reduces the error to 28%. The stiffness measurements have been completed with a pull-in measurement, which have been compared with the theoretical values found with the measured stiffness. To this intent, the deflection of the structure was measured under different applied voltages. A maximum mean error of 22% of the deflection has been found between the measurements and the theoretical curve and the pull-in error is found to be less than one percent. Finally, a $64 \text{ m}\Omega$ contact resistance has been measured for a 5 mN applied force 2

Chapter 5. Microfabrication of the MEMS relay

times lower than the expected value, which was very conservative.

The obtained electrical contact and the measurements performed on the relays confirm the feasibility of the proposed manufacturing method and the fabrication of the MEMs relay from scratch with the aim to integrate them inside a permanent synchronous motor.

6 Dynamic winding reconfiguration

Contents

| | |
|--|------------|
| 6.1 Introduction | 104 |
| 6.2 Reconfiguration criterion | 105 |
| 6.3 Importance of the control strategy | 106 |
| 6.4 Electrical setup | 107 |
| 6.5 Series to parallel reconfiguration | 108 |
| 6.6 Star to delta reconfiguration | 109 |
| 6.6.1 State I & II | 109 |
| 6.6.2 State III | 112 |
| 6.6.3 State IV & V | 113 |
| 6.6.4 State VI & VII | 113 |
| 6.6.5 State VIII | 115 |
| 6.6.6 Overview | 115 |
| 6.7 Experimental result | 116 |
| 6.7.1 Series to parallel reconfiguration | 117 |
| 6.7.2 Star to delta reconfiguration | 118 |
| 6.8 Modification of the motor dynamic | 120 |
| 6.9 Experimental verification of the motor characteristic extension | 121 |
| 6.10 Conclusion | 123 |

The modification of the torque-speed limitation is performed through winding reconfiguration. The latter consists of a rearrangement of the coils terminal connections. The transient behaviour of the motor is then studied during the dynamic reconfiguration of the winding. As a result, novel control strategies are proposed in order to avoid torque jerks.

6.1 Introduction

This chapter consists of a study on the dynamic winding reconfiguration from series to parallel configuration or star to delta configuration under a 120° torque control.

The winding reconfiguration consists of a rearrangement of winding terminal connections resulting in a modification of the motor intrinsic characteristic. Two main control strategies are possible to reconfigure the winding: when the motor is stopped or dynamically

In this chapter, the dynamic solution is studied. To do a dynamic reconfiguration, it is possible to:

- stop supplying the motor when it is turning,
- reconfigure the winding when there is no current in the phases and then resupply the phases [67],
- reconfigure each phase at the time when they are not supplied [66].

The problem when stopping the power supply of the motor is the current interruption. Hence, the torque is interrupted as well, which can be disastrous for certain applications where abrupt torque variation are prohibited such as surgical ones. In order to avoid a torque interruption, the phase are reconfigured one at the time when the control is in 120° . This solution has already been explored in [66]. In the 120° control strategy, there is always a floating phase. This means that no current flows through the latter. If the reconfiguration occurs in this phase during that time, no torque interruption will occur. Note that during the overall winding reconfiguration process, the winding will become unbalanced. However, as this study [66] has been performed for a slotted synchronous motor that has high inductance, the time constant of the transient regime is high as well. This means that the current varies slowly and no torque pulse should occur. When it comes to slotless DC motor, the inductance is small. Consequently, the current variation can not be neglected because torque jerk will appear. For these reasons, a novel control strategies needs to be elaborated.

Different strategies will be proposed to avoid the torque jerk during the winding reconfiguration. When the motor is connected in star configuration, passing the winding from series to parallel is relatively simple because there is always a floating phase with no current passing through it. However, when the winding is reconfigured from star to delta difficulties appear because in delta configuration the current is flowing in all phases. Furthermore, as the time constant is small due to the fact that the winding will not be balanced during the reconfiguration process the current will jump resulting in a torque jerk. Finally, there is a phase shift of $\frac{\pi}{6}$ of the back-emf when the winding is reconfigured from star to delta.

6.2 Reconfiguration criterion

Each winding configuration modify the motor intrinsic characteristic. This means that for each configuration, the resistance, the speed constant and the torque constant are different. Table 6.1 summarizes the ratio for each winding configuration considering that each phase is composed of 2 coils that can be placed in series or in parallel and in star or in delta.

Table 6.1 – Resistance, speed and torque constant for different winding configurations

| | Y_s | Y_p | Δ_s | Δ_p |
|-------|-----------------|----------------|-----------------|-----------------|
| R | $4R'$ | R' | $\frac{4}{3}R'$ | $\frac{1}{3}R'$ |
| k_e | $2\sqrt{3}k'_e$ | $\sqrt{3}k'_e$ | $2k'_e$ | k'_e |
| k_m | $2\sqrt{3}k'_m$ | $\sqrt{3}k'_m$ | $2k'_m$ | k'_m |

Y stands for star configuration, Δ stands for delta configuration and the index s and p respectively stands for series and parallel. Then R' , k'_e and k'_m are respectively the resistance, the speed constant and the torque constant of one coil and R , k_e and k_m are respectively the phase-phase resistance, the total speed constant and the total torque constant.

The reconfiguration criterion derives from the current limitation of the motor drive. For the same electrical limitation, the torque limitation depends on the winding configuration as the torque constant is modified. Different reconfiguration scenarios are possible:

1. if the torque of the first configuration can not be reached by the following one, a torque drop will occur,
2. if the torque of the first configuration is lower than the maximum torque of the following configuration and the current is not well controlled a torque jump will occur.

In order to avoid torque jerks, the reconfiguration criterion has to be chosen when the torque of the previous configuration can be reached by the following one. Note that the second scenario can be used for implementation. Nonetheless, the current limitation has to be well controlled to avoid torque jerks. This can be illustrated by an example as shown in fig. 6.1. When the motor starts, a higher torque is necessary to place the motor in motion due to the static force that opposes to the motion (1). Then, as the motor accelerates, the back-emf increases. As a result, the current needed is reduced and the provided torque as well (2). When the torque of the previous configuration is equivalent to the maximum torque of the next one, the winding reconfiguration can occur (3) (4). After the reconfiguration, the back-emf is reduced so more current is flowing in the motor. Finally, as the motor accelerates, the back-emf increases and the current decreases (5). Note that I_1 and I_2 are respectively used for line current of phase 1 and line current of phase 2.

In summary, table 6.1 gives the criterion to change from star to delta configuration when the torque and by extension the current is $\frac{1}{\sqrt{3}}$ smaller than the maximum current possible. When it comes to change from series to parallel, the criterion reaches half of the maximum current.

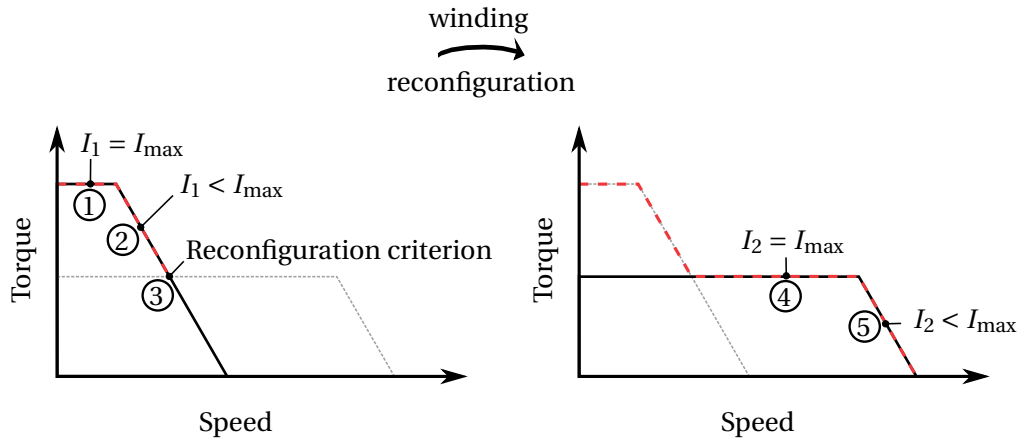


Figure 6.1 – Reconfiguration criterion

6.3 Importance of the control strategy

As explained in 6.1, there are different control strategies. The following results obtained in this section are simulations performed with PleximTM.

- The power supply of the motor can be stopped, then the winding is reconfigured and then the supply is restarted. When the power supply is stopped, no current flows in the phases. As a result, a torque drop can be noticed as shown in fig. 6.2. When the motor starts the current is maximum and then decreases as the back-emf increases until it reaches the reconfiguration criterion (3). At that time, the supply is stopped and the winding is reconfigured. Note that as long as the current supply is stopped, there is an important temporary torque loss. Furthermore, the torque is interrupted as long as the switches need to turn on. When the reconfiguration is done, the motor is resupplied and the current is maximum. Depending on the application, this interruption can not be acceptable and can also prevent the winding from reconfiguring. If this interruption is too long, the motor can lose speed and a higher torque can be required again.

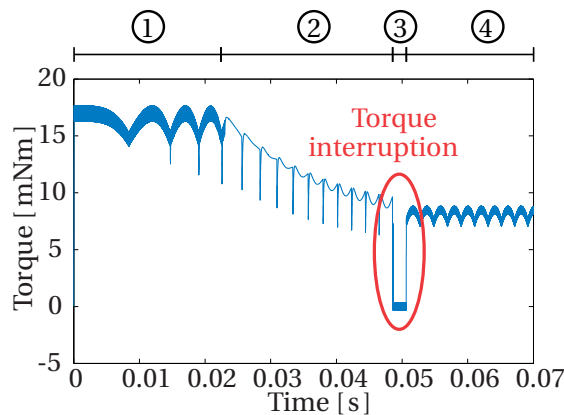


Figure 6.2 – Torque simulation when all the phase are interrupt at the same time

- Each phase can be reconfigured one at the time when it is not supplied. However, without proper current control, torque jolts can occur during the reconfiguration process when the winding becomes unbalanced as shown in fig. 6.3 at step ③. For high inductance motors, the inductance opposes itself to the current variation. However, for small inductances, the current varies rapidly. Such jerk can be disastrous for given medical applications for example.

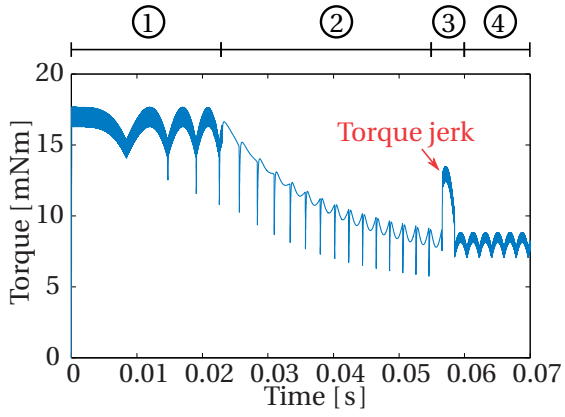


Figure 6.3 – Torque simulation with a phase per phase reconfiguration but without any strategy

For these reasons, smooth constant torque transitions during the winding reconfiguration are necessary. To do so, each phase can be reconfigured one at the time in using a fine control on the current and by extension the torque, torque jerks can be avoided

6.4 Electrical setup

As explained in 3.2, the studied motor is a three phases brushless DC motor where each phase is composed of two parallel coils. As a result twelve terminals exit the motor: two for each coils. In order to have four different winding configurations e.g. star-series, star-parallel, delta-series and delta-parallel, each coil is connected to relays that can reconfigure the winding. The electric circuit is presented in fig. 6.4.

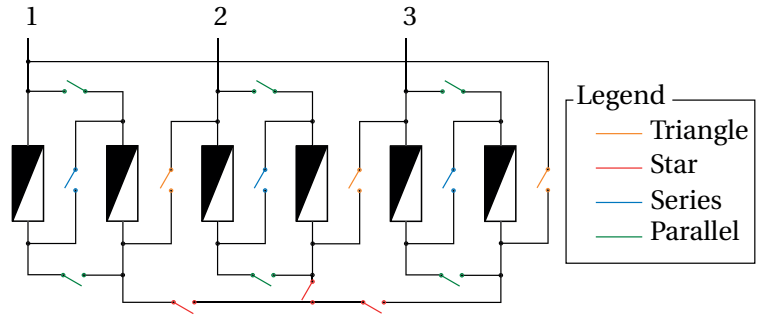


Figure 6.4 – Electric circuit for the winding reconfiguration - inspired from [66]

6.5 Series to parallel reconfiguration

In order to reconfigure the winding from series to parallel when the winding is in star configuration, the winding reconfiguration is made in three steps. As said, the command used is a 120° command control, this means that there is always a floating phase and two supplied phases. The phase is floating during $\frac{\pi}{6}$ electrical angle. Depending on the motor speed, the phase reconfiguration timing can be known.

As shown in table 6.1, the torque constant is divided by two when the winding changes from series to parallel. As a consequence, for the same maximum current, the maximum torque when the winding is in parallel configuration is half its series value. As a result, the reconfiguration criterion is when the current becomes half of its maximum as shown in fig. 6.5

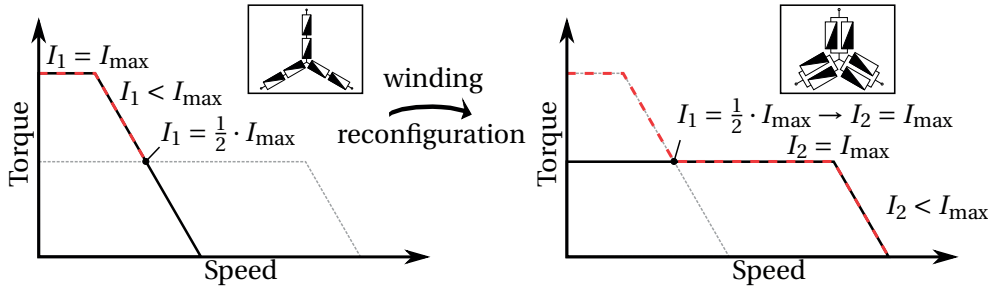


Figure 6.5 – Reconfiguration criterion for series to parallel

In order to avoid torque jerk, three steps are necessary. Everything starts when the reconfiguration criterion is attained. At the time, one phase is floating and the current is half of its maximum.

$$M_{reconf} = 2\sqrt{3} \cdot k'_m \cdot \frac{I_{max}}{2} \tag{6.1}$$

Then, at the next step, a new phase becomes floating. At the time, the winding becomes unbalanced i.e. one phase reconfigured and one not reconfigured.

$$U_{e\text{tot}} = U_e e^{j\alpha} \left[2 - e^{j\left(-\frac{2\pi}{3}\right)} \right] \tag{6.2a}$$

$$= \sqrt{7} U_e e^{j\left(\alpha - \frac{\pi}{9}\right)} \tag{6.2b}$$

As shown with eq. (6.1) and eq. (6.2), the current amplitude should be $\frac{\sqrt{3}}{\sqrt{7}}$ of the maximum current in order to avoid torque jerk. Note that in order to be perfectly correct a phase shift of 10° appear. This means that the commutation should be delayed by 5° electric, which will be the same for the next step. Finally, at the next reconfiguring step, the two supplied phases are already reconfigured. The current can already be maximum in order to keep the torque constant. The currents for all phases are shown in fig. 6.7. The optimized torque control that allows a smooth torque transition during the winding reconfiguration is presented in fig. 6.6.

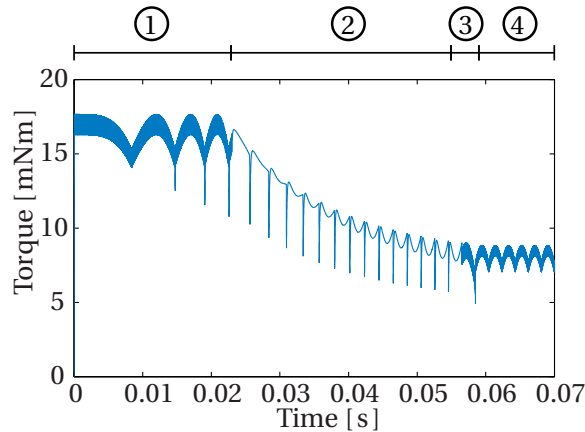


Figure 6.6 – Simulated winding reconfiguration using current control strategy

6.6 Star to delta reconfiguration

The winding reconfiguration from star to delta is more challenging than the series to parallel reconfiguration because in delta configuration the current flows in all phases all the time resulting in torque jerk at the last reconfigured phase. Furthermore, the back-emf shifts by $\frac{\pi}{6}$ by passing from star to delta.

In order to ensure no torque jerk, two factors have to be taken into consideration: the amplitude of the current, which gives an information on the torque and the commutation angle. Indeed, as soon as the amplitude of the current is adapted, the vectorial addition of the back-emf value of each supplied phase will give an information on its shift and the angle of commutation. The latter is chosen when the torque of two successive steps are the same. Note that, as a fine control on the commutation angle needs to be done, the position of the rotor has to be accurately known.

The overall winding reconfiguration from star to delta is divided into eight steps, which are presented in fig. 6.8. Note that the red color shows where the current is present in the phase. In order to proceed from one step to the next step, the torque of the former must match the torque of the latter. This means that the maximum amplitude can be controlled with the current. As it is a 120° control small variations of the torque appear due to the back-emf. Nonetheless, the torque jerk can be avoided in choosing the commutation angle when the back-emf are equal.

6.6.1 State I & II

As shown in table 6.1, the torque constant is divided by $\sqrt{3}$ when the winding changes from star to delta. As a result, for the same maximum current, the maximum torque when the winding is in delta configuration is $\frac{1}{\sqrt{3}}$ smaller than when it was in delta which is the reconfiguration criterion. In this example, this occurs when phase 1 and 2 are supplied. As a result phase 3 is

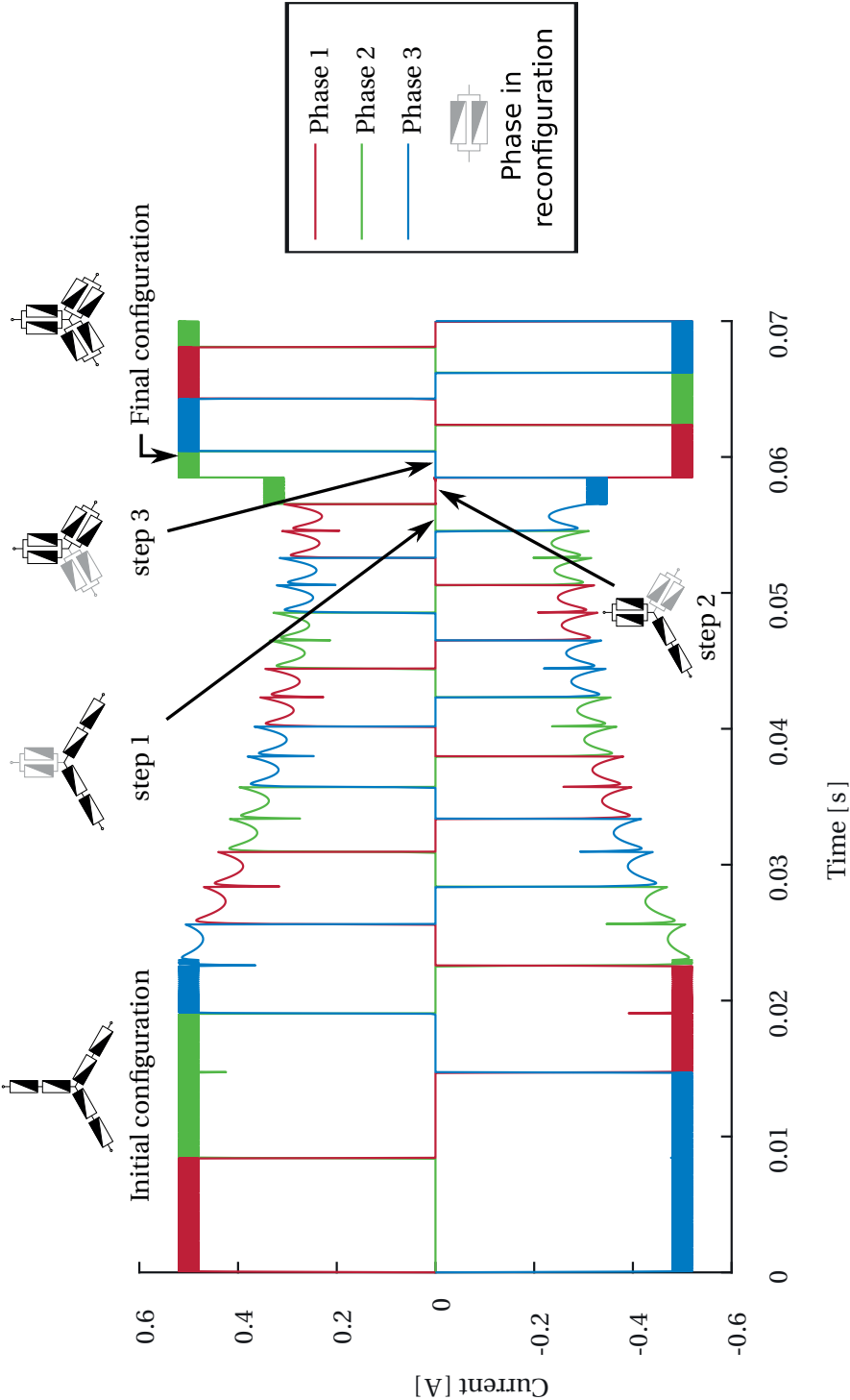


Figure 6.7 – Simulated current while reconfiguring the winding

6.6. Star to delta reconfiguration

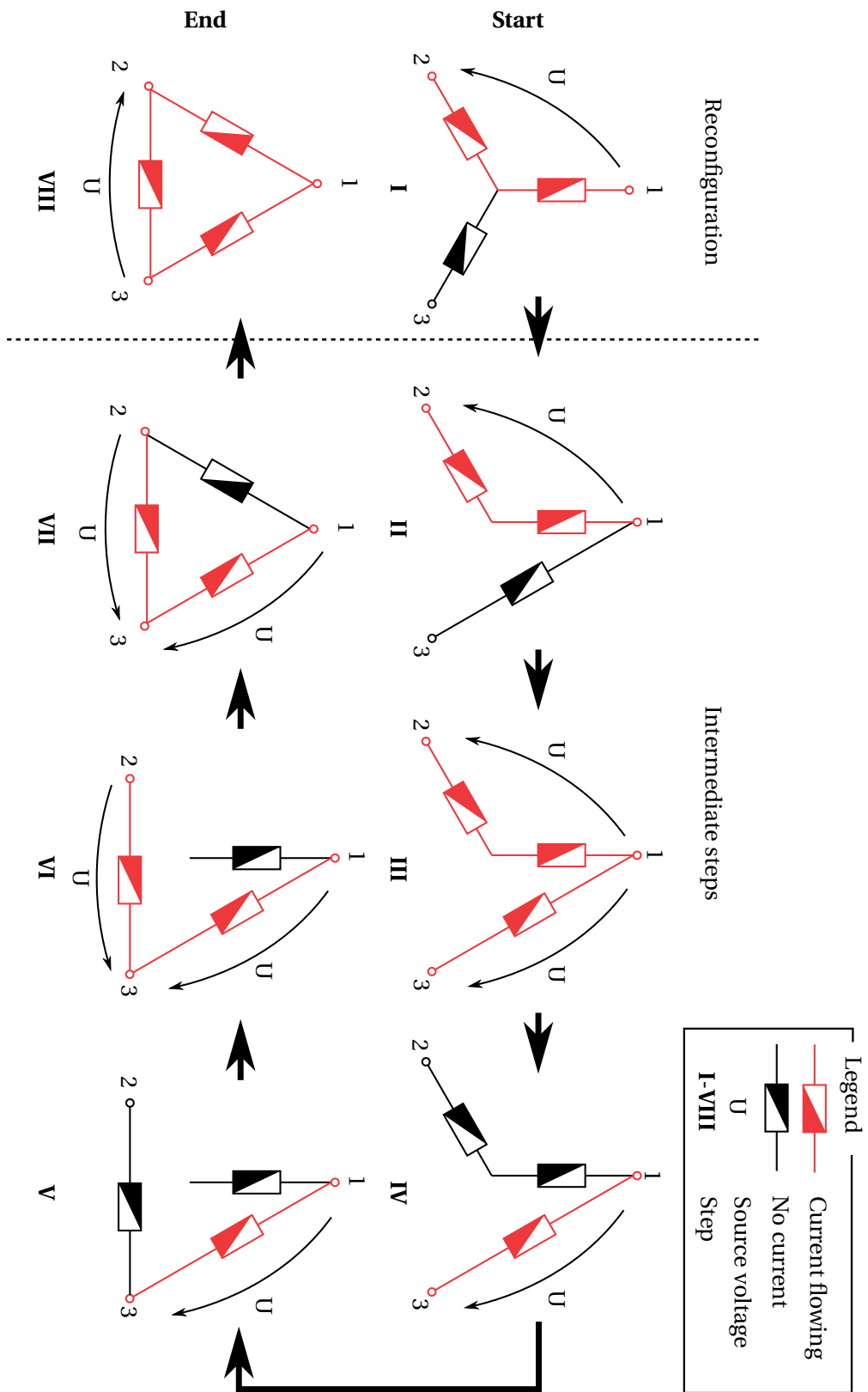


Figure 6.8 – Star to delta reconfiguration steps - the current flow is represented in red

floating (no current flows through it) and can be reconfigured.

The torque at this time is expressed as shown in eq. (6.3).

$$M_1(I_1) = \left(\sin(\delta) - \sin\left(\delta - \frac{2\pi}{3}\right) \right) \cdot k_m \cdot I_1 \quad (6.3a)$$

$$= \sqrt{3} \cdot \sin\left(\delta + \frac{\pi}{6}\right) \cdot k_m \cdot I_1, \quad (6.3b)$$

where δ is the phase angle between the back-emf and the source voltage and I_1 is the line current.

Consequently, the torque value during the reconfiguration is:

$$M_1\left(I_1 = \frac{I_{\max}}{\sqrt{3}}\right) = \sin\left(\delta + \frac{\pi}{6}\right) \cdot k'_m \cdot I_{\max}, \quad (6.4)$$

where I_{\max} is the current limitation.

6.6.2 State III

Now that phase 3 is reconfigured a transition step is needed. By passing from step II to step IV directly a torque drop would have occurred because of the delay in the commutation to avoid torque jerk. As a result an intermediate step where all the phases are supplied is needed. Here, the current is controlled so that the same current amplitude flows through phases 12 and 13. As a result, the torque for this step is:

$$M_2(I_2) = 2 \cdot \sin(\delta) \cdot k'_m \cdot I_2 \quad (6.5)$$

where I_2 is the line current.

In order to have the same torque, the current amplitude has to be:

$$I_2 = \frac{I_{\max}}{2} \quad (6.6)$$

Now that the current amplitude to control the torque is found, the commutation angle needs to be deduced. As a result eq. (6.5) is compared with eq. (6.3).

$$\sin(\delta) = \sin\left(\delta + \frac{\pi}{6}\right), \quad \delta \in [0, 2\pi[, \quad (6.7)$$

And, the commutation angle is $\delta = 75^\circ$.

6.6.3 State IV & V

The same methodology is used for this step. Here, phase 3 is supplied and phase 1 and 2 are floating. Phase 2 is reconfigured. The current limitation is deduced from the torque eq. (6.8).

$$M_3(I_3) = \sin\left(\delta + \frac{2\pi}{3}\right) \cdot k'_m \cdot I_3 \tag{6.8}$$

As eq. (6.8) has the same amplitude than eq. (6.3), the current is limited to its maximum amplitude. The commutation angle is found by comparing eq. (6.3) and eq. (6.5).

$$-\sin\left(\delta + \frac{2\pi}{3}\right) = \sin(\delta), \delta \in [0, 2\pi[\tag{6.9}$$

As result, the commutation angle is $\delta = 120^\circ$.

6.6.4 State VI & VII

Now, two phases out of three are reconfigured. The last phase reconfiguration is challenging because as soon as the last one is reconfigured, the current will flow in all phases and a torque jerk will appear.

This torque jerk can be avoided if the current shape in each phase is as presented in fig. 6.9a. In this figure, 1 means that the current is positive and flows in the phase. Reciprocally, -1 means that the current is negative. As the phase current can not be directly controlled, the line current has to be deduced in using Kirchoff's Law as shown in fig. 6.9b.

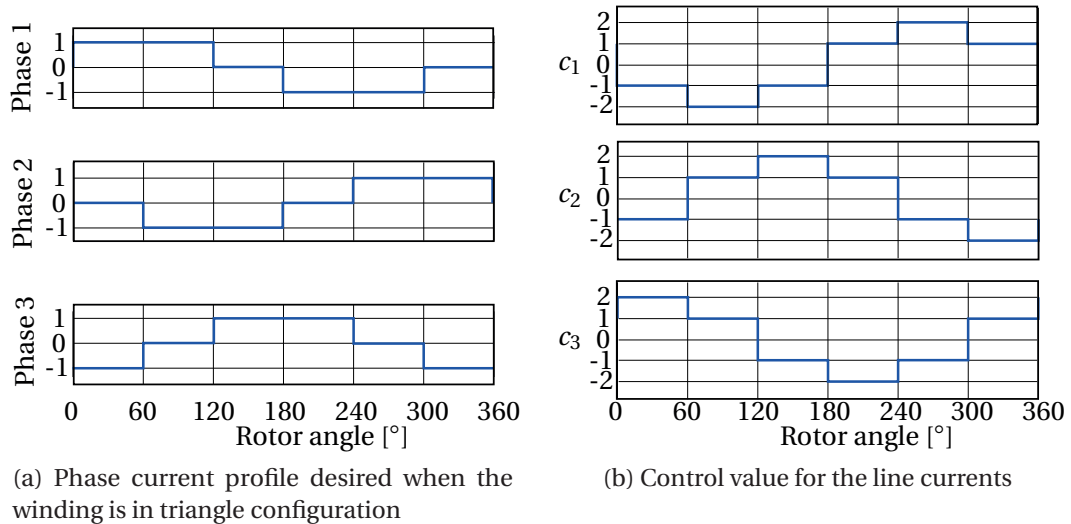


Figure 6.9 – Control signal for each phase

The control loop for each phase is given in fig. 6.10 where i is used to represent the phase. The signal value found in fig. 6.9b is multiplied by a constant (k) used for the current limitation.

Chapter 6. Dynamic winding reconfiguration

From there a current limitation value is found and compared with the measured current. The difference between these two currents pass through a Schmitt trigger which outputs $\{-1, 1\}$ where 1 means that the upper transistor of the bridge it turned on and -1 means that the lower transistor of the bridge is turned on. The $\frac{u}{u}$ block ensures that the transistors are on only when required.

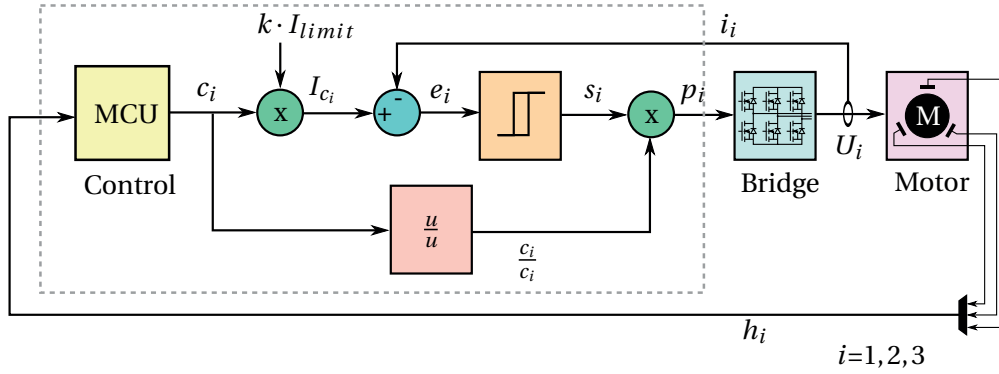


Figure 6.10 – Current control loop

In using the methodology of the previous steps, the torque for step VI & VII is:

$$M_4(I_4) = \sqrt{3} \cos(\delta) \cdot k'_m \cdot I_4 \quad (6.10)$$

In order to have a constant torque the current should be limited to:

$$I_4 = \frac{1}{\sqrt{3}} \cdot I_{\max}, \quad (6.11)$$

Note that, as the command is 1 for phase 1, 1 for phase 2 and -2 for phase 3, the current amplitude in the lower potential will be $\frac{2}{\sqrt{3}}$. As a consequence, this line current will have a temporary increase of 15.5% of the current limitation. If this current increase is not possible, the winding reconfiguration can be done when the torque is 15.5% lower. This will guarantee that the current does not exceed the bridge maximum capability.

The commutation angle can be obtained from:

$$-\cos(\delta) = -\sin\left(\delta + \frac{2\pi}{3}\right) \quad (6.12)$$

As result, $\delta = 165^\circ$.

Note that this algorithm can also be used to switch from series to parallel when the motor is in delta configuration due to the fact that there is always a floating phase.

6.6.5 State VIII

Finally, all phases are reconfigured, the current can be maximum in order to have the maximum torque in this configuration. The commutation angle to change to this configuration is:

$$\sin\left(\delta - \frac{2\pi}{3}\right) = -\cos(\delta), \delta \in [0, 2\pi[, \tag{6.13}$$

$$\delta = 195^\circ.$$

6.6.6 Overview

Table 6.2 summarizes the commutation angle and the current limitation for each step of the winding reconfiguration from star to delta.

Table 6.2 – Commutation table during the winding reconfiguration

| State | I&II | III | IV&V | VI&VII | VIII |
|----------|---------|---------------|-----------|----------------------|-----------|
| δ | [30 75[| [75 120[| [120 165[| [165 195[| [195 240[|
| k | 1 | $\frac{1}{2}$ | 1 | $\frac{1}{\sqrt{3}}$ | 1 |

where k is the current limitation constant and δ is the phase between the voltage and the back-emf.

The evolution of the current signal during the winding reconfiguration from star to delta is reported in fig. 6.11.

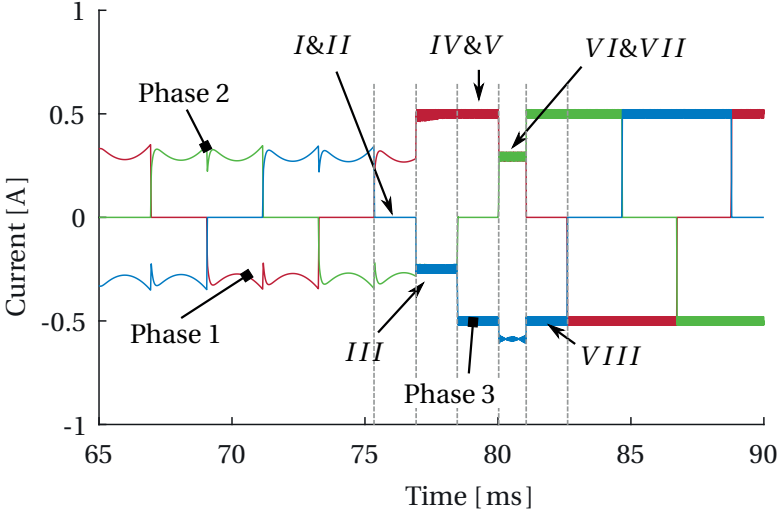


Figure 6.11 – Simulated current signal during winding reconfiguration from star to delta

Chapter 6. Dynamic winding reconfiguration

The resulting torque for reconfiguring from star to delta using the strategy is given in figure fig. 6.12.

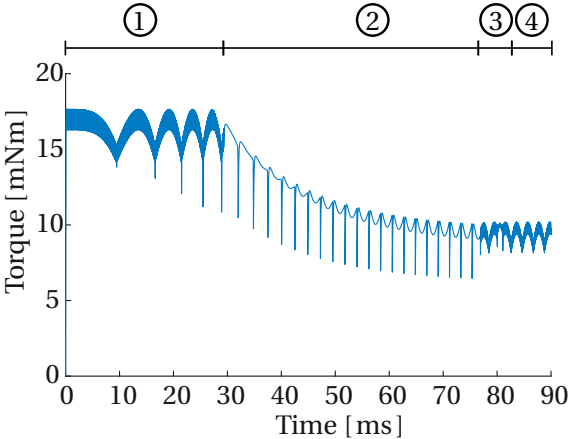


Figure 6.12 – Evolution of the simulated torque while accelerating

6.7 Experimental result

A custom drive electronic shown in fig. 6.13 has been realised to confront the simulated results with real measurements performed on the prototype presented in section 3.2. Note that the the experimental bench has to be able to control the bridge, set the winding in the desired configuration and load to the motor.

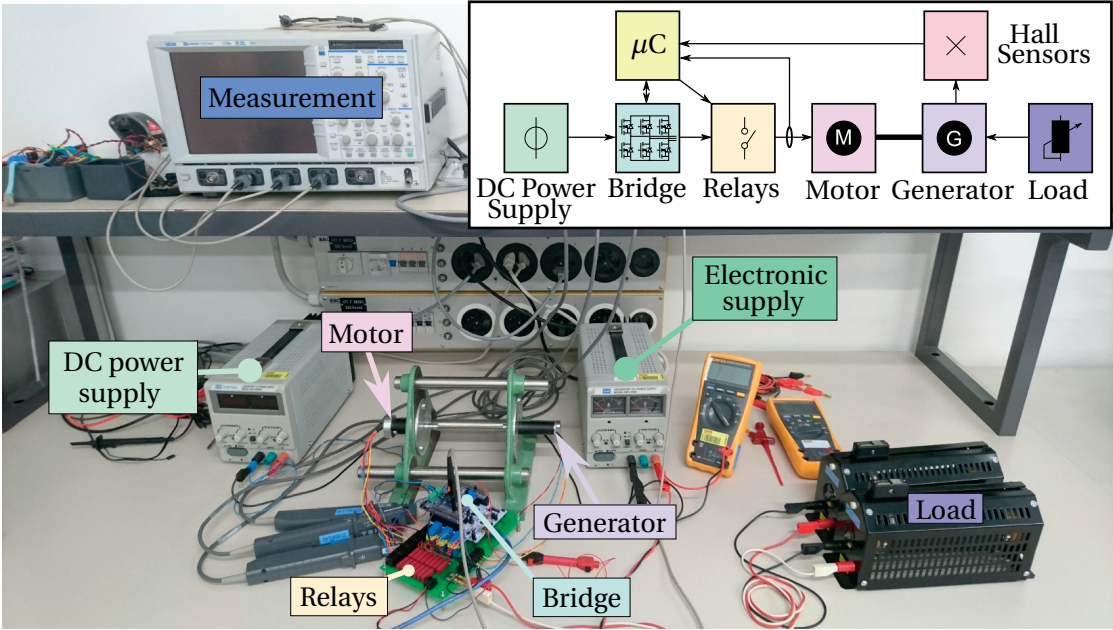


Figure 6.13 – Setup for the control command

The electronics is composed of three PCB connected in stack. The top PCB and the one below are off the shelf development boards. The top one is a classic 6 transistors power bridge combined with a drive stage and the lower one has the micro-controller and different I/O that are used to control the relays. The third board includes the relays and a drive stage. The design of this board is reported in appendix ???. Furthermore, current sensors are added in order to measure phase current as shown in fig. 6.14.

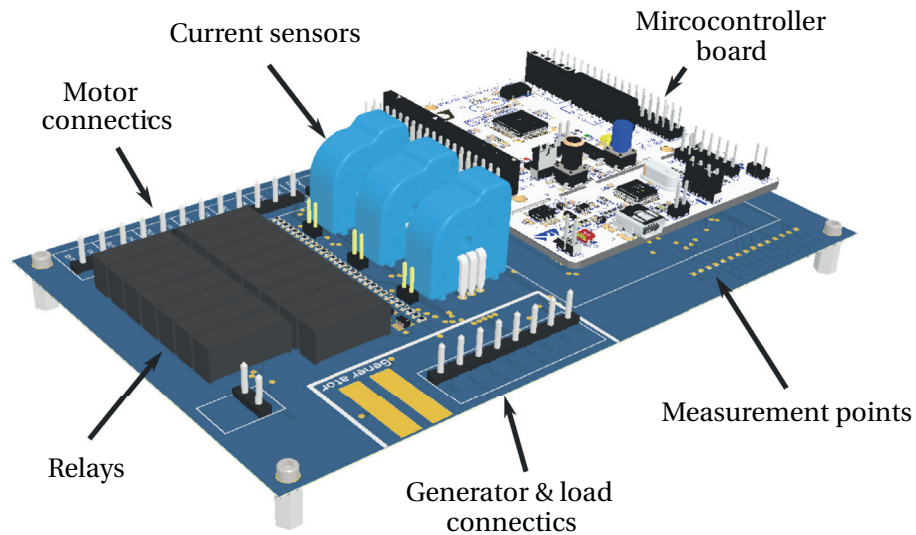


Figure 6.14 – Relay prototype board

In order to load the motor, it is coupled to a generator, which is connected to variable resistors. When the motor drives the generator, current flows through the variable resistors and a counter torque is created. Note that the smallest resistance generates the highest counter torque.

Finally, the bridge controlled by a micro-controller is supplied by a DC power supply. The signal coming out from the bridge pass through a relay board that configures each coil and phase according to the wanted configuration. These relays are controlled by the micro-controller.

6.7.1 Series to parallel reconfiguration

Following the discussed algorithm in order to change the winding reconfiguration from series to parallel reconfiguration, measurements are performed on a prototype in order to confront the simulated results and prove its feasibility. From its start, as the motor accelerates the required current decreases due to the increase of the back-emf magnitude. Then, as soon as the current reaches the reconfiguration criterion ($\frac{1}{2}$ of its maximum value) the reconfiguration starts. Due to the apparition of the current limitation in step 2, a PWM appears. Finally as soon as the step 3 is done the current is limited to its maximum. The variation of the current during the winding reconfiguration is shown in fig. 6.15

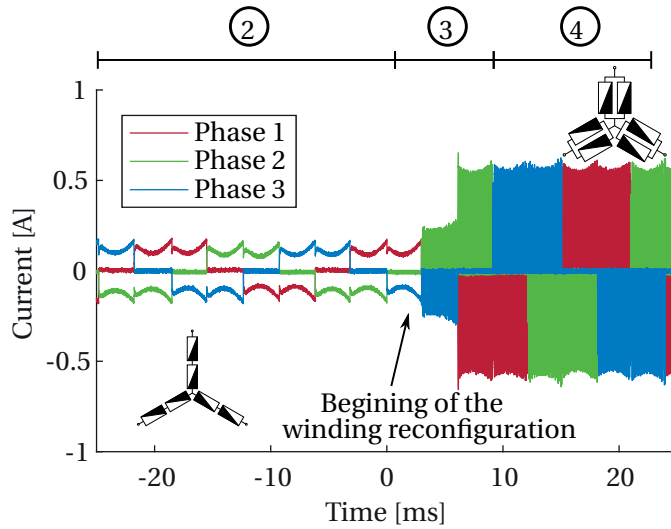


Figure 6.15 – Evolution of the measured current during the winding reconfiguration

The details of the current limitation can be seen by analysing phase 2. As the winding reconfiguration starts when this phase is floating, there is no current flowing through this phase and as a consequence this phase plays no role for the torque (trigger 1). Then, when this phase is reconfigured the current is limited to half of its maximum in order to prevent torque jerks (trigger 2). Phase 3 is floating and is reconfigured. Finally, the current is once again maximum in order to have the maximum torque and the last phase can be reconfigured (trigger 3).

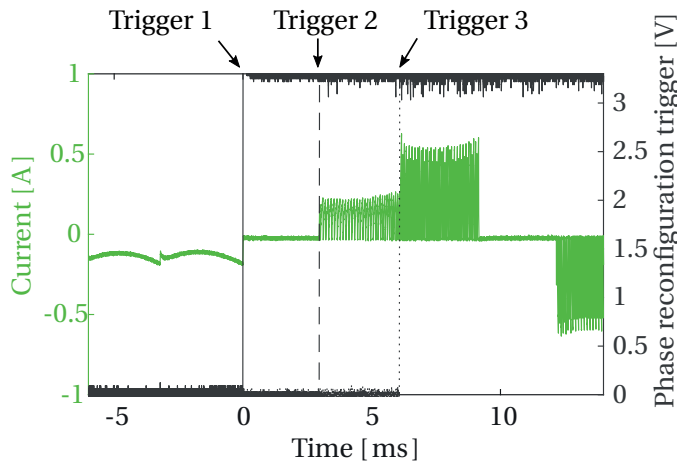


Figure 6.16 – Evolution of the measured phase 2 current during the winding reconfiguration

6.7.2 Star to delta reconfiguration

For star to delta reconfiguration, the criterion to start the winding reconfiguration occurs when the line current decreases because of the increase of back-emf and reaches $\frac{1}{\sqrt{3}}$ of its maximum value as discussed in section 6.2. The evolution of the current during the entire

winding reconfiguration from star to delta is presented in fig. 6.17.

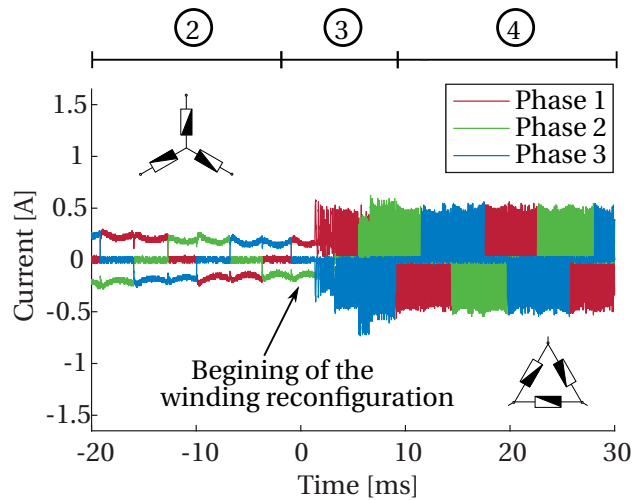


Figure 6.17 – Evolution of the measured phase 2 current during the winding reconfiguration

From the command strategy explained in section 6.6, the winding reconfiguration from star to delta while avoiding torque jerk is divided into 8 steps. Fig. 6.18 dissects the current signal for phase 2 and 3.

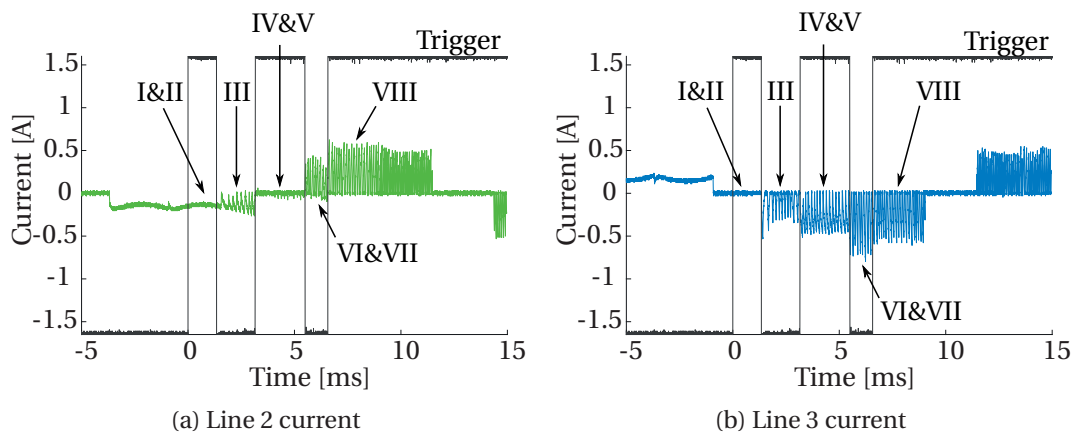


Figure 6.18 – Measured currents of phase 2 and 3 during the winding reconfiguration

As shown in fig. 6.18a, the reconfiguration occurs when the line 2 is connected to the ground. This means that the current is negative for phase 2 and by extension for line 2. During this time phase 3 is reconfigured because no current flows through it as shown in fig. 6.18b. When the winding reconfiguration reaches step III, the first current limitation occurs. Line 2 and 3 are connected to the ground. For this reason, currents are negative in these two lines. Due to the new current limitation, the PWM appears. During step IV and V, phase 2 is not supplied and is reconfigured. As this winding configuration is similar in terms of back-emf to the one when the winding is completely in delta configuration, the PWM reappears to control the

current. At this time, the amplitude of the back-emf phase-phase decreases by $\frac{1}{\sqrt{3}}$. During step VI and VII, the current is limited by a factor of $\frac{1}{\sqrt{3}}$ for phase 2 and 3 as shown for instance for line 2 in fig. 6.18a. Note that the current flowing in line 3 is the sum of the current flowing in all other phases. For this reason its value is greater than the limitation as shown in fig. 6.18b. When the reconfiguration reaches the last step, the current is released to its maximum and the maximum torque available is provided for the given winding configuration.

6.8 Modification of the motor dynamic

The reconfiguration of the winding modifies the motor intrinsic characteristic. In other terms the torque and speed limitations are changed. As a result, a torque boost or a speed boost can be achieved, which modifies the motor dynamic. The relation between the angular acceleration of the rotor and the torque is given by eq. (6.14).

$$\sum M = J \cdot \ddot{\varphi} \quad (6.14)$$

All the different torques present in the system can be developed as shown in eq. (6.15)

$$\underbrace{\sum_{i=1}^k I_i \frac{d\Psi_i(\varphi)}{d\varphi}}_{\text{EM}} + \underbrace{\sum_{i=1}^k \sum_{j=1}^k \frac{1}{2} I_i I_j \frac{dL_{ij}(\varphi)}{d\varphi}}_{\text{reluctant}} + \underbrace{\frac{1}{2} \Theta_e^2 \frac{d\Lambda_e(\varphi)}{d\varphi}}_{\text{cogging}} - \underbrace{M_{\text{fr}} \cdot \text{sign}(\Omega) - \beta\Omega + M_{\text{ext}}}_{\text{friction}} = J \cdot \ddot{\varphi} \quad (6.15)$$

where $k = 3$ for a three phase motor.

The first term M_{EM} is the electromotive torque generated by the interaction between the magnet of the rotor and the magnetic field. The second and third parts are the reluctant and cogging torque. Depending on the type of motor used, a variation of the magnetic path that can occur while the rotor is rotating. This can be due to salient poles for example. The second term depends on the excitation condition and the the third term depends on the magnetic path between the magnet and the rotor and the stator yoke. For slotless brushless DC motor these parts are not considered. Then there is the dry friction torque that is opposed to the rotation of the rotor. The first term is the friction force and the second one is the viscous force that depends on the speed of the rotor. Finally, the last term depends of an external applied torque. Note that if the latter is opposed to the rotor rotation, this torque becomes negative. As a result eq. (6.15) for slotless brushless DC motor is simplified as:

$$M_{\text{EM}} - M_{\text{fr}} \cdot \text{sign}(\Omega) - \beta\Omega + M_{\text{ext}} = J \cdot \ddot{\varphi} \quad (6.16)$$

A winding reconfiguration from star to delta connection is then considered. The star configuration has a higher torque constant than the delta connection. This means that by using the star configuration when the motor starts, the initial torque and the initial acceleration are higher. As the motor turns faster, the electromagnetic torque decreases as the current decreases as well

6.9. Experimental verification of the motor characteristic extension

due to the increase of the back-emf. As a result, when the winding reconfiguration criterion is reached the winding reconfiguration can occur. From there, the motor acceleration is reduced due to the fact that the maximum possible torque in the new configuration is lower as shown in fig. 6.19. Here, three scenarios are compared: when the winding stays in star configuration, when the winding stays in delta configuration and finally when winding reconfiguration is used. As expected, the maximum speed is reached faster (0.38 second) than if no winding reconfiguration were used (0.58 second). Furthermore, the maximum speed is lower for star configuration than delta configuration due to a higher torque constant.

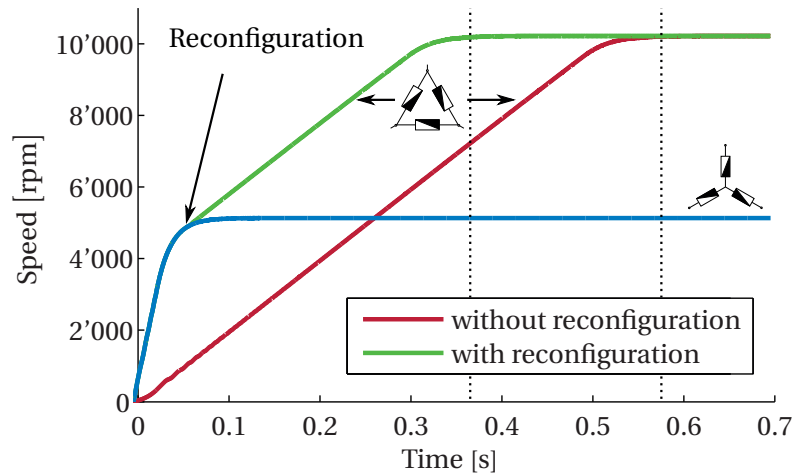


Figure 6.19 – Speed comparison with or without reconfiguration

6.9 Experimental verification of the motor characteristic extension

The winding reconfiguration increases the motor intrinsic characteristic. To highlight the theory developed in this study a torque sequence will be applied as shown in fig. 6.20 and two different scenarios will be used to illustrate it. The idea is to demonstrate that either a higher torque boost and a greater maximum speed are accessible using winding reconfiguration than if only one winding configuration were used.

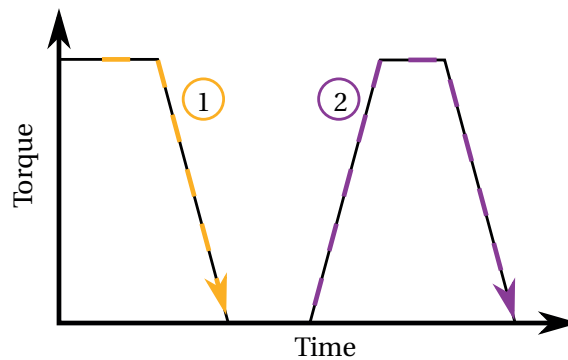


Figure 6.20 – Speed comparison with or without reconfiguration

Firstly a high external torque is applied to the motor. Then, the torque is slowly removed. Finally the same torque is reapplied and removed.

1. The first scenario demonstrates that a higher initial torque can be available when the motor starts together with a higher maximum speed while using the winding reconfiguration. This scenario includes only two winding reconfigurations: one when the motor is accelerating and one when the motor is decelerating. The evolution of the torque-speed is reported in fig. 6.21 where the lines are the theoretical torque-speed characteristics and the crosses are the measured torque and speed. Each color represents a winding configuration.

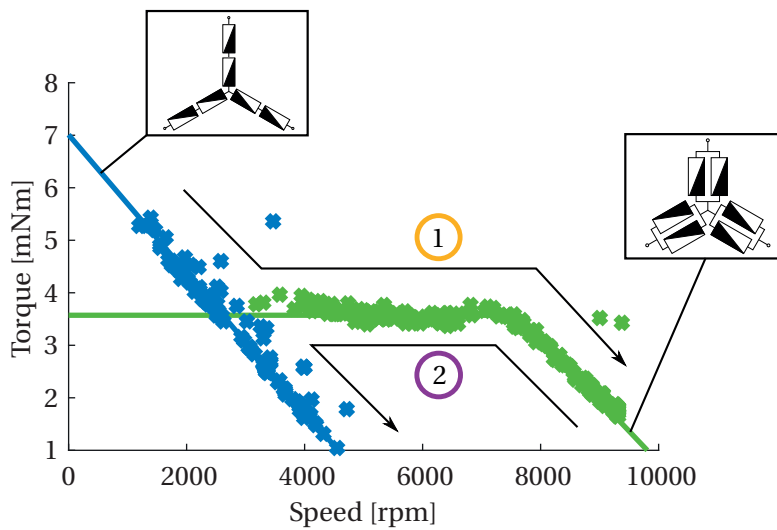


Figure 6.21 – Torque-speed characteristics with and without winding reconfiguration

In the beginning the motor is in star-series configuration (blue). When the winding reconfiguration criterion is reached as discussed in section 6.2, the winding is reconfigured into star-parallel configuration (green). The intrinsic characteristic is divided by two. The motor reaches its maximum speed in this new winding configuration. Then, a torque is reapplied to the motor (2). As the torque increases, the motor slows down until it reaches the same reconfiguration point. After the winding reconfiguration, the torque continues to increase. When the torque decreases once again, this time there is no winding reconfiguration and a new maximum speed is reached. As expected, this new maximum speed is half of the previous one when the motor was in star-parallel configuration.

2. In the second scenario, there is no restriction in the number of times that the winding reconfiguration is used. Whenever the winding reconfiguration criteria meet the requirement discussed in section 6.2, the winding is reconfigured. The new result is reported in fig. 6.22. Once again, each color represents a winding configuration. In blue is the star-series configuration and in green is the star-parallel configuration.

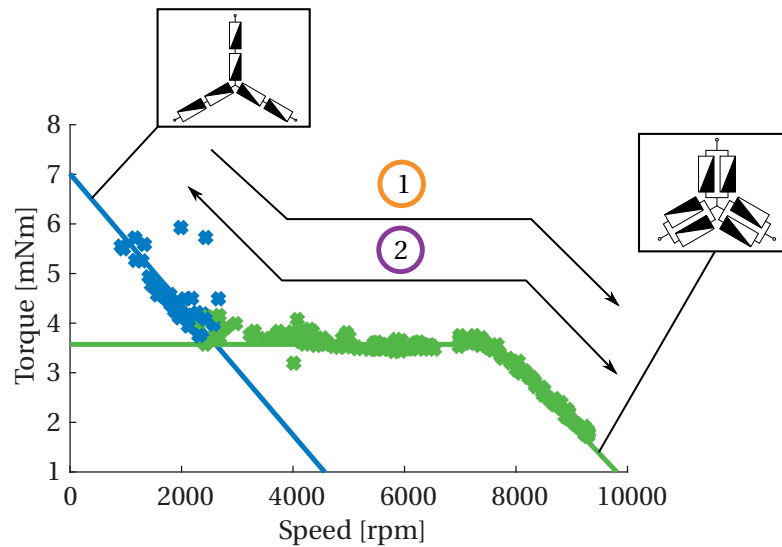


Figure 6.22 – Torque-speed characteristic with winding reconfiguration

When the applied torque is removed (1), the torque decreases. When the winding reconfiguration requirement is met, the winding is reconfigured to star-parallel configuration and a maximum speed is reached. Whenever a new torque is applied and removed, the same maximum speed is reached. When the torque increases, the winding is reconfigured in order to produce a higher torque than if the motor was only in star-delta configuration

6.10 Conclusion

The modification of the motor intrinsic characteristic can be subject to torque jerks during the reconfiguration process. They come from phase current variations when the phases are reconnected. Usually, these variations are small when the inductance of the motor is large. However, when the phase inductance is small, its current varies faster due to a small time constant. In order to avoid torque jerks in such situation, novel control methodologies have been presented for winding reconfiguration from series to parallel when the winding is in star configuration and for star to delta.

This new control is based on a fine control of the current amplitude and of the commutation angle under a block commutation. When a phase is not supplied, it does not play any role in the torque generation because no current flows through it. As a consequence the winding reconfiguration from series to parallel is straightforward. However, issues appear during star to delta reconfiguration because the current always flows in all phases when the winding is in delta connection. The developed control strategy guarantees a smooth torque transition even in such condition. The time available to reconfigure the motor diminishes with the rotor speed. Indeed, if the switch takes too long to turn on or off, short circuits or torque jerk can

Chapter 6. Dynamic winding reconfiguration

occur.

Finally, using winding reconfiguration improves the motor dynamic by offering a torque or a speed boost. A higher torque available when the motor starts gives a higher initial angular acceleration. This allows the motor to reach its maximum speed faster. Furthermore, the modification of the motor intrinsic characteristic improves the motor dynamic. In changing the torque and speed constant, a torque or speed boost is possible. Having a higher initial torque results in a greater initial acceleration. The maximum speed is reached faster. For example, using star to delta reconfiguration allows the motor to reach its maximum speed 34% faster than if the winding remains in delta configuration only.

Publications related to this chapter:

- F. Copt, D. Martins Araujo, C. Koechli and Y. Perriard, Dynamic Winding Reconfiguration of a Brushless DC Motor, 2017 IEEE International Electric Machines and Drives Conference (IEMDC), Miami, FL, USA, May 21-24, 2017
- F. Copt, D. Martins Araujo, C. Koechli and Y. Perriard, Current control strategy for dynamic winding reconfiguration of a brushless DC motor, 2017 IEEE Energy Conversion Congress and Exposition (ECCE), Cincinnati, OH, USA, 1-5 Oct. 2017

7 Conclusion and perspectives

In this thesis, the integration of a winding reconfiguration system has been investigated in order to increase the limited intrinsic motor characteristic. Usually, when a larger operating range is required, the drive system is oversized. In order to solve this issue, different aspects have been explored.

The motor phases are often made of several coils or groups of coils, which can be connected together either in series or in parallel. If the parallel coil groups do not have identical back-emf, circulating currents may appear. For this reason, the distribution of the winding has been investigated in order to reduce this effect. It has been shown that they can easily be reduced without necessarily adding more complexity.

The reconfiguration method has been investigated as well, and switches are needed to achieve this. Using transistors may have appeared to be the most appropriate solution because of their size and their ease of manipulation. However, as floating voltages are present in the electric circuit, relays have been chosen to reconfigure the electrical connections between the coils. As they are sizeable and can not simply be used as an integrated solution, its subfamily of MEMS relay has been favored. This family includes numerous possible technological actuation schemes. Here, the electrostatic one was chosen due to its low power consumption and its tolerance to the targeted environment.

With regards to the manufacturing steps, the relay has been designed. Because of the micro-fabrication technique, several dimensions can be subject to modification. For this reason, several influences have been discussed. Furthermore, the presented design has proposed an approach that guaranteed the contact surface flatness and a sufficient force to have a small contact resistance. The manufacturing and the tests performed have validated the feasibility of the presented process flow and the proposed design methodology.

Once the relay has been manufactured, its control has been analysed. When it comes to permanent magnet motors having a small inductance, fast current variations imply torque jerks. This phenomenon are not acceptable in specific applications such as surgical or dental

ones. Consequently, a control strategy has been proposed that suppresses these torque jerks during the winding reconfiguration. Finally, it has been shown that the proposed winding reconfiguration methods improved the motor dynamic by offering a torque or speed boost. Measurements performed on a prototype have shown that the maximum speed is reached in 34% less time while using the torque boost.

7.1 Original contributions

The research conducted throughout this thesis links different separated domains such as the motor and the microfabrication. The main contributions are summarized below.

- *Circulating current for different winding organizations*

Depending on the winding geometrical distribution, circulating currents between the conductors may appear. Usually these currents are small enough that they can be neglected, or the turns are twisted in order to reduce them. When it comes to winding reconfiguration, turns are grouped together to create a coil and are connected according to the desired intrinsic characteristic. Depending on how these turns are grouped, circulating currents may become significant especially when it comes to emergent winding technologies such as flexPCB where the turns can not be twisted. The significance of the presented analysis lies in the study of the spatial distribution of the grouped turns and its consequence on circulating currents between the parallel conductors. It has been shown that the circulating currents can be drastically reduced without adding too much complexity to the winding fabrication: this can be an asset for future winding designs.

- *Methodology to design a MEMS relay with the aim to integrate it inside a motor*

The reconfiguration of the winding is performed through relays that will reshape the electrical connections between the coils. In order to design them to be manufactured in the clean room, a special methodology has been presented. As they will be used in a winding, their resistance shall be as small as possible in order to not reduce the motor's intrinsic characteristic and to add losses if its supply is limited. As the contact resistance is the biggest between all electrical resistances, two approaches are proposed to keep its value small. As this value is determined both by its contact surface and the contact force, a two spring system is used, which offers an increase of the contact force. However, this system has the drawback that the contact can be subject to deformation. The proposed model ensures the flatness of the contact based on the variation of the flexural rigidity of the contact when the relay is actuated. Furthermore, the proposed methodology explores the limitation of the manufacturing methods and their influences on the relay behaviour as well. Finally, the environment plays an important role in the requirements of the relay. For this reason, resonant frequencies should be taken care of. Within this framework, the proposed methodologies gives the necessary tools to manufacture a MEMS relay, which will be integrated inside a requiring environment.

- *Process flow for manufacturing a MEMs relay*

In order to manufacture the relay, a process was developed and optimized. This process confirms the feasibility of the design approach based on a variation of the flexural rigidity presented before without adding much complexity in the process flow design. Furthermore, the different tests performed on the prototypes confirm the theoretical design. Finally, although a manipulation error has reduced the success rate of the fabrication, the proposed process is stable and can be easily re-used or adapted for different relay shapes.

- *Winding reconfiguration without torque jerk*

The winding reconfiguration on slotless brushless DC motor has never been analysed in the literature. This type of motor has a very small inductance and it is subject to fast current variations which will cause torque jerks. For surgical or dental applications, these jerks are not acceptable. The proposed control guarantees a smooth transition from one configuration to another (series/parallel reconfiguration or star/delta reconfiguration) when the motor is block controlled.

7.2 Outlook and perspectives

Considering the work done through this thesis, research directions or improvements can be suggested.

- *Lifespan of the relay*

One of the key aspect in adding new components in a system is their lifespan. Due to the impact of the contact, the latter can degrade, which can lead to failure. The key aspect to investigate is the life time of the contact itself. Furthermore, as the electrode will be placed one above the other with an intermediate dielectric layer, the wear of this layer over time should be analyzed as well. Depending on the result obtained, optimization should be performed to improve it.

- *Shape optimization*

The designed relays that have been built with the designed process flow have confirmed the feasibility of the approach. Its shape should now be optimized with the aim to reduce its size and integrate it in different motor sizes.

- *Adding different sensors*

Now that the winding reconfiguration can be performed using MEMS relays, the next step could be to add intelligence to the winding so that it could monitor itself.

The main limitation of the motor is thermal. It is mainly due to the Joule losses of the winding for motor of the studied size. In real life scenario, the motor is used at different speeds and different loads during variable periods. As the cooling is hard

to estimate, a safe margin is usually taken and the drive system is oversized for the client. Consequently, by integrating a thermal sensor directly inside the winding, a finer thermal control can be done.

By using auxiliary turns, it is possible to measure the magnetic field. Consequently, it becomes possible to determine the rotor position, which could be used as an alternative to Hall sensors.

- *Study of the different working motor mode*

The control performed in the thesis targets only the motor working in motor mode. However, various aspects can be investigated. For example, the active braking or the generator mode.

If the motor is in speed boost and the winding unexpectedly reconfigures, the back-emf voltage becomes too high compared to the bridge voltage. Consequently, the control is lost and the diodes of the bridge start conducting until the working point reaches the new characteristics. An extensive study of this behaviour and its consequence on the circuit should be investigated. Furthermore, the possibility to actively brake the motor using the winding reconfiguration should be conducted as well.

If the winding reconfiguration is used in generator mode, different voltages could be produced.

- *Voltage adaptation*

From an industrial point of view, depending on the customer voltage source, motor manufacturers have to propose motors composed of different windings in order to offer the same motor characteristic. Instead of manufacturing different winding, the windings reconfiguration can be used.

A Vector potential

The brushless DC motor is include of magnetic part and an electric part. In order to link them, Maxwell equations can be used. In quasi-static these equations are:

$$\nabla \cdot \vec{D} = \rho \quad (\text{A.1})$$

$$\nabla \times \vec{E} = \frac{\partial \vec{B}}{\partial t} \quad (\text{A.2})$$

$$\nabla \cdot \vec{B} = 0 \quad (\text{A.3})$$

$$\nabla \times \vec{H} = \mu_0 \vec{J} \quad (\text{A.4})$$

In order to evaluate the induction in the air gap, usually a potential vector \vec{A} is introduced. The latter is defined as follows:

$$\nabla \times \vec{A} = \vec{B} \quad (\text{A.5})$$

A vector field is fully defined by a curl and a divergence. In order to avoid an infinity of solution and simplify the futur equations, the Coulomb gauge is chosen as a complement of eq. (A.5).

$$\nabla \cdot \vec{A} = 0 \quad (\text{A.6})$$

By substituting eq. (A.5) in eq. (A.4):

$$\nabla \times (\nabla \times \vec{A}) = \mu_0 \vec{J} \quad (\text{A.7})$$

$$\nabla (\nabla \cdot \vec{A}) - \Delta \vec{A} = \mu_0 \vec{J} \quad (\text{A.8})$$

Thanks to the Coulomb law eq. (A.8) is simplified.

$$\Delta \vec{A} = -\mu_0 \vec{J} \quad (\text{A.9})$$

Appendix A. Vector potential

In a cylindrical frame, the potential vector is expressed as shown in eq. (A.10).

$$\Delta \vec{A} = \frac{\partial^2 \vec{A}}{\partial r^2} + \frac{1}{r} \frac{\partial \vec{A}}{\partial r} + \frac{1}{r^2} \frac{\partial^2 \vec{A}}{\partial \varphi^2} = -\mu_0 \vec{J} \quad (\text{A.10})$$

In this study, only the influence of the magnet is considered. As a consequence eq. (A.10) is simplified.

$$\Delta \vec{A} = \frac{\partial^2 \vec{A}}{\partial r^2} + \frac{1}{r} \frac{\partial \vec{A}}{\partial r} + \frac{1}{r^2} \frac{\partial^2 \vec{A}}{\partial \varphi^2} = 0 \quad (\text{A.11})$$

Due to the cylinder symmetry and that the leakage flux and the fringes are not considered \vec{A} can be reduced to the z component.

$$\Delta A_z = \frac{\partial^2 A_z}{\partial r^2} + \frac{1}{r} \frac{\partial A_z}{\partial r} + \frac{1}{r^2} \frac{\partial^2 A_z}{\partial \varphi^2} = 0 \quad (\text{A.12})$$

Establishing that the solution is the product of two separable variable such as:

$$A_z(r, \varphi) = f(r) \cdot g(\varphi) \quad (\text{A.13})$$

This mean that:

$$\frac{\partial^2 A_z}{\partial r^2} = g(\varphi) \frac{\partial f}{\partial r} = f' g \quad (\text{A.14a})$$

$$\frac{\partial^2 A_z}{\partial r^2} = g(\varphi) \frac{\partial^2 f(r)}{\partial r^2} = f'' g \quad (\text{A.14b})$$

$$\frac{\partial^2 A_z}{\partial \varphi^2} = f(r) \frac{\partial^2 g(\varphi)}{\partial \varphi^2} = f g'' \quad (\text{A.14c})$$

Hence:

$$r^2 \frac{f''}{f} + r \frac{f'}{f} = -\frac{g'}{g} \quad (\text{A.15})$$

As this two equation have to be equal to each other. A constant n is add:

$$r^2 \frac{f''}{f} + r \frac{f'}{f} = -\frac{g'}{g} = n^2 \quad (\text{A.16})$$

so:

$$r^2 f'' + r f' - n^2 f = 0 \quad (\text{A.17a})$$

$$g'' + n^2 g = 0 \quad (\text{A.17b})$$

The solution is:

$$f(r) = a_n r^n + b_n r^{-n} \quad (\text{A.18a})$$

$$g(\varphi) = c_n \cos(n\varphi) + d_n \sin(n\varphi) \quad (\text{A.18b})$$

the solution for the potential vector is:

$$A_z(r, \varphi) = \sum_{n=1}^{\infty} f(r) \cdot g(\varphi) = \sum_{n=1}^{\infty} (a_n r^n + b_n r^{-n}) \cdot (c_n \cos(n\varphi) + d_n \sin(n\varphi)) \quad (\text{A.19})$$

B Evaluation of the vector potential in the motor

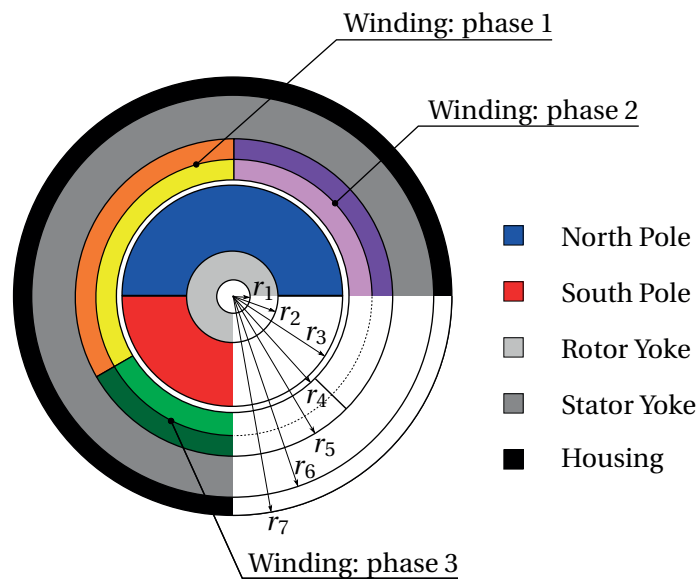


Figure B.1 – Internal radius parametrization

From the vector potential:

$$A_{z_i}(r, \varphi) = (e_i r + f_i r^{-1}) \cdot \sin(\varphi) \quad (\text{B.1})$$

where i stands for the domain in which the vector potential is evaluated.

e_i and f_i can be found by applying the limit conditions between each domain and by solving the resulting equations system. Indeed, by using eq. (B.3) the continuity of the magnetic flux and the magnetic flux strength is guaranty [92].

Appendix B. Evaluation of the vector potential in the motor

$$\vec{n} \cdot (\vec{B}_2 - \vec{B}_1) = 0 \quad (\text{B.2})$$

$$\vec{n} \times (\vec{H}_2 - \vec{H}_1) = \vec{I}_s \quad (\text{B.3})$$

where \vec{n} is the surface normal vector and \vec{I}_s the surface current density, 1 and 2 stand for domain 1 and domain 2

- Eq. (B.2) indicates that the focus is on the radial component. The relationship between the potential vector and the induction in cylindrical coordinate is:

$$\vec{n} \cdot \vec{B} = \frac{1}{r} \frac{\partial A_z}{\partial \varphi} \quad (\text{B.4})$$

- For the second condition, at the magnet border and by using eq. (B.3):

$$\vec{n} \times \left(\left. \frac{\vec{B}}{\mu_0 \mu_r} \right|_2 - \left. \frac{\vec{B}}{\mu_0 \mu_{dr}} \right|_1 \right) + \vec{n} \times \left(\frac{\vec{B}_0}{\mu_0 \mu_{dr}} \right) = 0 \quad (\text{B.5})$$

Therefore:

$$\vec{I}_s = -\vec{n} \times \left(\frac{\vec{B}_0}{\mu_0 \mu_{dr}} \right) \quad (\text{B.6})$$

which gives for external surface when the magnet is diametrically magnetized

$$\vec{I}_{s\text{external}} = -\frac{1}{\mu_0 \mu_{dr}} \begin{bmatrix} \cos(\varphi) \\ \sin(\varphi) \\ 0 \end{bmatrix} \times \begin{bmatrix} B_0 \\ 0 \\ 0 \end{bmatrix} = \begin{bmatrix} 0 \\ 0 \\ \frac{B_0}{\mu_0 \mu_{dr}} \sin(\varphi) \end{bmatrix} \quad (\text{B.7})$$

and for internal surface

$$\vec{I}_{s\text{internal}} = -\vec{I}_{s\text{external}} \quad (\text{B.8})$$

Otherwise

$$\vec{I}_s = 0 \quad (\text{B.9})$$

C Process Flow

Semestral Project Master Project Thesis Other

Electrostatic MEMs relay for power application



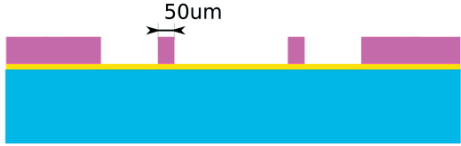
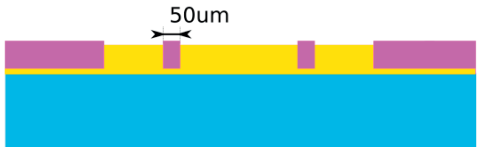





Description











In my thesis the fabrication of an electrostatic mems relay is needed. This switch have to handle **1.56A DC** with a conducting resistance smaller than **168 mΩ**.










| Technologies used | | | |
|---|-------------------------|--------------------|---------------------------------------|
| Direct writting, Lift-off, Dry etching, Wet etching, PECVD, sputtering, Electro-Plating, Thermal oxidation, Wafer Bonding, Grinding, CMP, Thermocompression | | | |
| Photolith masks | | | |
| Mask # | Critical Dimension [um] | Critical Alignment | Remarks |
| 1 | 200 | First Mask | Electrodes and tracks |
| 2 | 50 | | Au remove bottom wafer |
| 3 | 40 | | Au ring remover |
| 4 | 20 | | SiO2 bottom wafer |
| 5 | 20 | | Pt mask |
| 6 | 20 | | Au increase |
| 7 | 20 | First Mask | Partial dry etch mask for structuring |
| 8 | 20 | | Au contact and electrodes structuring |
| 9 | 20 | | Au etch |
| 10 | 20 | | Full dry etch mask for structuring |
| 11 | 1000 | | Relay structuring |
| Substrate Type | | | |
| | | | |










For reading purpose, vertical dimensions are enlarged because horizontal dimensions are too large.











Process outline








| Step | Process description | Cross-section after process | Remarks |
|------|--|--|------------------------------------|
| 01 | Substrate: <i>Borofloat</i> Process: <i>Piranha</i> Machine: <i>UFT Piranha</i> |  | Clean the surface |
| 02 | Process: <i>Evaporation Ti/Au</i> Machine: <i>EVA760</i> Thickness: <ul style="list-style-type: none"> • 20 nm Ti • 500 nm Au • 20 nm Ti |  | |
| 03 | Process: <i>Lithography</i> PR: <i>AZ9260</i> Machine: <i>ACS200+MA6</i> Thickness: 8 μm PR Mask: <i>1</i> |  | Topography: 0 um No dehydration |
| 04 | Process: <i>Electroplating Au</i> Machine: <i>CSEM</i> Thickness: 5 μm Au |  | |
| 05 | Process: <i>Resist strip</i> Machine: <i>Coillard Photo</i> |  | |
| 06 | Process: <i>Lithography</i> Machine: <i>ACS200+MA6</i> PR: <i>AZ9260</i> Thickness: 8 μm PR Mask: <i>2</i> |  | Topography: 3um |
| 07 | Process : <i>Reflow</i> 2min @130°C |  | |
| 08 | Process: <i>Dry Etch Ti/Au/Ti</i> Machine: <i>IBE</i> |  | |
| 09 | Process: <i>Resist strip</i> |  | |

| | | | |
|----|---|--|-------------------|
| 10 | Process: <i>Lithography</i> Machine: <i>ACS200+MA6</i> PR: <i>AZ9260</i> Thickness: <i>8um PR</i> Mask: 3 |  | Ring etching |
| 11 | Process : <i>Wet Au etch</i> Machine : <i>Acid bench</i> |  | Ring etching |
| 12 | Process: <i>Resist strip</i> Machine: <i>Coillard Photo</i> |  | |
| 13 | Process: <i>Supttering</i> <i>Ti+SiO2</i> Machine: <i>Spider 600</i> Thickness: <i>20nm</i> <i>Ti+200nm SiO2</i> |  | |
| 14 | Process: <i>Lithography</i> PR: <i>AZ9260</i> Thickness: <i>8 μm PR</i> Machine: <i>ACS200+MA6</i> Mask: 4 |  | |
| 15 | Process: <i>Wet etch</i> Machine: <i>HF</i> |  | |
| 16 | Process: <i>Resist strip</i> Machine: <i>Coillard Photo</i> |  | |
| 17 | Process: <i>Lithography</i> PR: <i>AZ1515 + nLOR</i> Machine: <i>ACS200+ MA6</i> Thickness: <i>8μm PR</i> Mask: 5 |  | Topography: 5.8um |
| 18 | Process: <i>Evaporation Pt</i> Machine: <i>LAB600</i> Thickness: <i>100 nm Pt</i> |  | |
| 19 | Process: <i>Lift off</i> |  | |







| | | | |
|----|--|--|---|
| 20 | Process: <i>Lithography</i> Machine: <i>ACS200+MA6</i> PR: <i>AZ9260</i> Thickness: <i>8um PR</i> Mask: <i>6</i> |  | |
| 21 | Process: <i>Evaporation Ti/Au</i> Machine: <i>EVA760</i> Thickness: <ul style="list-style-type: none"> • <i>20 nm Ti</i> • <i>500 nm Au</i> |  | |
| 22 | Process: <i>Lift off</i> |  | |
| 23 | Substrate: <i>SOI</i> (<i>380x2x100</i>) Process: <i>Grinder</i> Machine: <i>DAG810</i> <ul style="list-style-type: none"> • <i>Front side: 8 μm</i> • <i>Back side: 48 μm</i> |  | Dimension to request: <u>Total thickness</u> 482 μm → 474 μm 474 μm → 426 μm |
| 24 | Process: <i>CMP</i> Machine: <i>Steag Mecapol</i> Thickness: <ul style="list-style-type: none"> • <i>Face 1: 5 μm</i> • <i>Face 2: 5 μm</i> |  | Dimension: 426 μm → 421 μm 421 μm → 416 μm |
| 25 | Process: <i>HF</i> Machine: <i>Plade oxyde</i> |  | Clean residual slurry |
| 26 | Process: <i>Oxidation SiO2</i> Machine: <i>RCA + Thermal oxidation</i> Thickness: <i>200nm</i> |  | To request |
| 27 | Process: <i>Lithography</i> PR: <i>AZ9221</i> Machine: <i>RiteTrack+MLA</i> Thickness: <i>2 μm PR</i> Mask: <i>7</i> |  | Topography: 0 um |
| 28 | Process: <i>Dry Etch SiO2</i> Machine: <i>SPTS</i> |  | |

| | | | |
|----|---|--|--|
| 29 | Process: <i>Resist strip</i> Machine: <i>Tepla</i> |  | |
| 30 | Process: <i>Wet Etch Si</i> Machine: <i>KOH</i> Depth: 13µm |  | Wet etch because slops are needed Ensure that K is well removed |
| 31 | Process: <i>Wet etch SiO2</i> Machine: <i>HF</i> |  | |
| 32 | Process: <i>Oxidation SiO2</i> Machine: <i>RCA + Thermal oxidation</i> Thickness: 500nm |  | |
| 33 | Process: <i>Evaporation Ti+Au + Ti</i> Machine: <i>EVA760</i> Thickness: <ul style="list-style-type: none"> • 20 nm Ti • 500 nm Au • 20nmTi |  | |
| 34 | Process: <i>Lithography</i> PR: <i>AZ9260</i> Machine: <i>RiteTrack+MA6</i> Thickness: 14µm Mask: 8 |  | |
| 35 | Process: <i>Electroplating Au</i> Machine: <i>CSEM</i> Thickness: 5 µm Au |  | Topography : 13 um |
| 36 | Process: <i>Resist strip</i> Machine: <i>Coillard Photo</i> |  | |
| 37 | Process: <i>Lithography</i> PR: <i>AZ9260</i> Machine: <i>ACS+MA6</i> Thickness: 14µm Mask: 9 |  | Topography : 13 um |

| | | | |
|----|--|--|------------------------|
| 38 | Process : <i>Reflow</i> 2min @ 130°C |  | |
| 39 | Process: <i>Dry etch Ti+Au + Ti</i> Machine: <i>IBE</i> |  | |
| 40 | Process: <i>Wet Etch SiO2</i> Machine: <i>BHF</i> |  | |
| 41 | Process: <i>Resist strip</i> Machine: <i>Coillard Photo</i> |  | |
| 42 | Process: <i>Lithography</i> PR: <i>AZ9260</i> Machine: <i>ACS+MA6</i> Thickness: <i>14µm</i> Mask: <i>3</i> |  | Removing the gold ring |
| 43 | Process : <i>Wet Au etch</i> Machine : <i>Acid bench</i> |  | |
| 44 | Process: <i>Resist strip</i> Machine: <i>Coillard Photo</i> |  | |
| 45 | Process: <i>Lithography</i> PR: <i>AZ9260</i> Machine: <i>ACS+MA6</i> Thickness: <i>14µm</i> Mask: <i>10</i> |  | Topography : 13.7 µm |
| 46 | Process: <i>Dry Etch Si</i> Machine: <i>AMS200</i> Depth: <i>87 µm</i> |  | |
| 47 | Process: <i>Dry Etch SiO2</i> Machine: <i>STPS</i> Depth: <i>2µm</i> |  | |

| | | | |
|----|--|--|---|
| 48 | Process: <i>Resist strip</i> Machine: <i>Coillard Photo</i> |  | |
| 49 | Process: <i>Thermopression</i> Machine: <i>CSEM</i> |  | Note: Two devices next to each other |
| 50 | Process: <i>Sputtering SiO2</i> Machine: <i>Spider</i> Thickness: <i>4 μm</i> |  | Note: 2.18 μm SiO2 BS etched during the upcoming Si etch |
| 51 | Process: <i>Lithography</i> PR: <i>AZ9221</i> Machine: <i>RiteTrack+MA6</i> Thickness: <i>8 μm</i> Mask: <i>11</i> |  | Topography : 0 μm |
| 52 | Process: <i>Wafer bond</i> Machine: <i>Nanoprint</i> |  | |
| 53 | Process: <i>Dry Etch SiO2</i> Machine: <i>SPTS</i> |  | |
| 54 | Process: <i>Dry Etch Si</i> Machine: <i>AMS200</i> |  | Note that in the schema the floating part are connected somewhere else which is not shown here due to the cut |

Legend:

- | | | |
|---|---|---|
|  Glass |  Photoresist |  Silicon |
|  Gold |  Carrier wafer |  Silicon Oxide |

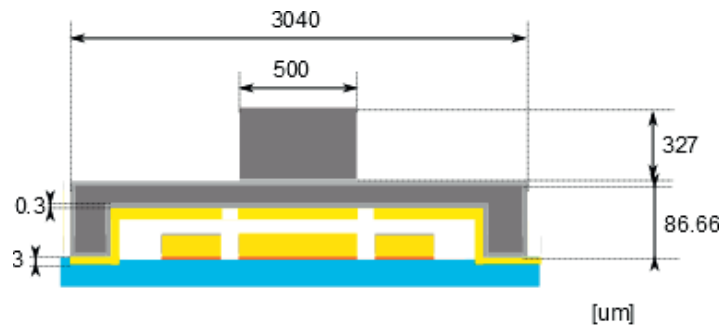


Fig 1: General dimension

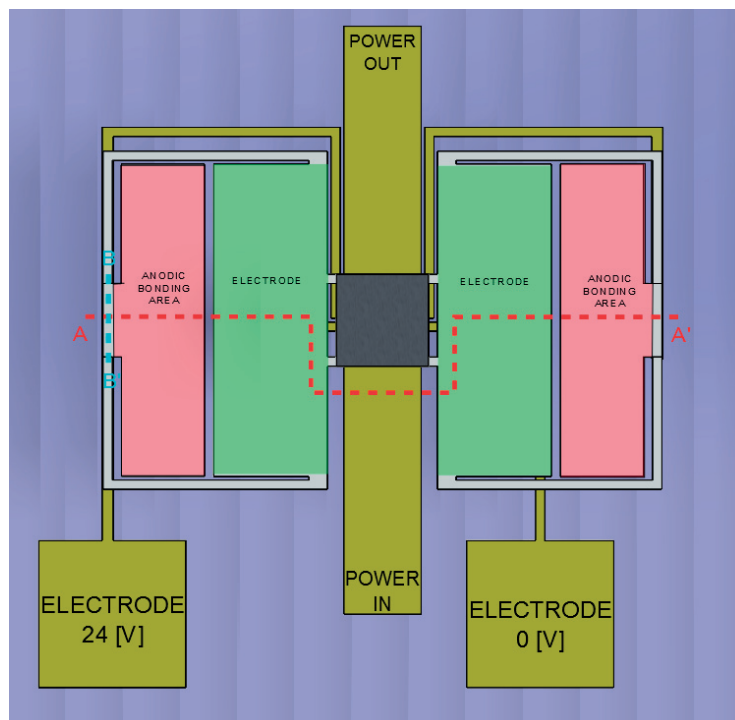


Fig 2: Relay

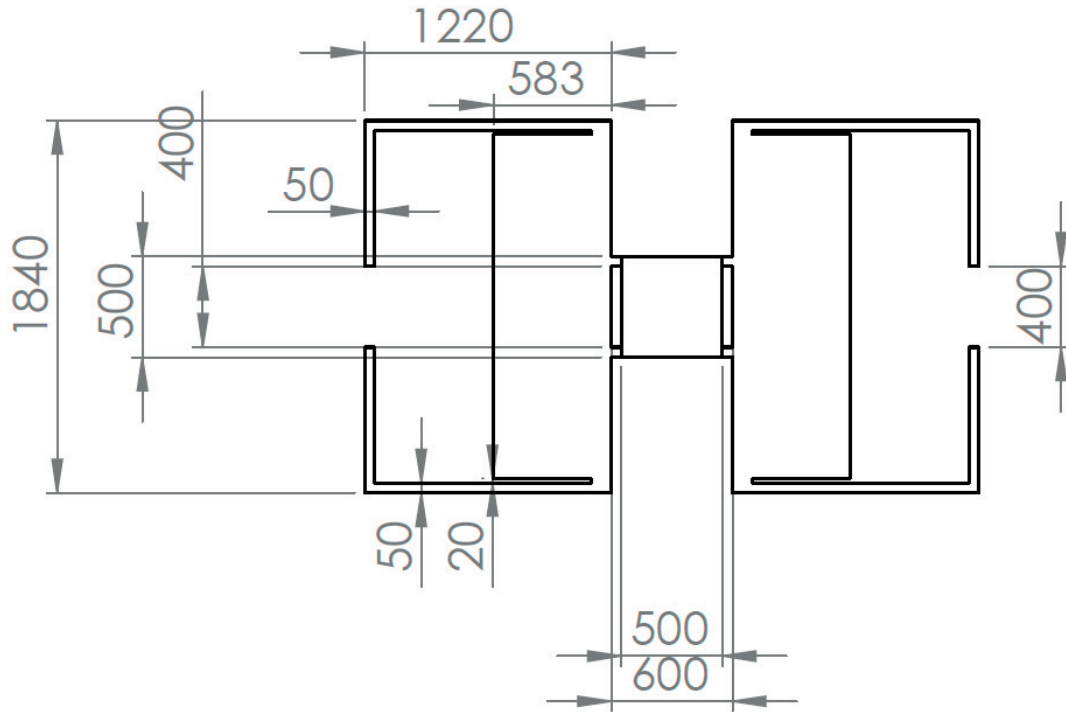


Fig 3: Design of the relay basic dimen

D Wafer carrier process flow

Lab : IMT-LAI
Operator Name : **F. Copt**
Supervisor Name : Y. Perriard C. Koechli Y. Civet
Date of comitee :

Téléphone : +4121 693 54290
Office : MC A4 228
E-mail : florian.copt@epfl.ch



Semestral Project Master Project Thesis Other










Wafer carrier

Description

Wafer carrier used for wafer bonding and future dry etch with AMS200 (Z2).

| Technologies used | | | |
|---|-------------------------|--------------------|---------|
| Lithography, sputtering, positive resist, Dry etching, Wet etching. | | | |
| Photolith masks | | | |
| Mask # | Critical Dimension [um] | Critical Alignment | Remarks |
| 1 | 200 | First Mask | |
| Substrate Type | | | |
| <i>100p/DS/ 0.1-0.5 TTV2 wet oxide 2um</i> | | | |

Process outline

| Step | Process description | Cross-section after process | Remarks |
|------|--|--|---------------------|
| 01 | Process: <i>Piranha</i> Machine: <i>UFT Piranha</i> |  | Clean the surface |
| 02 | Process: <i>Sputtering Cr/Al</i> Machine: <i>DP650</i> Thickness: <ul style="list-style-type: none"> • 20 nm Cr • 2 um Al |  | |
| 03 | Process: <i>Lithography</i> PR: <i>AZ9260</i> Machine: <i>ACS200+MA6</i> Thickness: 5 um PR Mask: <i>1</i> |  | Topography: 0 um |
| 04 | Process: <i>Post bake</i> Machine: <i>Oven</i> |  | Overnight at 85°C |
| 05 | Process: <i>Dry Etch SiO2</i> Machine: <i>SPTS</i> |  | Receipt: 3:1 |
| 06 | Process: <i>Dry Etch Si</i> Machine: <i>AMS200</i> Depth: Through-hole |  | Receipt: SOIACC++++ |
| 07 | Process: <i>Resist strip</i> Machine: <i>Coillard Photo</i> |  | |
| 08 | Process: <i>Wet etch</i> Machine: <i>Al etch</i> |  | |
| 09 | Process: <i>Wet etch</i> Machine: <i>BHF</i> |  | |

Legend:

| | | | |
|---|-------------|---|---------------|
|  | Photoresist |  | Silicon |
|  | Alu |  | Silicon Oxide |

Bibliography

- [1] IEEE Standard on Piezoelectricity. *ANSI/IEEE Std 176-1987*, pages 0_1–, 1988.
- [2] Thin film shape memory alloy actuated microrelay, March 2001.
- [3] Adhesive wafer bonding. *Journal of Applied Physics*, 99(3):031101, February 2006.
- [4] *Comprehensive Materials Processing*. Newnes, April 2014.
- [5] *High-power-density high-efficiency permanent magnet synchronous motor used for vehicle*. Google Patents, February 2015.
- [6] V. Agrawal. A latching MEMS relay for DC and RF applications. In *Proceedings of the 50th IEEE Holm Conference on Electrical Contacts and the 22nd International Conference on Electrical Contacts Electrical Contacts, 2004.*, pages 222–225, September 2004.
- [7] M. Aydin, Surong Huang, and T. A. Lipo. A new axial flux surface mounted permanent magnet machine capable of field control. In *Conference Record of the 2002 IEEE Industry Applications Conference. 37th IAS Annual Meeting (Cat. No.02CH37344)*, volume 2, pages 1250–1257 vol.2, October 2002.
- [8] D. Balma, A. Lamberti, S. L. Marasso, D. Perrone, M. Quaglio, G. Canavese, S. Bianco, and M. Cocuzza. Piezoelectrically actuated MEMS microswitches for high current applications. *Microelectronic Engineering*, 88(8):2208–2210, August 2011.
- [9] Allen Keith Bates, Nhan Xuan Bui, Reed Alan Hancock, and Daniel James Winarski. Dynamic reconfiguration-switching of windings in a brushless DC motor, March 2015. U.S. Classification 318/400.41, 318/496, 318/497; International Classification H02P25/18, H02P27/08, H02P6/08; Cooperative Classification H02P27/08, H02P25/18.
- [10] A. Berthold, B. Jakoby, and M. J. Vellekoop. Wafer-to-wafer fusion bonding of oxidized silicon to silicon at low temperatures. *Sensors and Actuators A: Physical*, 68(1):410–413, June 1998.
- [11] Bharat Bhushan. *Springer Handbook of Nanotechnology*. Springer Science & Business Media, April 2010. Google-Books-ID: me1grr_pobMC.

Bibliography

- [12] Ramon O. Caceres and Ivo Barbi. A boost DC-AC converter: analysis, design, and experimentation. *IEEE transactions on power electronics*, 14(1):134–141, 1999.
- [13] F. Caricchi, F. Crescimbin, F. Mezzetti, and E. Santini. Multistage axial-flux PM machine for wheel direct drive. *IEEE Transactions on Industry Applications*, 32(4):882–888, July 1996.
- [14] S.-K. Changchien, T.-J. Liang, J.-F. Chen, and L.-S. Yang. Step-up DC–DC converter by coupled inductor and voltage-lift technique. *IET power electronics*, 3(3):369–378, 2010.
- [15] Y. Chen, L. Kong, and W. Zhong. Finite element analysis of interior composite-rotor controllable flux permanent magnet synchronous machine. In *2009 International Conference on Electrical Machines and Systems*, pages 1–4, November 2009.
- [16] Il-Joo Cho, Taeksang Song, Sang-Hyun Baek, and Euisik Yoon. A low-voltage and low-power RF MEMS series and shunt switches actuated by combination of electromagnetic and electrostatic forces. *IEEE Transactions on Microwave Theory and Techniques*, 53(7):2450–2457, July 2005.
- [17] Michael B. Cohn, Kaosio Saechao, Michael Whitlock, Daniel Brenman, Wallace T. Tang, and Robert M. Proie. RF MEMS switches for wide I/O data bus applications. In *Test Conference (ITC), 2013 IEEE International*, pages 1–8. IEEE, 2013.
- [18] R. Coratger, C. Girardin, R. Pechou, F. Ajustron, and J. Beauvillain. Determination of the electron mean free path in the 1–1.8 eV energy range in thin gold layers using ballistic electron emission microscopy. *The European Physical Journal - Applied Physics*, 5(3):237–242, March 1999.
- [19] S. Day and T. Christenson. A High Aspect Ratio Microfabricated Reed Switch Capable of Hot Switching. In *2013 IEEE 59th Holm Conference on Electrical Contacts (Holm 2013)*, pages 1–8, September 2013.
- [20] M. J. DeBortoli, S. J. Salon, D. W. Burow, and C. J. Slavik. Effects of rotor eccentricity and parallel windings on induction machine behavior: a study using finite element analysis. *IEEE Transactions on Magnetics*, 29(2):1676–1682, March 1993.
- [21] B. Dehez, F. Baudart, M. Markovic, and Y. Perriard. Theoretical and Experimental Investigation of Flex-PCB Air-Gap Windings in Slotless BLDC Machines. *IEEE Transactions on Industry Applications*, 50(5):3153–3160, September 2014.
- [22] Michel Del Pedro and John Botsis. *Introduction à la mécanique des solides et des structures*. [Mécanique]. Presses Polytechniques et Universitaires Romandes, Lausanne, 3e édition revue et augmentée edition, 2012.
- [23] Ji Fan and Chuan Seng Tan. Low Temperature Wafer-Level Metal Thermo-Compression Bonding Technology for 3d Integration. *Metallurgy - Advances in Materials and Processes*, 2012.

-
- [24] Leslie A. Field and Richard S. Muller. Fusing silicon wafers with low melting temperature glass. *Sensors and Actuators A: Physical*, 23(1-3):935–938, 1990.
- [25] A. Florescu, O. Stocklosa, M. Teodorescu, C. Radoi, D. A. Stoichescu, and S. Rosu. The advantages, limitations and disadvantages of Z-source inverter. In *CAS 2010 Proceedings (International Semiconductor Conference)*, volume 02, pages 483–486, October 2010.
- [26] D. Fodorean, A. Djerdir, I. A. Viorel, and A. Miraoui. A Double Excited Synchronous Machine for Direct Drive Application #x2014;Design and Prototype Tests. *IEEE Transactions on Energy Conversion*, 22(3):656–665, September 2007.
- [27] A. Foggia, J. E. Torlay, C. Corenwinder, A. Audoli, and J. Herigault. Circulating current analysis in the parallel-connected windings of synchronous generators under abnormal operating conditions. In *Electric Machines and Drives, 1999. International Conference IEMD '99*, pages 634–636, May 1999.
- [28] S. Frederico, C. Hibert, R. Fritschi, Ph Fluckiger, Philippe Renaud, and A. M. Ionescu. Silicon sacrificial layer dry etching (SSLDE) for free-standing RF MEMS architectures. In *Micro Electro Mechanical Systems, 2003. MEMS-03 Kyoto. IEEE The Sixteenth Annual International Conference on*, pages 570–573. IEEE, 2003.
- [29] Yongfeng Gao, Zheng You, and Jiahao Zhao. Electrostatic comb-drive actuator for MEMS relays/switches with double-tilt comb fingers and tilted parallelogram beams. *Journal of Micromechanics and Microengineering*, 25(4):045003, 2015.
- [30] Jacek Gieras, Rong-Jie Wang, and Maarten J. Kamper. *Axial Flux Permanent Magnet Brushless Machines*. January 2008.
- [31] M. Glickman, P. Tseng, J. Harrison, T. Niblock, I. B. Goldberg, and J. W. Judy. High-Performance Lateral-Actuating Magnetic MEMS Switch. *Journal of Microelectromechanical Systems*, 20(4):842–851, August 2011.
- [32] David B. Go and Daniel A. Pohlman. A mathematical model of the modified Paschen's curve for breakdown in microscale gaps. *Journal of Applied Physics*, 107(10):103303, May 2010.
- [33] R. Goggin, P. Fitzgerald, J. e Wong, B. Hecht, and M. Schirmer. Fully integrated, high yielding, high reliability DC contact MEMS switch technology amp; control IC in standard plastic packages. In *2011 IEEE SENSORS Proceedings*, pages 958–961, October 2011.
- [34] J A Greenwood. Constriction resistance and the real area of contact. *British Journal of Applied Physics*, 17(12):1621–1632, December 1966.
- [35] Techbriefs Media Group. High-Temperature SMAs for Actuator Applications - Tech Briefs.

Bibliography

- [36] Dooyoung Hah and Songcheol Hong. A low-voltage actuated micromachined microwave switch using torsion springs and leverage. *IEEE Transactions on Microwave Theory and Techniques*, 48(12):2540–2545, December 2000.
- [37] C. Harendt, H. G. Graf, B. Hofflinger, and E. Penteker. Silicon fusion bonding and its characterization. *Journal of Micromechanics and Microengineering*, 2(3):113, 1992.
- [38] H. Hijikata and K. Akatsu. A basic study of MATRIX motor. In *2011 IEEE Energy Conversion Congress and Exposition*, pages 3285–3290, September 2011.
- [39] H. Hijikata and K. Akatsu. Design and online winding reconfigurations method of MATRIX motor. In *2012 IEEE Energy Conversion Congress and Exposition (ECCE)*, pages 1330–1337, September 2012.
- [40] H. Hijikata and K. Akatsu. Design technique and online winding reconfigurations method of MATRIX motor. In *Proceedings of The 7th International Power Electronics and Motion Control Conference*, volume 1, pages 713–718, June 2012.
- [41] Ragnar Holm. *Electric Contacts: Theory and Application*. Springer Science & Business Media, June 2013. Google-Books-ID: yfzuCAAQBAJ.
- [42] A. G. M. Jansen, A. P. van Gelder, and P. Wyder. Point-contact spectroscopy in metals. *Journal of Physics C: Solid State Physics*, 13(33):6073, 1980.
- [43] Huang Jia, Wang Xinjian, and Sun Zechang. Variable flux memory motors: A review. In *Transportation Electrification Asia-Pacific (ITEC Asia-Pacific), 2014 IEEE Conference and Expo*, pages 1–6. IEEE, 2014.
- [44] Marcel Jufer. *Electromécanique*, volume 9. PPUR presses polytechniques, 1995.
- [45] R. Kanthimathi and J. Kamala. Analysis of different flyback converter topologies. In *Industrial Instrumentation and Control (ICIC), 2015 International Conference on*, pages 1248–1252. IEEE, 2015.
- [46] T. Kato, N. Limsuwan, C. Y. Yu, K. Akatsu, and R. D. Lorenz. Rare Earth Reduction Using a Novel Variable Magnetomotive Force Flux-Intensified IPM Machine. *IEEE Transactions on Industry Applications*, 50(3):1748–1756, May 2014.
- [47] N. Klein and H. Gafni. The maximum dielectric strength of thin silicon oxide films. *IEEE Transactions on Electron Devices*, ED-13(2):281–289, February 1966.
- [48] R. Knechtel, M. Wiemer, and J. Frömel. Wafer level encapsulation of microsystems using glass frit bonding. *Microsystem Technologies*, 12(5):468–472, 2006.
- [49] Roy Knechtel. Glass frit bonding: an universal technology for wafer level encapsulation and packaging. *Microsystem technologies*, 12(1-2):63–68, 2005.

-
- [50] Y. Komura, M. Sakata, T. Seki, K. Kobayashi, K. Sano, S. Horiike, and K. Ozawa. Micro machined relay for high frequency application. In *PROCEEDINGS OF THE RELAY CONFERENCE-NATIONAL ASSOCIATION OF RELAY MANUFACTURERS*, volume 47, pages 12–12, 1999.
- [51] T. Kume, T. Iwakane, T. Sawa, T. Yoshida, and I. Nagai. A wide constant power range vector-controlled AC motor drive using winding changeover technique. *IEEE Transactions on Industry Applications*, 27(5):934–939, September 1991.
- [52] Chong-Min Kyung. *Nano Devices and Circuit Techniques for Low-Energy Applications and Energy Harvesting*. Springer, July 2015. Google-Books-ID: qUkwCgAAQBAJ.
- [53] Hee-Chul Lee, Jae-Yeong Park, and Jong-Uk Bu. Piezoelectrically actuated RF MEMS DC contact switches with low voltage operation. *IEEE Microwave and Wireless Components Letters*, 15(4):202–204, April 2005.
- [54] Hee Chul Lee, Jae Yeong Park, Kyeong Hak Lee, Hyo Jin Nam, and Jong Uk Bu. Silicon bulk micromachined RF MEMS switches with 3.5 volts operation by using piezoelectric actuator. In *2004 IEEE MTT-S International Microwave Symposium Digest (IEEE Cat. No.04CH37535)*, volume 2, pages 585–588 Vol.2, June 2004.
- [55] Thomas MH Lee, Debbie HY Lee, Connie YN Liaw, Alex IK Lao, and I.-Ming Hsing. Detailed characterization of anodic bonding process between glass and thin-film coated silicon substrates. *Sensors and Actuators A: Physical*, 86(1):103–107, 2000.
- [56] F. Li, K. T. Chau, C. Liu, and Z. Zhang. Design Principles of Permanent Magnet Dual-Memory Machines. *IEEE Transactions on Magnetics*, 48(11):3234–3237, November 2012.
- [57] M. Li, J. He, and N. A. O. Demerdash. A flux-weakening control approach for interior permanent magnet synchronous motors based on Z-source inverters. In *2014 IEEE Transportation Electrification Conference and Expo (ITEC)*, pages 1–6, June 2014.
- [58] W. Li, K. T. Chau, Y. Gong, J. Z. Jiang, and F. Li. A New Flux-Mnemonic Dual-Magnet Brushless Machine. *IEEE Transactions on Magnetics*, 47(10):4223–4226, October 2011.
- [59] N. Limsuwan, T. Kato, K. Akatsu, and R. D. Lorenz. Design and Evaluation of a Variable-Flux Flux-Intensifying Interior Permanent-Magnet Machine. *IEEE Transactions on Industry Applications*, 50(2):1015–1024, March 2014.
- [60] Hengchuan Liu, Heyun Lin, Shuhua Fang, and Xueliang Huang. Investigation of influence of permanent magnet shape on field-control parameters of variable flux memory motor with FEM. In *2008 World Automation Congress*, pages 1–4, September 2008.
- [61] Xiaogang Luo and T. A. Lipo. A synchronous/permanent magnet hybrid AC machine. *IEEE Transactions on Energy Conversion*, 15(2):203–210, June 2000.

Bibliography

- [62] Lei Ma, M. Sanada, S. Morimoto, Y. Takeda, and N. Matsui. High efficiency adjustable speed control of IPMSM with variable permanent magnet flux linkage. In *Conference Record of the 1999 IEEE Industry Applications Conference. Thirty-Forth IAS Annual Meeting (Cat. No.99CH36370)*, volume 2, pages 881–887 vol.2, 1999.
- [63] E. Maruyama, A. Nakahara, A. Takahashi, and K. Miyata. Circulating current in parallel connected stator windings due to rotor eccentricity in permanent magnet motors. In *2013 IEEE Energy Conversion Congress and Exposition*, pages 2850–2855, September 2013.
- [64] Hiroyuki Mikami, Kazumasa Ide, Yukiaki Shimizu, Masaharu Senoo, and Hideaki Seki. Historical Evolution of Motor Technology. page 8.
- [65] E. Nipp. Alternative to field-weakening of surface-mounted permanent-magnet motors for variable-speed drives. In *Conference Record of the 1995 IEEE Industry Applications Conference, 1995. Thirtieth IAS Annual Meeting, IAS '95*, volume 1, pages 191–198 vol.1, October 1995.
- [66] Eckart Nipp. *Permanent magnet motor drives with switched stator windings*. PhD thesis, Institutionen för elkraftteknik, 1999.
- [67] Eckart Nipp and Erik Norberg. On the feasibility of switched stator windings in permanent magnet motors for traction drives. In *Railroad Conference, 1998. Proceedings of the 1998 ASME/IEEE Joint*, pages 33–39. IEEE, 1998.
- [68] Vlado Ostovic. Memory motors-a new class of controllable flux PM machines for a true wide speed operation. In *Industry Applications Conference, 2001. Thirty-Sixth IAS Annual Meeting. Conference Record of the 2001 IEEE*, volume 4, pages 2577–2584. IEEE, 2001.
- [69] Vlado Ostovic. Memory motors. *IEEE Industry Applications Magazine*, 9(1):52–61, 2003.
- [70] R. Owen, Z. Q. Zhu, J. B. Wang, D. A. Stone, and I. Urquhart. Mechanically adjusted variable-flux concept for switched-flux permanent-magnet machines. In *2011 International Conference on Electrical Machines and Systems*, pages 1–6, August 2011.
- [71] Fatih M. Ozkeskin and Yogesh B. Gianchandani. Micromachined Pt–Rh and stainless steel relays for high power DC applications. *Sensors and Actuators A: Physical*, 176:130–137, April 2012.
- [72] Jamie K. Paik, Elliot Hawkes, and Robert J. Wood. A novel low-profile shape memory alloy torsional actuator. *Smart Materials and Structures*, 19(12):125014, 2010.
- [73] Jamie K. Paik and Robert J. Wood. A bidirectional shape memory alloy folding actuator. *Smart Materials and Structures*, 21(6):065013, 2012.
- [74] Fang Zheng Peng. Z-source inverter. *IEEE Transactions on industry applications*, 39(2):504–510, 2003.

- [75] R. M. Proie, T. Ivanov, J. S. Pulskamp, and R. G. Polcawich. A compact, low loss piezoelectric RF MEMS relay with sub 100-ns switching times. In *2012 IEEE/MTT-S International Microwave Symposium Digest*, pages 1–3, June 2012.
- [76] R. M. Proie, R. G. Polcawich, J. S. Pulskamp, T. Ivanov, and M. E. Zaghoul. Development of a PZT MEMS Switch Architecture for Low-Power Digital Applications. *Journal of Microelectromechanical Systems*, 20(4):1032–1042, August 2011.
- [77] Jin Qiu, J. H. Lang, A. H. Slocum, and A. C. Weber. A bulk-micromachined bistable relay with U-shaped thermal actuators. *Journal of Microelectromechanical Systems*, 14(5):1099–1109, October 2005.
- [78] J. Qui, J. H. Lang, A. H. Slocum, and R. Strumpler. A high-current electrothermal bistable MEMS relay. In *IEEE The Sixteenth Annual International Conference on Micro Electro Mechanical Systems, 2003. MEMS-03 Kyoto*, pages 64–67, January 2003.
- [79] Patrick Ragot. Modélisation analytique multiphysique pour la conception optimale de moteurs synchrones à aimants permanents. 2008.
- [80] Gabriel M. Rebeiz. *RF MEMS: Theory, Design, and Technology*. John Wiley & Sons, February 2004. Google-Books-ID: A7728XHtmzAC.
- [81] P. Rodriguez, P. Rzeszucinski, M. Sulowicz, R. Disselnkoetter, U. Ahrend, C. T. Pinto, J. R. Ottewill, and S. Wildermuth. Stator circulating currents as media of fault detection in synchronous motors. In *2013 9th IEEE International Symposium on Diagnostics for Electric Machines, Power Electronics and Drives (SDEMPED)*, pages 207–214, August 2013.
- [82] S. Sadeghi, L. Guo, H. A. Toliyat, and L. Parsa. Wide Operational Speed Range of Five-Phase Permanent Magnet Machines by Using Different Stator Winding Configurations. *IEEE Transactions on Industrial Electronics*, 59(6):2621–2631, June 2012.
- [83] S. Sadeghi, L. Parsa, and H. A. Toliyat. Extending speed range of five-phase PM machines by changing the stator windings connections. In *2011 IEEE International Electric Machines Drives Conference (IEMDC)*, pages 1540–1545, May 2011.
- [84] Koichiro Saga and Takeshi Hattori. Identification and removal of trace organic contamination on silicon wafers stored in plastic boxes. *Journal of the Electrochemical Society*, 143(10):3279–3284, 1996.
- [85] K. Sakai, K. Yuki, Y. Hashiba, N. Takahashi, and K. Yasui. Principle of the variable-magnetic-force memory motor. In *2009 International Conference on Electrical Machines and Systems*, pages 1–6, November 2009.
- [86] M. Sakata, Y. Komura, T. Seki, K. Kobayashi, K. Sano, and S. Horiike. Micromachined relay which utilizes single crystal silicon electrostatic actuator. In *Micro Electro Mechanical Systems, 1999. MEMS'99. Twelfth IEEE International Conference on*, pages 21–24. IEEE, 1999.

Bibliography

- [87] G. Schiavone, S. Smith, J. Murray, J. G. Terry, M. P. Y. Desmulliez, and A. J. Walton. Micro-mechanical test structures for the characterisation of electroplated NiFe cantilevers and their viability for use in MEMS switching devices. In *Microelectronic Test Structures (ICMTS), 2013 IEEE International Conference on*, pages 13–18. IEEE, 2013.
- [88] Giuseppe Schiavone, Andrew S. Bunting, Marc PY Desmulliez, and Anthony J. Walton. Fabrication of electrodeposited Ni–Fe cantilevers for magnetic MEMS switch applications. *Journal of Microelectromechanical Systems*, 24(4):870–879, 2015.
- [89] M. A. Schmidt. Wafer-to-wafer bonding for microstructure formation. *Proceedings of the IEEE*, 86(8):1575–1585, August 1998.
- [90] Yong Shi and Sang-Gook Kim. A lateral, self-cleaning, direct contact MEMS switch. In *18th IEEE International Conference on Micro Electro Mechanical Systems, 2005. MEMS 2005.*, pages 195–198, January 2005.
- [91] Wan Shuting and He Yuling. Analysis on stator circulating current characteristics of turbo-generator under eccentric faults. In *2009 IEEE 6th International Power Electronics and Motion Control Conference*, pages 2062–2067, May 2009.
- [92] W.R. Smythe. *Static and Dynamic Electricity*. International series in physics. London, 1939.
- [93] Peter Kelly Sokolowski. Processing and Protection of Rare Earth Permanent Magnet Particulate for Bonded Magnet Applications. Technical Report IS–T 2887, 933032, January 2007.
- [94] G. Gerald Stoney. The tension of metallic films deposited by electrolysis. *Proc. R. Soc. Lond. A*, 82(553):172–175, 1909.
- [95] Y. Tan, J. X. Shen, M. J. Jin, and H. Hao. Study of magnet fatigue in hybrid PM memory motors. In *2015 International Conference on Sustainable Mobility Applications, Renewables and Technology (SMART)*, pages 1–5, November 2015.
- [96] Min Tang, Yong Hean Lee, Rakesh Kumar, Ravi Shankar, and Olivier Le Neel. A MEMS micro-reed switch designed for portable applications. In *Solid-State Sensors, Actuators and Microsystems Conference (TRANSDUCERS), 2011 16th International*, pages 2847–2850. IEEE, 2011.
- [97] J. A. Tapia, F. Leonardi, and T. A. Lipo. Consequent pole permanent magnet machine with field weakening capability. In *IEMDC 2001. IEEE International Electric Machines and Drives Conference (Cat. No.01EX485)*, pages 126–131, 2001.
- [98] Niels Tas, Tonny Sonnenberg, Henri Jansen, Rob Legtenberg, and Miko Elwenspoek. Stiction in surface micromachining. *Journal of Micromechanics and Microengineering*, 6(4):385, 1996.

-
- [99] E. Tatar, M. M. Torunbalci, S. E. Alper, and T. Akin. A method and electrical model for the anodic bonding of SOI and glass wafers. In *Micro Electro Mechanical Systems (MEMS), 2012 IEEE 25th International Conference on*, pages 68–71. IEEE, 2012.
- [100] W. P. Taylor, O. Brand, and M. G. Allen. Fully integrated magnetically actuated micromachined relays. *Journal of Microelectromechanical Systems*, 7(2):181–191, June 1998.
- [101] Garth W. Tormoen, Jaroslaw Drelich, and Elvin R. Beach. Analysis of atomic force microscope pull-off forces for gold surfaces portraying nanoscale roughness and specific chemical functionality. *Journal of Adhesion Science and Technology*, 18(1):1–17, 2004.
- [102] Christine H. (Christine Hsin-Hwa) Tsau. *Fabrication and characterization of wafer-level gold thermocompression bonding*. Thesis, Massachusetts Institute of Technology, 2003.
- [103] G. Usai, L. Hutin, J. L. Muñoz-Gamarra, T. Ernst, M. Vinet, and P. X. L. Feng. Design considerations for optimization of pull-in stability margin in electrostatic N/MEM relays. In *2017 IEEE International Conference on IC Design and Technology (ICICDT)*, pages 1–4, May 2017.
- [104] R. Vitushinsky, S. Schmitz, and A. Ludwig. Bistable Thin-Film Shape Memory Actuators for Applications in Tactile Displays. *Journal of Microelectromechanical Systems*, 18(1):186–194, February 2009.
- [105] Albert J. Wallash and Larry Levit. Electrical breakdown and ESD phenomena for devices with nanometer-to-micron gaps. volume 4980, pages 87–97. International Society for Optics and Photonics, January 2003.
- [106] G. Wexler. The size effect and the non-local Boltzmann transport equation in orifice and disk geometry. *Proceedings of the Physical Society*, 89(4):927, 1966.
- [107] Jürgen Wibbeler, Günter Pfeifer, and Michael Hietschold. Parasitic charging of dielectric surfaces in capacitive microelectromechanical systems (MEMS). *Sensors and Actuators A: Physical*, 71(1):74–80, November 1998.
- [108] H. Woehl-Bruhn, W. R. Canders, and N. Domann. Classification of field-weakening solutions and novel PM machine with adjustable excitation. In *The XIX International Conference on Electrical Machines - ICEM 2010*, pages 1–6, September 2010.
- [109] R. F. Wolffenbuttel. Low-temperature intermediate Au-Si wafer bonding; eutectic or silicide bond. *Sensors and Actuators A: Physical*, 62(1-3):680–686, 1997.
- [110] H. Yang, H. Y. Lin, S. H. Fang, and Y. K. Huang. Novel flux-regulatable dual-magnet vernier memory motors for electric vehicle propulsion. In *2013 IEEE International Conference on Applied Superconductivity and Electromagnetic Devices*, pages 359–360, October 2013.

Bibliography

- [111] Chen Yiguang, Pan Wei, Wang Ying, Tang Renyuan, and Wang Jing. Interior composite-rotor controllable-flux PMSM - memory motor. In *2005 International Conference on Electrical Machines and Systems*, volume 1, pages 446–449 Vol. 1, September 2005.
- [112] C. Yu and K. T. Chau. Design, Analysis, and Control of DC-Excited Memory Motors. *IEEE Transactions on Energy Conversion*, 26(2):479–489, June 2011.
- [113] C. Yu and K. T. Chau. Dual-Mode Operation of DC-Excited Memory Motors Under Flux Regulation. *IEEE Transactions on Industry Applications*, 47(5):2031–2041, September 2011.
- [114] Lawrence P. Zepp and Jerry W. Medlin. Brushless permanent magnet motor with variable axial rotor/stator alignment to increase speed capability, December 2002. U.S. Classification 310/90, 310/266, 310/114, 310/209, 310/191, 310/190; International Classification H02K7/12, H02K21/00; Cooperative Classification H02K21/024; European Classification H02K21/02M2S2.
- [115] G. Zhou, T. Miyazaki, S. Kawamata, D. Kaneko, and N. Hino. Development of variable magnetic flux motor suitable for electric vehicle. In *The 2010 International Power Electronics Conference - ECCE ASIA -*, pages 2171–2174, June 2010.

Curriculum Vitae

Florian COPT

Born on August 8, 1986
florian.copt@alumni.epfl.ch

Educations

| | |
|-------------|---|
| 2014 - 2018 | Teaching student and PhD student at Integrated Actuators Laboratory (LAI) École Polytechnique Fédérale de Lausanne, Switzerland |
| 2011 - 2013 | Master of Science in Microengineering, Robotics and autonomous systems specialization École Polytechnique Fédérale de Lausanne, Switzerland |
| 2007 - 2011 | Bachelor in Microengineering, École Polytechnique Fédérale de Lausanne, Switzerland |

Publications

- F. Copt, D. Martins Araujo, C. Koechli and Y. Perriard, Current control strategy for dynamic winding reconfiguration of slotless brushless DC motors, IEEE Transaction on Industrial Applications, IAS, Accepted for publication, 2018
- F. Copt, D. Martins Araujo, C. Koechli and Y. Perriard, Dynamic Winding Reconfiguration of a Brushless DC Motor, 2017 IEEE International Electric Machines and Drives Conference (IEMDC), Miami, FL, USA, May 21-24, 2017
- J. Poliakine, F. Copt, D. Martins Araujo, Y. Civet, Y. Perriard : Modeling, Design, and Manufacturing of Microfabricated Coils With High Inductance Density; Journal of Microelectromechanical Systems. 2017. DOI : 10.1109/JMEMS.2017.2727544.

Appendix D. Curriculum Vitae

- F. Copt, D. Martins Araujo, C. Koechli and Y. Perriard, Current control strategy for dynamic winding reconfiguration of a brushless DC motor, 2017 IEEE Energy Conversion Congress and Exposition (ECCE), Cincinnati, OH, USA, 1-5 Oct. 2017
- F. Copt, C. Koechli, Y. Perriard : Electrostatically actuated MEMs relay for high power applications. 2016. The 19th International Conference on Electrical Machines and Systems (ICEMS2016), Chiba, Japan, November 13-16, 2016.
- F. Copt, C. Koechli and Y. Perriard, Study on the Layout of the BLDC Motor's Winding in Order to Minimize the Circulating Current, The Seventh Annual IEEE Energy Conversion Congress & Exposition (ECCE 2015), Montreal, Canada, September 20 - 24, 2015.
- C. Auvigne, F. Copt, C. Winter, Y. Perriard : Study of Various Winding Topologies for Self-Shielding Induction Cookers; Journal of International Conference on Electrical Machines and Systems (JICEMS). 2013.
- F. Copt, C. Auvigne, C. Winter, Y. Perriard : A Novel winding topology applied for a self-shielding induction cooker. 2013. The International Conference on Electrical Machines and Systems 2013 (ICEMS 2013), Busan, Korea, October 26 - 29, 2013.

